Title
Micro-scale piezoelectric vibration energy harvesting: from fixed-frequency to adaptable-frequency devices

Author
Miller, Lindsay Margaret

Publication Date
2012

Peer reviewed|Thesis/dissertation

Micro-scale piezoelectric vibration energy harvesting: from fixed-frequency to adaptable-frequency devices

by

Lindsay Margaret Miller

A dissertation submitted in partial satisfaction of the
requirements for the degree of
Doctor of Philosophy

in

Engineering - Mechanical Engineering

and the Designated Emphasis

in

Energy Science and Technology

in the

Graduate Division

of the

University of California, Berkeley

Committee in charge:

Professor Paul K. Wright, Chair
Professor Einar Halvorsen
Professor David Dornfeld
Professor Jan Rabaey

Spring 2012

Micro-scale piezoelectric vibration energy harvesting: from fixed-frequency to adaptable-frequency devices

Abstract

Micro-scale piezoelectric vibration energy harvesting:
from fixed-frequency to adaptable-frequency devices

by

Lindsay Margaret Miller

Doctor of Philosophy in Engineering - Mechanical Engineering

Designated Emphasis in Energy Science and Technology

University of California, Berkeley

Professor Paul K. Wright, Chair

Wireless sensor networks (WSNs) have the potential to transform engineering infrastructure, manufacturing, and building controls by allowing condition monitoring, asset tracking, demand response, and other intelligent feedback systems. A wireless sensor node consists of a power supply, sensor(s), power conditioning circuitry, radio transmitter and/or receiver, and a micro controller. Such sensor nodes are used for collecting and communicating data regarding the state of a machine, system, or process. The increasing demand for better ways to power wireless devices and increase operation time on a single battery charge drives an interest in energy harvesting research.

Today, wireless sensor nodes are typically powered by a standard single-charge battery, which becomes depleted within a relatively short timeframe depending on the application. This introduces tremendous labor costs associated with battery replacement, especially when there are thousands of nodes in a network, the nodes are remotely located, or widely-distributed. Piezoelectric vibration energy harvesting presents a potential solution to the problems associated with too-short battery life and high maintenance requirements, especially in industrial environments where vibrations are ubiquitous.

Energy harvester designs typically use the harvester to trickle charge a rechargeable energy storage device rather than directly powering the electronics with the harvested energy. This allows a buffer between the energy harvester supply and the load where energy can be stored in a "tank". Therefore, the harvester does not need to produce the full required power at every instant to successfully power the node. In general, there are tens of microwatts of power available to be harvested from ambient vibrations using micro scale devices and tens of milliwatts available from ambient vibrations using meso scale devices. Given that the power requirements of wireless sensor nodes range from several microwatts to about one hundred milliwatts and are falling steadily as improvements are made, it is feasible to use energy harvesting to power WSNs.

This research begins by presenting the results of a thorough survey of ambient vibrations in the machine room of a large campus building, which found that ambient vibrations are low frequency, low amplitude, time varying, and multi-frequency. The modeling and design of fixed-frequency micro scale energy harvesters are then presented. The model is able to take into account rotational inertia of the harvester's proof mass and it accepts arbitrary measured acceleration input, calculating the energy harvester's voltage as an output.

The fabrication of the micro electromechanical system (MEMS) energy harvesters is discussed and results of the devices harvesting energy from ambient vibrations are presented. The harvesters had resonance frequencies ranging from 31 – 232 Hz, which was the lowest reported in literature for a MEMS device, and produced 24 pW/g^2 – 10 nW/g^2 of harvested power from ambient vibrations. A novel method for frequency modification of the released harvester devices using a dispenser printed mass is then presented, demonstrating a frequency shift of 20 Hz.

Optimization of the MEMS energy harvester connected to a resistive load is then presented, finding that the harvested power output can be increased to several microwatts with the optimized design as long as the driving frequency matches the harvester's resonance frequency. A framework is then presented to allow a similar optimization to be conducted with the harvester connected to a synchronously switched pre-bias circuit.

With the realization that the optimized energy harvester only produces usable amounts of power if the resonance frequency and driving frequency match, which is an unrealistic situation in the case of ambient vibrations which change over time and are not always known *a priori*, an adaptable-frequency energy harvester was designed. The adaptable-frequency harvester works by taking advantage of the coupling between a sliding mass and a beam. The derivation of the nonlinear coupled dynamic mathematical model representing the physical system is presented, as are the numerical and experimental results of the prototype device. Passive self-tuning was observed in this system and the mathematical model was found to successfully portray the physical behavior.

To my family.

Contents

List of Figures

List of Tables

Acknowledgments

This work was funded by the California Energy Commission Contract 500-01-43, and the Demand Response project DR-03-01. Additionally, the Research Council of Norway Grant 191282 and SIU Contract No. NNA-2008/10004 supported the collaboration with Professor Halvorsen. The MEMS devices presented here were fabricated in the UC Berkeley microfabrication laboratory.

On a personal note, I have been incredibly fortunate through the course of my graduate study to work with and be supported by many wonderful people. I feel compelled to thank those who have played a significant role in my research and life while I worked on this dissertation.

My research advisor, Professor Paul Wright, had an unwavering belief in my ability to figure things out, allowing me the independence to approach our research goals from the direction I thought was best. His encouragement and support were greatly appreciated. I am also grateful to Professor Einar Halvorsen, who is a fantastic teacher and an insightful researcher. Our fruitful collaboration enriched my graduate research experience tremendously. I also owe thanks to Professor Paul Mitcheson for a valuable research collaboration, to Professors Jan Rabaey and David Dornfeld for serving on my dissertation committee, and to Professor Jim Evans for his input over the years.

I am thankful to have had a great group of fellow lab members over the years who could be counted on for stimulating research conversations and collaborations, coffee breaks, and friendship. I want to thank Beth for giving me a running start by putting me in a bunny suit to clean wafers on my first day of work and teaching me everything she knew about microfabrication. I owe thanks to Nate for teaching me all about the sol-gel process and bestowing grad school wisdom upon me. I'm grateful for the camaraderie of Christine, Eli, Alic, and Andrew. Dan Chapman deserves huge thanks for keeping the lab running smoothly, and for leaving cookies on my desk on the afternoons I needed them most.

Thank you to the amazing women of the Friday ladies' breakfast tradition, whose friendship is invaluable to me. Thank you to Tadas, Ioan, and Josee for inspiring me to pursue grad school. I am deeply grateful to and thankful for my sisters, Karly and Ariel, who are my best friends in the world and are always there for me. I want to thank Grandpa Karl for his scientific influence, Grandma Peggy for being a role model of strength and fiery independence, Grandpa Doyle for teaching me a love of building things, and my parents for giving me all the tools I needed to pursue my goals. To my fiance, John, thank you for filling the journey through grad school with laughing fits and bright spots - shekh ma shieraki anni.

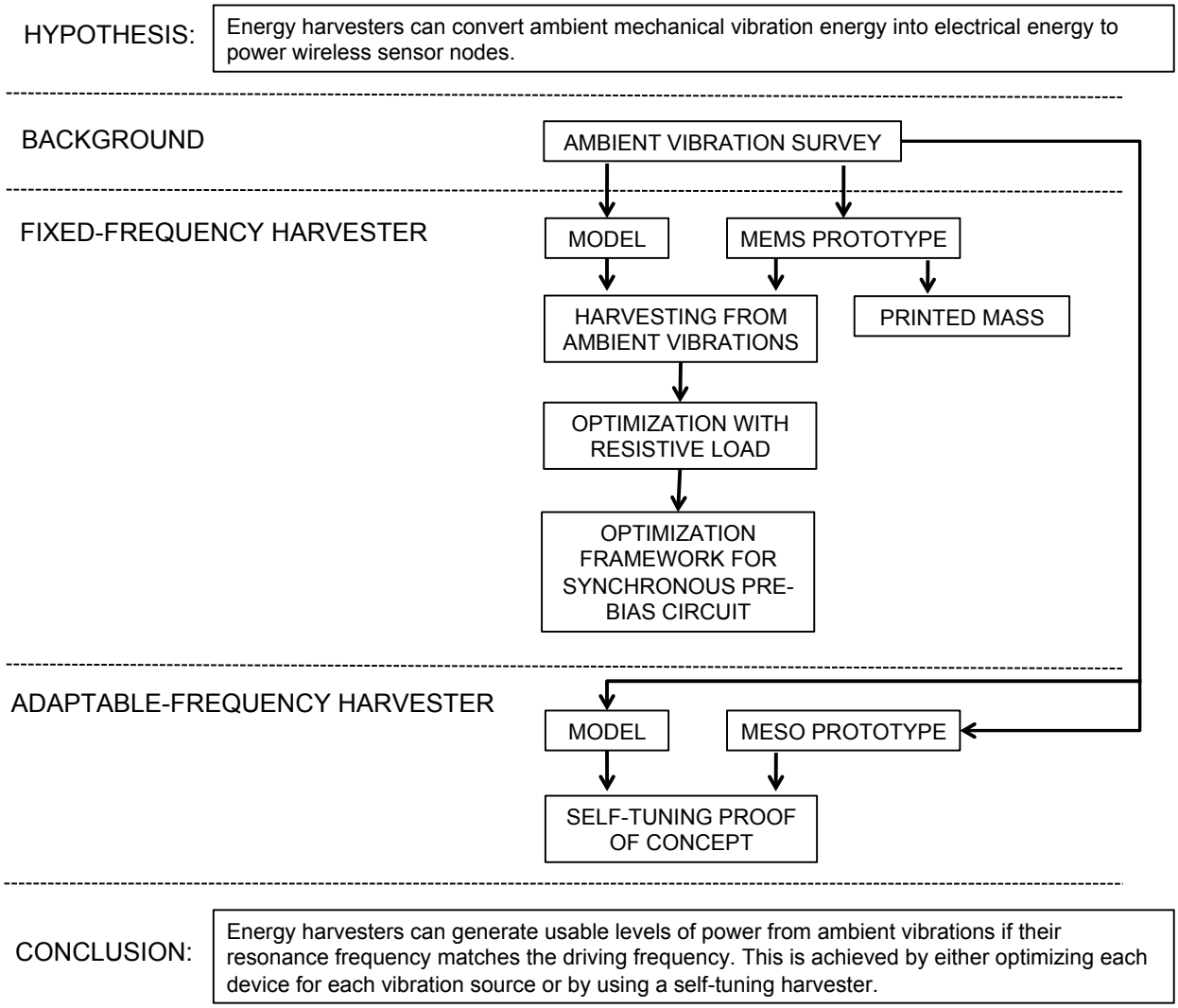
HYPOTHESIS:
Energy harvesters can convert ambient mechanical vibration energy into electrical energy to power wireless sensor nodes.
BACKGROUND
AMBIENT VIBRATION SURVEY
FIXED-FREQUENCY HARVESTER
MODEL
MEMS PROTOTYPE
HARVESTING FROM AMBIENT VIBRATIONS
PRINTED MASS
OPTIMIZATION WITH RESISTIVE LOAD
OPTIMIZATION FRAMEWORK FOR SYNCHRONOUS PRE-BIAS CIRCUIT
ADAPTABLE-FREQUENCY HARVESTER
MODEL
MESO PROTOTYPE
SELF-TUNING PROOF OF CONCEPT
CONCLUSION:
Energy harvesters can generate usable levels of power from ambient vibrations if their resonance frequency matches the driving frequency. This is achieved by either optimizing each device for each vibration source or by using a self-tuning harvester.

Chapter 1

Introduction

1.1 Motivation for energy harvesting research

Energy harvesting began centuries ago with waterwheels and windmills and continues to this day to inspire engineering creativity because the concept of "free energy" is so appealing. Energy harvesting technology has made incredible advances in the past few decades as new sources of harvestable energy were identified, novel materials for energy conversion were developed, and the advent of low-power computing opened up a whole new realm of applications for using harvested energy. The increasing demand for better ways to power wireless devices and increase operation time on a single battery charge continues to drive research in energy harvesting today.

1.1.1 Wireless sensing enabled by energy harvesting technology

Electronic devices that are well-suited to utilize energy harvesting technology include sensor nodes in wireless sensor networks (WSNs) [54]. A wireless sensor node consists of a power supply, sensor(s), power conditioning circuitry, radio transmitter and/or receiver, and a micro controller. Such sensor nodes are used for collecting and communicating data regarding the state of a machine, system, or process. Variables that may be sensed include, but are not limited to, temperature, occupancy, vibrations, air quality, humidity, sound, and pressure.

Wireless, rather than hard-wired, sensing systems are appealing because they avoid the highly labor intensive and material intensive expenses associated with installing a hard-wired system. The exception may be with sensor networks that are incorporated into a building as it is constructed rather than added as a retrofit later on. Another advantage of wireless networks is that they are much quicker and easier to install and there are fewer limitations on where the sensing nodes must be located if they do not need to be hard-wired. In the ideal case, WSN nodes can be installed in seconds anywhere the user desires using magnets or velcro, and easily readjusted later if a different sensing point is needed.

The application areas of WSNs to engineering infrastructure, manufacturing processes, and building control are extensive. Condition monitoring of equipment and machinery can allow engineers to perform maintenance only as needed, eliminate unscheduled downtime, improve productivity and process efficiency, increase available information about a process for quality control, and improve energy efficiency. WSNs also have the potential to open up many applications in asset tracking. From an infrastructure perspective, demand response, energy efficiency, and smart or automated control can be enabled by providing data about state variables of the HVAC systems or electricity grid, for example.

Today's WSNs are typically powered by standard batteries, with a small fraction powered by some form of energy harvesting [25]. The problem with the battery powered sensor nodes is that the batteries become depleted within a relatively short timeframe, depending on the application. This is a problem because the labor costs associated with battery replacement quickly become prohibitive, especially when there are thousands of nodes in a network or the nodes are widely-distributed. Additionally, nodes may be located in remote places that are hard to reach or even inaccessible, making battery replacement even more cumbersome. Finally, when long sensor node lifetimes are required, batteries may not have the necessary shelf life without becoming very large or expensive.

Energy harvesting presents a potential solution to the problems associated with too-short battery life and high maintenance requirements by providing an autonomous, replenishable power supply. Energy harvester designs typically operate by using the harvester device to trickle charge a rechargeable battery and/or capacitor rather than directly powering the electronics with the harvested energy. This allows a buffer between the energy harvester supply and the load where energy can be stored in a "tank". Therefore, the harvester does not need to produce the full required power at every instant to successfully power the node. The reason that both a battery and capacitor may be used is that the battery provides a longer, slower supply of energy, while the capacitor can provide quick bursts of power as may be needed to transmit a signal [22, 23].

1.1.2 Power demands of wireless sensor nodes

Part of what has supported the demand of autonomous WSNs is the reduction in power requirements for radio transmitters and microprocessors. Power demand numbers for a commercial and research phase wireless sensor node are given in table 1.1. The commercial node is the Dust Networks SmartMesh IP DN6000/M600x [25] and is taken to be representative of commercially available WSN nodes. The research level node is the PicoCube [55], which contains less functionality than the Dust node but illustrates the trends of low power limits.

Table 1.1 points out that wireless sensor nodes require different amounts of power depending on whether they are in a sleep state, transmitting or receiving data, writing to memory, or performing other functions. An energy harvester supplying power to such a node does not need to constantly provide the instantaneous amount of power the node is using since the harvester will charge a battery and capacitor, which serve as a storage tank. In this way,

Table 1.1: Wireless sensor node power requirements [25, 55]

	Node state	Power required (mW)
Dust Networks commercial node	Peak operation*	108
	Radio transmit	34.9
	Radio receive	16.2
	Flash write	10.8
	Flash erase	9.0
	Active**	8.6
	Doze***	0.0043
Pico Cube research platform node	Radio transmit	6
	Standby	< 0.001
	Average****	0.006

* 14.7 MHz. Flash write, radio transmitter on.

** 7.37 MHz. Flash, ARM Cortex-M3, RAM on. Radio, peripherals off.

*** 32.768 kHz. RAM on, data and state retained. All else off.

**** For transmitting once every 6 seconds

the harvester may produce more energy than the node requires during sleep state and this energy can be stored to use when the node is in a high power state.

Because of the inconsistent power demands of the node, the average power required depends on the duty cycle. Duty cycle refers to how frequently the node turns on its high power active states to send or receive a signal or write data to memory, and is determined both by needs of the application and by how much energy the harvester can supply. Low duty cycle values mean that a much lower average power than peak power is required to operate the node. The harvester must be able to provide enough energy to meet the average power demands of the node in order to be a feasible power source.

The power requirements of any sensors used in the node must be taken into account, as well, and are typically on the order of several mW for standard sensors. However, in the past few years a number of sensors with power requirements in the μW range have appeared on the market, for example, Analog Devices ADXL345 [24] and STMicroelectronics LIS3DH [27] accelerometers. At the research level there are also a number of passive or self-powered sensors under development, for example, a passive AC current sensor [36].

1.1.3 Sources of harvestable energy

There are many possible sources of harvestable energy and the best source depends highly on the requirements and environment of the application. In some cases it is possible to harvest from more than one energy source to power a single node. This section does not, therefore, attempt to name one energy harvesting source as better than the others, but simply outlines

the options available. For a more detailed overview of the different energy harvesting sources, see [66] and [53].

Sunlight may be one of the most widely recognized harvestable sources of energy. Solar photovoltaic devices harvest the light energy while solar thermal devices utilize the Sun's heat. Fluid motion, in the form of wind or water movement, is another common source of energy. Wind energy harvesting can be utility scale using turbines or small scale, such as from HVAC ducts, using von Karman vortex shedding [67]. Ocean harvesting technologies can be designed to take advantage of tidal changes, flowing currents, or the motion of waves [6]. Thermal and pressure gradients are less commonly considered sources of harvestable energy, as are radio frequencies [28]. Ambient mechanical vibrations from machinery can also be harnessed and are the focus of this thesis.

This research is motivated by the need to power wireless sensor networks. For applications of wireless sensor networks in buildings, including manufacturing or industrial process monitoring, machine condition assessment, smart grid, smart buildings, demand response and energy efficiency, vibrations are a ubiquitous source of energy, especially where solar or thermal energy may not be consistently available. Therefore, the focus of this work is on harvesting energy from ambient vibrations. Throughout this work, the term "ambient vibrations" is taken to mean any vibrations existing in the environment from machinery, appliances, or movement of building occupants. Examples include pumps, motors, fans, ducts, industrial equipment, transformers, and even doors slamming.

1.2 Vibration energy harvesting

1.2.1 Theoretically available power from ambient vibrations

The maximum power theoretically available from ambient vibrations can be expressed as [46]

$$P_{\max} = \frac{1}{4}\frac{mA_{\text{in}}^2 Q}{\omega_{\text{in}}} \tag{1.1}$$

where m is the mass, A_{in} is the magnitude of input acceleration, ω_{in} is the input vibration frequency, and Q is the quality factor, which is a nondimensional parameter that characterized the amount of damping in the system. This equation assumes sinusoidal vibration input, operation at resonance, unconstrained displacement, and optimal electrical damping. In the case of unconstrained displacement, optimal electrical damping occurs when mechanical and electrical damping are equal.

In the case of a displacement-constrained vibration, optimal electrical damping occurs when the electrical damping just barely constrains beam motion within the package, so equation (1.1) becomes

$$P_{\max} = \frac{1}{2}mA_{\text{in}}\omega_{\text{in}}Z_{\text{limit}} \tag{1.2}$$

Table 1.2: Example calculations for maximum theoretically available power from ambient vibrations using typical values for micro and meso scale devices

		Variable	Value	
Micro scale device	A_{in}	Input acceleration	0.203 g	m/s^2
	ω_{in}	Input frequency	22.5	Hz
	m	Mass	118e-6	kg
	Z_{limit}	Displacement limit	4e-3	m
	Q	Quality factor	100	
	P_{max}	**Maximum power**	**66***	μW
Meso scale device	A_{in}	Input acceleration	0.203 g	m/s^2
	ω_{in}	Input frequency	22.5	Hz
	m	Mass	12e-3	kg
	Z_{limit}	Displacement limit	1e-2	m
	Q	Quality factor	100	
	P_{max}	**Maximum power**	**16.9***	mW

* displacement constrained case

where Z_{limit} is the maximum displacement allowed by the constraint. Equation (1.2) is the more realistic expression since in most cases the energy harvester will be packaged to protect it from the environment and also may include end stops to protect it from mechanical failure.

These expressions highlight the factors that determine the power available to harvest from ambient vibrations. The power scales directly with mass, input acceleration and frequency, and displacement limit. Table 1.2 shows example calculations for maximum theoretically available power using typical values for micro and meso (several centimeter) scale devices. For micro devices, tens of μW are typically available, while tens of mW are available for meso scale devices. It is important to note that these equations for maximum power available do not take into account any details about efficiency of the energy conversion mechanism. Rather, given information about the vibrations, the mass of the device, and the package size, these equations give the amount of power that could be harvested if the energy conversion mechanism could convert all of the mechanical energy to electrical energy. Based on the power requirements of sensor nodes listed in table 1.1, it is evident that there is enough energy available in ambient vibrations to power a wireless sensor node assuming that the node is operated efficiently and that the energy harvester efficiently converts mechanical to electrical energy.

1.2.2 Vibration-to-electrical energy conversion mechanisms

There are three commonly used methods for converting mechanical energy into electrical energy: electrostatic, electromagnetic, and piezoelectric. Electrostatic harvesting works by

using vibration-induced motion of the inertial proof mass to change the capacitance of the device while holding voltage or charge constant. Electromagnetic harvesting uses vibration-induced motion of the inertial proof mass to move a magnet relative to a conductive coil, thereby generating a current in the coil. Piezoelectric harvesters use vibrations to induce deflection of a spring structure connected to an inertial proof mass, where the spring structure is made of a piezoelectric material. All three of these conversion techniques can be modeled as spring-mass-damper systems.

In general, electrostatic devices are well-suited to micro electromechanical systems (MEMS) because small capacitor gap sizes are desirable, while electromagnetic devices are better suited for meso scale systems because it is difficult to achieve a large number of coils or long translation distances through the coils in a MEMS fabricated device. Piezoelectric devices can work at either the MEMS or meso scale, but the energy conversion capability of the piezoelectric thin films used at the MEMS scale tend to be inferior by approximately an order of magnitude to that of bulk ceramic piezoelectric materials that are used at the meso scale.

There is not, in general, a consensus in the literature about which technique is superior, as the ideal harvesting technique tends to be application-specific. A more detailed comparison of the three conversion techniques is outside the scope of this work but can be found in literature [28, 54, 66]. Piezoelectric harvesting is attractive, for both micro and meso scale devices, because of its simple configuration and its high energy conversion potential [54], and is thus the focus of this research.

1.2.3 MEMS versus macro scale devices

There is growing interest in miniaturization and integration of electronics, radios, sensors, and power sources for sensor networks and personal electronics. Because of this, MEMS scale energy harvesting has received attention over the past decade, yet MEMS harvesters still struggle to produce enough power to be usable. This raises the question of whether MEMS scale energy harvesting technologies are viable or if efforts should be focused on meso scale devices.

The main disadvantage of MEMS devices is that they are mass-limited, limiting the maximum theoretical power available to harvest according to equation (1.2). Another disadvantage of MEMS harvesters is that in some cases the piezoelectric material properties are inferior to those available with a bulk device, as described in section 1.2.2. Additionally, it can be difficult to achieve high coupling with MEMS electromagnetic devices because of fabrication constraints limiting the number of magnetic coils that can be achieved. However, it is feasible that in the near future the MEMS scale energy conversion materials will improve to the point where they are an advantage over bulk materials, rather than a disadvantage [48].

Despite these challenges, MEMS devices are very appealing due to their compact size, their potential for integration with electronic components, and their potential for cost reductions using standard semiconductor fabrication processes. The bottom line at this point

in time is that MEMS energy harvesting devices have incredible potential. There are some applications which can use meso scale harvesting devices with no drawbacks because there is not a spacial constraint, yet other applications are dependent on achieving small form factors and integrated components. Given that the power requirements of electronics are continuously decreasing and MEMS energy harvesters are improving in higher power output and lower cost, it is justifiable to continue research towards the goal of a well-integrated MEMS scale energy harvester while, at the same time, recognizing that not every application requires a MEMS solution. This research focuses mostly on MEMS piezoelectric energy harvesting devices.

1.2.4 Piezoelectric manufacturing considerations

There are several standard ways to fabricate MEMS piezoelectric thin films for use in energy harvesters: pulsed laser deposition (PLD), sputtering, and sol-gel deposition. Other more upstream materials science focused deposition methods exist but were not considered for this research. Sol-gel deposition was chosen for this research because it is the most scalable of the thin film deposition processes, does not require tremendous up-front equipment costs to carry out, and is relatively quick. It requires only access to a spin-coater, hotplates, and a rapid thermal annealer, as well as sol-gel piezoelectric chemicals, and can achieve film deposition on silicon wafers of arbitrary size. The disadvantage of sol-gel deposition is that it is difficult to achieve the high piezoelectric conversion coefficients that are desired. PLD, in contrast, requires a sophisticated laser setup, can only be conducted using 1 cm^2 sample sizes, and takes a very long time to complete each sample, but results in incredibly high quality piezoelectric films. Sputtering falls somewhere in between, having potential to work with wafer-scale deposition and producing good piezoelectric films, yet requiring access to expensive and specialized equipment and piezoelectric sputtering targets.

The piezoelectric material chosen for this research was lead zirconate titanate, or PZT, because it is a well known and well-characterized material with a high piezoelectric coefficient. However, because of the lead content, it has the potential to pose an environmental hazard and it is not compatible with complimentary metal oxide semiconductor (CMOS) processing, undermining the goal to eventually integrate the MEMS energy harvester with electronic components. Aluminum Nitride (AlN) is a potentially better alternative piezoelectric material because it does not contain toxic materials, is CMOS compatible, and has a piezoelectric coupling coefficient comparable to PZT. Its piezoelectric coefficient is lower, but so is its dielectric constant, resulting in an overall coupling coefficient of similar value. Additionally, AlN can be easily deposited using sputtering, so it upholds the goal of achieving a scalable manufacturing process.

1.2.5 Commercially available vibration energy harvesters

Several companies have developed macro-scale vibration energy harvesting technologies that are available commercially, including Perpetuum, Enocean, KCF Technologies, Microstrain, and Mide Volture. National Instruments has recently partnered with Perpetuum to sell an energy harvester-powered sensor node. These devices generate power output on the order of several hundred μW to mW from vibration amplitudes as low as 0.25 g. These macro-scale harvesters are well-suited for some applications, but their large size and weight (more than 1 kg for one Perpetuum harvester) is a disadvantage and severely limits the possible applications. To this author's knowledge, there are no MEMS vibration energy harvesters on the market.

1.3 Importance of ambient vibration focus

Energy harvesting is only truly "harvesting" if it converts ambient vibrations, not laboratory supplied vibrations, into electrical energy. For vibration energy harvesters to utilize ambient vibrations, they must be able to respond to the low frequency, low acceleration, time-varying, often broadband vibrations that exist in the environment [11, 54]. In contrast to those requirements, most researchers report MEMS energy harvesters with high resonance frequencies tested at resonance on a vibrometer with a single sinusoidal frequency at high acceleration [14, 16, 30, 39, 52, 57]. While such studies are very important for energy harvester characterization and modeling insight, they do not accurately represent ambient vibration conditions or prove that the device can actually harvest energy in realistic conditions. Only two studies have used realistically low magnitude acceleration in vibrometer tests of MEMS energy harvesters at relatively low frequency of 204 Hz and 0.5 g [38] and 528 Hz and 0.39 g [47].

A number of authors have tested or modeled energy harvester response to random acceleration input, as opposed to sinusoidal input, in order to mimic ambient vibration sources. Two studies tested MEMS harvesters with sinusoidal as well as random vibration input on a vibrometer. They explored nonlinear behavior of the devices due to nonlinear spring stiffness [65] and a mechanical stopper [4] in order improve the harvester effectiveness subjected to random input vibration. One author presented a model for random vibrations, deriving closed-form expressions for power output, displacement, and optimal load [19]. Two research groups have presented meso scale harvesters tested with random vibration input on a vibrometer in order to explore which power conditioning schemes [35] and energy storage configurations [58] work well with random vibrations. To the author's knowledge, our study of MEMS energy harvesters tested with ambient vibration acceleration input is the first of its kind in the literature [43].

This dissertation is organized as follows. Chapter 2 presents a survey of ambient vibration sources in a large campus building. The characteristics of these ambient vibration sources

are what motivate the approach taken in this research. Chapters 3 through 7 pertain to a fixed-frequency energy harvester, while chapters 8 and 9 present a new model and design which leads to an adaptable-frequency harvester. Specifically, Chapter 3 lays out the mathematical model for the fixed-frequency energy harvester, and chapter 4 presents the design, fabrication, and testing of the fixed-frequency energy harvester. Next, chapter 5 describes a technique to customize the resonance frequency of a fixed-frequency harvester. In chapter 6, an optimization is conducted on the energy harvester with a resistive load. Chapter 7 lays out a framework in which an optimization could be performed with the harvester connected to a synchronous switched circuit to boost output and condition the power. Chapter 8 presents the model for an adaptable-frequency harvester, and chapter 9 reports the simulation results and experimental results from the meso scale adaptable-frequency prototype device. Finally, concluding remarks are given in chapter 10.

The contributions of this work to the field of energy harvesting can be summarized as:

1. Survey of ambient vibrations in a machine room setting (Chapter 2)
2. Development of a model for a fixed-frequency harvester that accounts for rotational inertia of the proof mass and accepts arbitrary measured acceleration input (Chapter 3)
3. Fabrication of MEMS energy harvesters with frequencies of 31–232 Hz (Chapter 4)
4. Harvesting energy from ambient vibration sources (Chapter 4)
5. Demonstration of pneumatically printed proof mass post-microfabrication (Chapter 5)
6. Optimization of harvester with a resistive load and ambient vibration input compared to sinusoidal vibration input (Chapter 6)
7. Development of a framework to allow harvester optimization when connected to a synchronously switched pre-biasing circuit (Chapter 7)
8. Development of a model for an adaptable-frequency, or "self-tuning", harvester consisting of a fixed-fixed beam with sliding mass (Chapter 8)
9. Demonstration of self-tuning resonator proof of concept (Chapter 9)

Chapter 2

Survey of Ambient Vibrations in Buildings

In order to understand how to appropriately design an energy harvester, it is critical to understand the energy source to be harvested. To this end, an extensive survey of ambient vibration sources was conducted in the machine room of a large building, Etcheverry Hall, on the UC Berkeley campus. The vibration data presented in this chapter inform and motivate the approach taken in the rest of this dissertation. This chapter is adapted from [43].

Data were collected at a sampling rate of 2048 Hz using a Microstrain G-link wireless 3-axis accelerometer magnetically mounted on the vibration source. All three axes were surveyed, but in most cases the z-axis (orthogonal to the vibrating surface) acceleration was an order of magnitude higher than x- and y-axes, so only the z acceleration is reported and used in this study.

Table 2.1 reports the three frequency peaks with the highest acceleration for each vibration source. The results in this table indicate that the dominant frequency peaks from the majority of the sources surveyed lie between 20-60 Hz, with another set of frequencies lying between 120-140 Hz. Three sources also contain peaks around 350 Hz. The accelerations of the ambient vibrations were all below 0.7 $g/\sqrt{Hz}$, with most accelerations on the order of 10^{-2} to 10^{-1} $g/\sqrt{Hz}$. These findings are consistent with previous vibration surveys [11, 54].

Figure 2.1 shows the general configuration of the energy harvester and accelerometer during data collection. The compressor base vibration source is shown in 2.1a and the fan belt cage vibration source is shown in Figure 2.1b to show both horizontal and vertical mounting. The fan and drive belt are part of an HVAC system and the cage encloses the belt.

The full frequency spectrum for "fan belt cage 1" and "compressor base" from Table 2.1 are shown in Figure 2.2. The graphs show the power spectral density (PSD) on a semi log scale versus frequency, where plots 2.2a and 2.2c show the full spectrum and 2.2b and 2.2d show close up on area of interest from zero to 250 Hz. These two examples illustrate the extremes of the vibration sources measured, ranging from smooth spectra with a few

Table 2.1: Acceleration & frequency of the dominant peaks in the vibration spectra of equipment in a campus building machine room. Note that the peaks, f_1, f_2, and f_3, are not harmonics but rather are the first, second, and third highest vibration frequencies.

	Units of a: $g/\sqrt{Hz}$, Units of f: Hz					
	Highest peak		2^{nd} highest		3^{rd} highest	
Source	a_1	f_1	a_2	f_2	a_3	f_3
^{V} Fan belt cage 1 •	0.332	22.5	0.241	45.0	0.118	20.5
^{V} Fan belt cage 2	0.120	37.5	0.096	27.5	0.094	23.0
^{V} Fan belt cage 3 •	0.236	40.5	0.216	40.6	0.163	40.4
^{V} Fan belt cage 4 •	0.376	30.0	0.070	25.5	0.210	38.5
^{S} Fan belt cage 1	0.159	27.6	0.150	25.9	0.144	26.0
^{S} Fan belt cage 2	0.178	36.4	0.173	34.2	0.164	36.3
^{S} Fan belt cage 3	0.223	26.0	0.206	25.9	0.199	20.4
^{H} HVAC duct 1 •	0.020	15.5	0.020	29.5	0.014	79.0
^{H} HVAC duct 2 •	0.174	28.7	0.157	29.2	0.156	28.6
^{H} HVAC duct 3	0.042	30.1	0.042	30.2	0.037	30.4
^{V} HVAC duct 4	0.055	20.4	0.054	19.5	0.050	19.4
^{V} HVAC duct 5	0.042	40.0	0.041	31.0	0.037	39.9
^{V} HVAC duct 6	0.054	60.6	0.050	60.7	0.047	60.5
^{S} HVAC duct 7	0.058	21.7	0.057	21.6	0.056	21.5
^{S} Compressor	0.113	29.4	0.110	29.4	0.099	29.3
^{H} Compressor base •	0.074	29.5	0.064	59.0	0.035	354.0
^{V} Controller	0.408	29.4	0.384	29.4	0.311	29.2
^{H} Pipe •	0.064	354.0	0.041	29.5	0.037	324.5
^{S} Water pump	0.669	135.6	0.669	135.7	0.539	135.4
^{H} Belt drive motor •	0.090	22.5	0.056	136.5	0.055	138.0
^{H} Floor by fan	0.020	19.1	0.017	20.0	0.017	19.0
^{V} Fan housing	0.049	121.4	0.048	121.5	0.044	122.0
^{H} Transformer	0.035	120.5	0.025	29.5	0.010	361.0

^{V} vertical, ^{H} horizontal, or ^{S} slanted surface
• Source upon which harvesters were tested

distinct peaks to rugged-looking spectra with both broad bumps and sharp peaks. Please see appendix A for more plots of vibration spectra.

In contrast to markedly different vibration spectrum, several groups of vibration sources demonstrated similarities. The spectra for the four vertical fan belt cage surfaces surveyed were almost identical. The spectra for the three slanted fan belt cage surfaces showed similarities in the general shape but the specific peaks were not the same. The three vertical ducts had similarities and the three horizontal ducts had similarities in general shape as well,

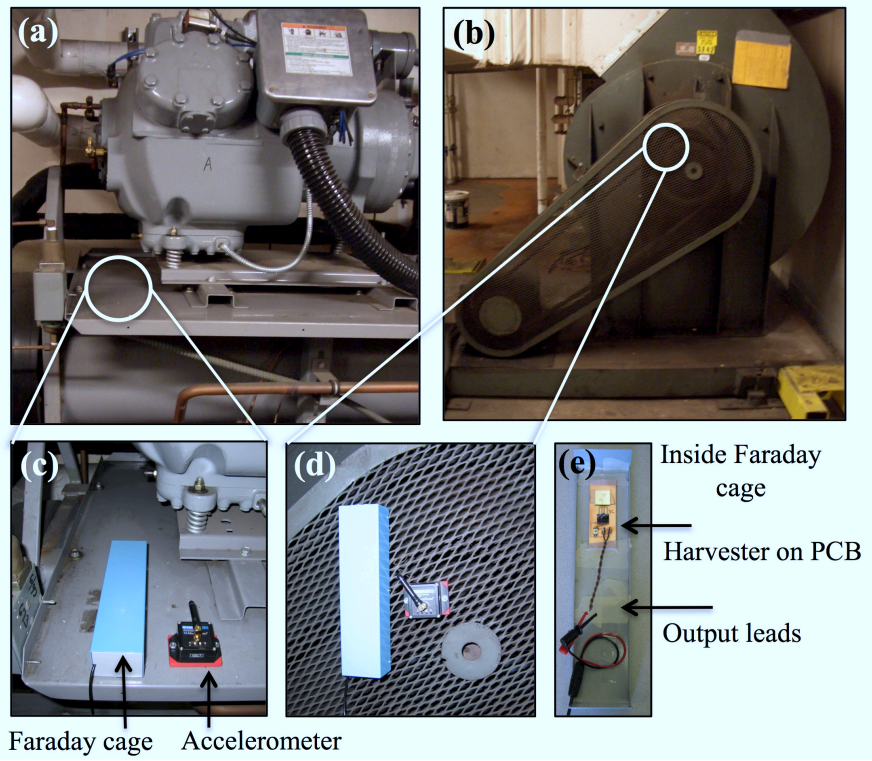

Figure 2.1: Photographs showing the testing configuration: a) compressor base. b) fan belt cage. c) and d) accelerometer (small black square) and Faraday cage containing energy harvester (rectangular box) mounted for testing. e) Faraday cage with lid removed to expose contents.

but specific peaks were not the same. Beyond those similarities every vibration source had a unique spectra. For power spectral density plots of all 23 vibration sources shown in the table, see Appendix A.

The characteristics of these ambient vibration sources over time are of interest since energy harvesters are intended for long-term use. Each vibration source in this study was measured several times over minutes/hours and weeks/months. The data suggest that the peak frequencies in the spectra do not vary over time, but the relative magnitudes of the frequencies can change significantly. This can be a result of duty cycles of equipment and differences in system settings. See Appendix A for graphs illustrating this variation over time. Additionally, the vibration characteristics can be sensitive to spatial location.

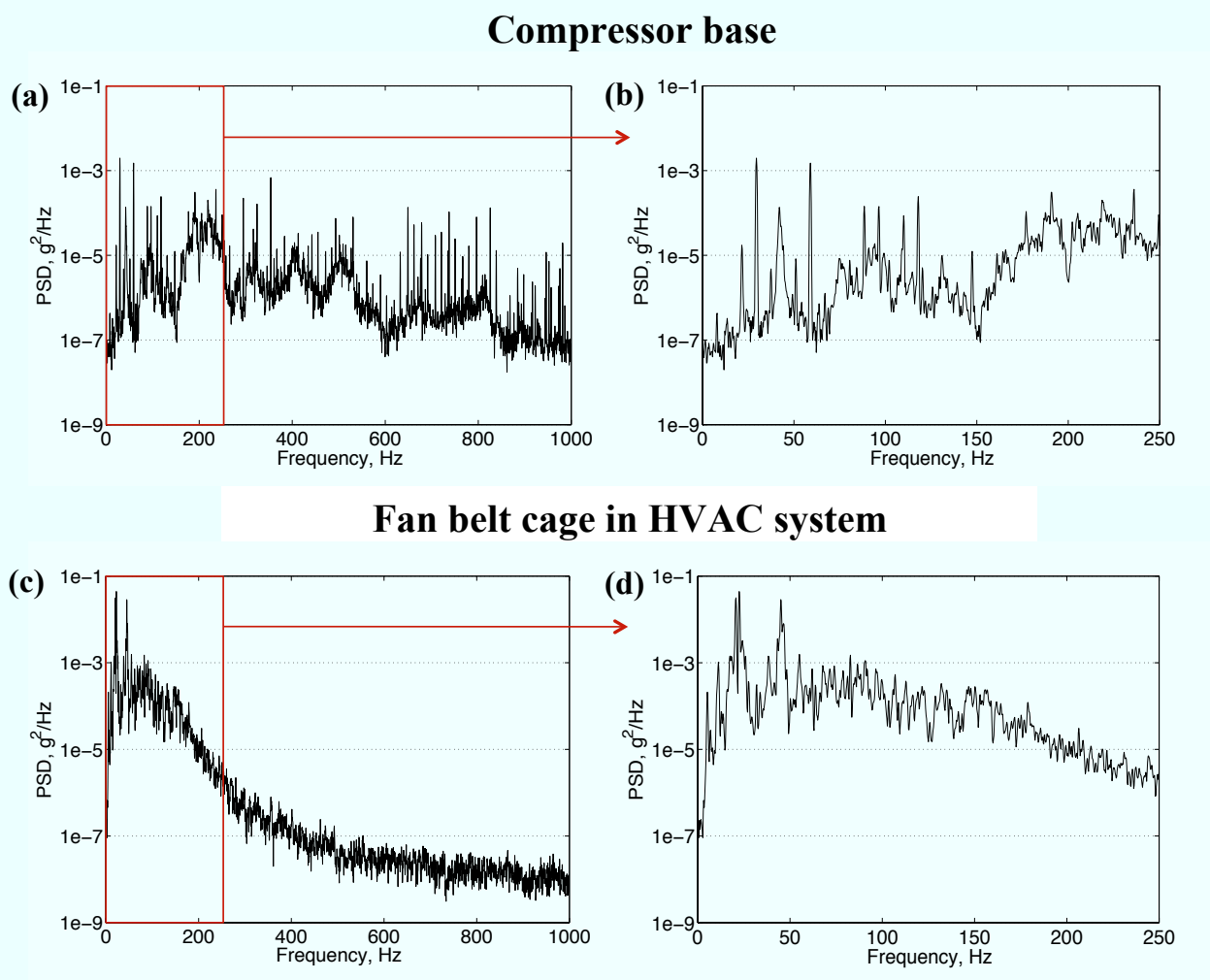

Figure 2.2: Acceleration PSD vs frequency on a semi-log scale for: a) and b) compressor base, c) and d) fan belt cage. b) and d) show close up of the area of interest where acceleration magnitude is highest. Dominant frequency peaks for the compressor are 30, 60, and 354 Hz and for the fan belt are 20, 22, and 45 Hz.

Chapter 3

Fixed-Frequency Piezoelectric Energy Harvester: Model

3.1 Modeling piezoelectric harvester response to arbitrary vibration input

This chapter, which is adapted from [43], develops a model for the response of the piezoelectric energy harvester to an arbitrary input excitation. For example, the input excitation may be a sine wave, as in a laboratory test, or may be a complicated machine vibration such as those presented in the previous chapter, as in real-world operation. The model developed here differs from previous research by including a trapezoidal beam shape and accounting for the rotational inertia of the proof mass, rather than treating it as a point mass as has been done in other work [17]. This model is simpler than many dynamical models of energy harvesters in that the proof mass to beam mass ratio is high enough that the beam can be treated quasi-statically as opposed to using the more complicated orthogonal function expansion as is done in [15]. Finally, a discretization method is used to solve the model equations with sampled acceleration inputs.

3.1.1 General energy harvester configuration

The configuration of the energy harvester is shown in Figure 3.1. The geometry of the cantilevers used in this study is described by w_o, width of the beam where it connects to the mass, y_o, additional width at the base, L_b, beam length, and L_m, mass length. The width at an arbitrary location along the beam, $W(x)$, and the surface area, A_s, are given by (3.1) and (3.2).

$$W(x) = w_\mathrm{o} + 2y_\mathrm{o}\left(1 - \frac{x}{L_\mathrm{b}}\right) \tag{3.1}$$

$$A_\mathrm{s} = (w_0 + y_0)\, L_\mathrm{b} + L_\mathrm{m}^2 \tag{3.2}$$

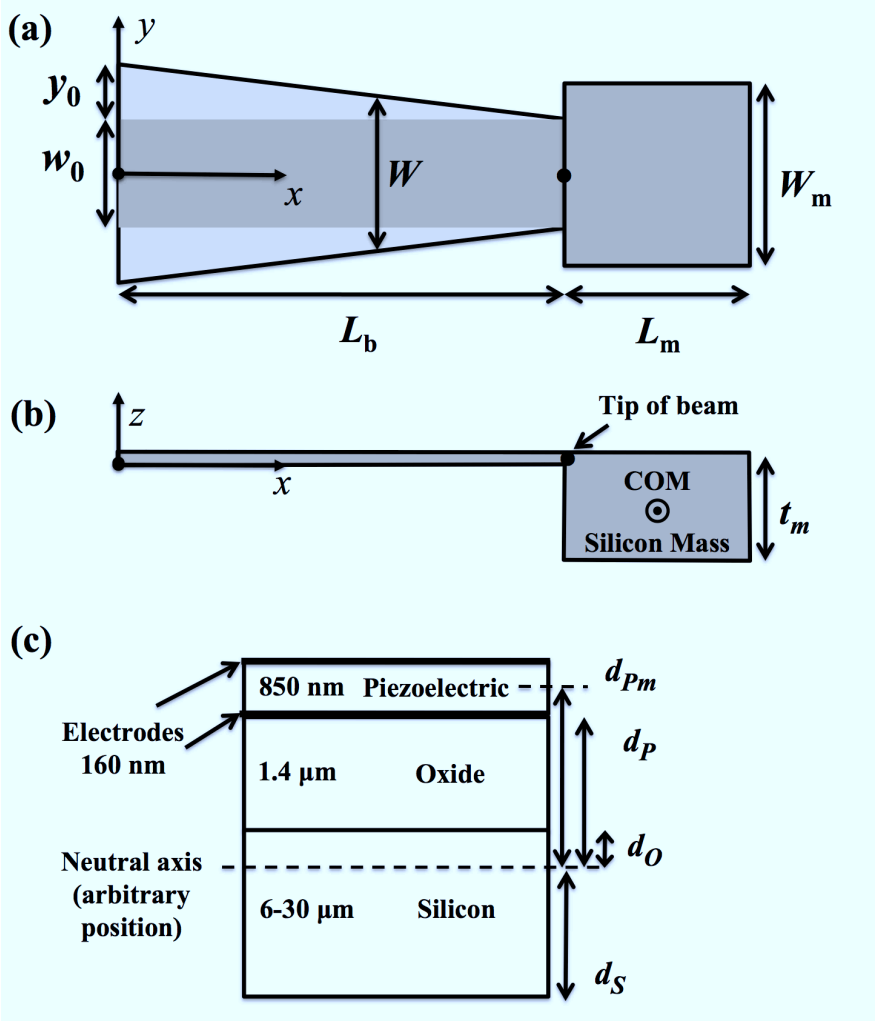

Figure 3.1: Schematic of the energy harvester (not to scale). a) top view, b) side view, c) cross section and layer thicknesses. The subscripts P, O, and S refer to piezoelectric, oxide, and silicon layers, respectively.

In this design L_{m} and W_{m}, the width of the mass, are equal. The beam tapering is characterized by δ, as defined by (3.3).

$$\delta = \frac{2y_0}{(2y_0 + w_0)} \tag{3.3}$$

If the beam is rectangular rather than trapezoidal, then δ will be zero.

3.1.2 Piezoelectric cantilever beam equations.

The goal in the next two sections is to derive expressions for the forces and moments on a beam calculated at the center of the proof mass in terms of geometry, material properties, loading conditions, and input acceleration. The method used closely follows that of [20]. The mechanical contribution from the thickness of the electrodes is neglected such that only the piezoelectric, oxide, and silicon layers are considered.

Using the Euler-Bernoulli assumptions that plane sections remain plane and neglecting shear stresses, the strain in the x-direction is given by

$$S_1 = \frac{d\xi}{dx} - z\frac{d^2\eta}{dx^2} \tag{3.4}$$

where S_1 is strain, ξ is displacement in the x-direction, η is displacement in the z-direction relative to the x-direction, and z is distance from the neutral axis. $\frac{d\xi}{dx}$ is strain due to axial force and $z\frac{d^2\eta}{dx^2}$ is strain due to curvature.

The full coupled constitutive piezoelectric equations can be found in [29]. For beam bending, these can be reduced to a simpler form. Since the beams are slender, we use the plane stress equations for a narrow beam as opposed to the plane strain equations applicable for beams with width nearly equal to length, see e.g. [62]. The reduced equations are

$$S_1 = s_{11}^E T_1 + d_{31} E_3 \tag{3.5}$$

$$D_3 = d_{31} T_1 + \varepsilon_{33}^T E_3 \tag{3.6}$$

where s_{11}^E is compliance at constant electric field, T_1 is stress, d_{31} is piezoelectric coefficient, E_3 is electric field, D_3 is electric displacement field, and ε_{33}^T is permittivity at constant stress. The subscript 1 denotes the length direction of the beam, x, while 3 denotes the thickness direction, z. Solving (3.5) for T_1 and substituting into (3.6) gives

$$D_3 = E_{\mathrm{P}} d_{31} S_1 + \varepsilon_{33}^T \left(1 - k_{31}^2\right) E_3 \tag{3.7}$$

$$\text{where} \quad k_{31}^2 = \frac{d_{31}^2 E_{\mathrm{P}}}{\varepsilon_{33}^T} \tag{3.8}$$

E_{P} is modulus of elasticity of the piezoelectric layer, which is $(s_{11}^E)^{-1}$, and k_{31}^2 is piezoelectric coupling coefficient. Electric displacement is independent of z from Gauss's Law and is therefore given entirely by the boundary condition

$$D_3(x, z) = -\sigma(x) \tag{3.9}$$

where σ is surface charge density. Substituting (3.4) into (3.7), and into (3.9), and integrating across the thickness of the piezoelectric layer from bottom to top yields

$$\sigma = -E_{\mathrm{P}} d_{31} \left(\frac{d\xi}{dx} - d_{\mathrm{Pm}}\frac{d^2\eta}{dx^2}\right) + \frac{\varepsilon_{33}^T \left(1 - k_{31}^2\right) V}{t_{\mathrm{P}}} \tag{3.10}$$

$$\text{where} \quad d_{\mathrm{Pm}} = d_{\mathrm{P}} + \frac{t_{\mathrm{P}}}{2} \tag{3.11}$$

and V is voltage, t_{P} is thickness of the piezoelectric layer, d_{Pm} is the distance from the neutral axis to the middle of the piezoelectric layer, and d_{P} is defined as the z position from the neutral axis to the bottom of the piezoelectric layer, as illustrated in figure 3.1c. Substituting (3.4), (3.9) and (3.10) into (3.7) and solving for electric field gives (3.12).

$$E_3 = \frac{E_{\mathrm{P}} d_{31}}{\varepsilon_{33}^{T}\left(1 - k_{31}^2\right)}\left(z - d_{\mathrm{Pm}}\right)\frac{d^2\eta}{dx^2} - \frac{V}{t_{\mathrm{P}}} \tag{3.12}$$

An expression for stress in the piezoelectric layer can be found by solving (3.5) for T_1 and inserting (3.4) and (3.12) into it.

$$T_1 = E_{\mathrm{P}}\left[\frac{d\xi}{dx} - \frac{d^2\eta}{dx^2}\left(d_{\mathrm{Pm}} + \frac{\left(z - d_{\mathrm{Pm}}\right)}{\left(1 - k_{31}^2\right)}\right) + \frac{d_{31}V}{t_{\mathrm{P}}}\right] \tag{3.13}$$

Axial force and bending moment can be found at position x for cross section area $A(x)$ using (3.14) and integrating over the thickness of the beam [29].

$$P = \int\int_A T_1 dydz, \quad M = -\int\int_A zT_1 dydz \tag{3.14}$$

The expression for d_{P} is still unknown, so d_{Pm} is unknown and P and M cannot be calculated. An equation for d_{P} can be derived by using the definition of the neutral plane: terms in the P expression proportional to $\frac{d^2\eta}{dx^2}$ should equal zero, as should terms in the M expression proportional to $\frac{d\xi}{dx}$. Both sets of terms that should equal zero have a common factor, - $w\left(E_{\mathrm{P}} t_{\mathrm{P}} d_{\mathrm{Pm}} + E_{\mathrm{O}} t_{\mathrm{O}} d_{\mathrm{Om}} + E_{\mathrm{S}} t_{\mathrm{S}} d_{\mathrm{Sm}}\right)$, where E_{S}, E_{O}, t_{S}, and t_{O} are the modulus of elasticity and thickness of the silicon and oxide layers. We can write d_{Pm} (equation (3.11)), d_{Om}, and d_{Sm} in terms of d_{P} and the known layer thicknesses (see figure 3.1c):

$$d_{\mathrm{Om}} = d_{\mathrm{P}} - \frac{t_{\mathrm{O}}}{2}, \quad d_{\mathrm{Sm}} = d_{\mathrm{P}} - t_{\mathrm{O}} - \frac{t_{\mathrm{S}}}{2}. \tag{3.15}$$

Substituting (3.15) into the common factor and setting it equal to zero allows us to solve for d_{P}:

$$d_{\mathrm{P}} = \frac{E_{\mathrm{S}} t_{\mathrm{S}} t_{\mathrm{O}} - \frac{1}{2}\left(E_{\mathrm{P}} t_{\mathrm{P}}^2 - E_{\mathrm{O}} t_{\mathrm{O}}^2 - E_{\mathrm{S}} t_{\mathrm{S}}^2\right)}{E_{\mathrm{P}} t_{\mathrm{P}} + E_{\mathrm{O}} t_{\mathrm{O}} + E_{\mathrm{S}} t_{\mathrm{S}}}. \tag{3.16}$$

Now it is possible to solve the force and moment equations, which can be conveniently parameterized as follows:

$$P = K_{\mathrm{A}}\frac{d\xi}{dx} + JV, \quad M = K_{\mathrm{B}}\frac{d^2\eta}{dx^2} - GV \tag{3.17}$$

where K_{A} is axial rigidity, K_{B} is flexural rigidity, J is force per voltage, and G is moment per voltage. They are defined as follows, where superscript O represents the expression for a beam with $\delta = 0$.

$$K_{\mathrm{A}} = \left(1 - \delta\frac{x}{L_{\mathrm{b}}}\right) K_{\mathrm{A}}^{O}, \quad K_{\mathrm{B}} = \left(1 - \delta\frac{x}{L_{\mathrm{b}}}\right) K_{\mathrm{B}}^{O} \tag{3.18}$$

$$J = \left(1 - \delta\frac{x}{L_b}\right) J^{O}, \quad G = \left(1 - \delta\frac{x}{L_b}\right) G^{O} \tag{3.19}$$

$$K_{\mathrm{A}}^{O} = w\left(E_{\mathrm{P}}t_{\mathrm{P}} + E_{\mathrm{O}}t_{\mathrm{O}} + E_{\mathrm{S}}t_{\mathrm{S}}\right) \tag{3.20}$$

$$J^{O} = wE_{\mathrm{P}}d_{31} \tag{3.21}$$

$$\begin{aligned} K_{\mathrm{B}}^{O} = w\Bigg[&E_{\mathrm{P}}\left(t_{\mathrm{P}}d_{\mathrm{Pm}}^{2} + \frac{t_{\mathrm{P}}^{3}}{12\left(1 - k_{31}^{2}\right)}\right) \\ &+ E_{\mathrm{O}}\left(t_{\mathrm{O}}d_{\mathrm{Om}}^{2} + \frac{t_{\mathrm{O}}^{3}}{12}\right) \\ &+ E_{\mathrm{S}}\left(t_{\mathrm{S}}d_{\mathrm{Sm}}^{2} + \frac{t_{\mathrm{S}}^{3}}{12}\right)\Bigg] \end{aligned} \tag{3.22}$$

$$G^{O} = wE_{\mathrm{P}}d_{31}d_{\mathrm{Pm}} = d_{\mathrm{Pm}}J^{O} \tag{3.23}$$

Thus far we have been considering forces and moments at any point along the beam, but we are specifically interested in the forces and moments at the tip of the beam where it connects with the mass, denoted by the subscript a, as shown in expression (3.24), where F is vertical force.

$$F = F_{\mathrm{a}}, \quad M = M_{\mathrm{a}} + \left(L - x\right)F_{\mathrm{a}}, \quad P = P_{\mathrm{a}} \tag{3.24}$$

At this point, vertical displacement, $\eta_{\mathrm{a}} = \eta\left(L_{\mathrm{b}}\right)$, and rotation, $\theta_{\mathrm{a}} = \eta'\left(L_{\mathrm{b}}\right)$, at the tip of the beam can be found by substituting M in (3.24) into (3.17) and solving for η with boundary conditions $\eta(0) = 0$ and $\eta'(0) = 0$, where $x = 0$ corresponds to the base of the beam. Similarly, axial displacement of the tip, $\xi_{\mathrm{a}} = \xi\left(L_{\mathrm{b}}\right)$, can be found by substituting P in (3.24) into (3.17) and solving for ξ, subject to boundary condition $\xi(0) = 0$. Finally, axial force and moment equations for the tip of the beam can be solved for $\frac{d\xi}{dx}$ and $\frac{d^2\eta}{dx^2}$ and inserted into (3.10) so that the equation is in terms of the mechanical loads. Integrating the surface charge density over area then gives the charge on the top electrode, q. These equations can be represented as

$$\begin{pmatrix} \eta_{\mathrm{a}} \\ \theta_{\mathrm{a}} \\ q \\ \xi_{\mathrm{a}} \end{pmatrix} = \begin{pmatrix} c_{\mathrm{t}} & c_{\mathrm{c}} & \beta_{\mathrm{t}} & 0 \\ c_{\mathrm{c}} & c_{\mathrm{r}} & \beta_{\mathrm{r}} & 0 \\ \beta_{\mathrm{t}} & \beta_{\mathrm{r}} & C & \beta_{\mathrm{a}} \\ 0 & 0 & \beta_{\mathrm{a}} & c_{\mathrm{a}} \end{pmatrix} \begin{pmatrix} F_{\mathrm{a}} \\ M_{\mathrm{a}} \\ V \\ P_{\mathrm{a}} \end{pmatrix} \tag{3.25}$$

where the coefficients are

$$c_{\mathrm{t}} = \left[\frac{9}{2\delta} - \frac{3}{\delta^2} - \frac{3\left(1-\delta\right)^2}{\delta^3}\ln\left(1-\delta\right)\right] c_{\mathrm{t}}^O \tag{3.26}$$

$$c_{\mathrm{c}} = \left[\frac{2}{\delta} - \frac{2\left(1-\delta\right)}{\delta^2}\ln\left(1-\delta\right)\right] c_{\mathrm{c}}^O \tag{3.27}$$

$$c_{\mathrm{t}}^O = \frac{L_{\mathrm{b}}^3}{3K_{\mathrm{B}}^O}, \quad c_{\mathrm{c}}^O = \frac{L_{\mathrm{b}}^2}{2K_{\mathrm{B}}^O} \tag{3.28}$$

$$c_{\mathrm{r}} = \left[\frac{1}{\delta}\ln\left(1-\delta\right)\right] c_{\mathrm{r}}^O, \quad c_{\mathrm{r}}^O = \frac{L_{\mathrm{b}}}{K_{\mathrm{B}}^O} \tag{3.29}$$

$$c_{\mathrm{a}} = \left[\frac{1}{\delta}\ln\left(1-\delta\right)\right] c_{\mathrm{a}}^O, \quad c_{\mathrm{a}}^O = \frac{L_{\mathrm{b}}}{K_{\mathrm{A}}^O} \tag{3.30}$$

$$\beta_{\mathrm{t}} = c_{\mathrm{c}}^O G^O, \quad \beta_{\mathrm{r}} = c_{\mathrm{r}}^O G^O, \quad \beta_{\mathrm{a}} = -c_{\mathrm{a}}^O J^O \tag{3.31}$$

$$C = \left[1 - \frac{1}{2}\delta\right] C^O \tag{3.32}$$

$$C^O = \frac{\varepsilon_{33}^T\left(1-k_{31}^2\right)A_{\mathrm{s}}}{t_{\mathrm{P}}} + c_{\mathrm{r}}^O\left(G^O\right)^2 + c_{\mathrm{a}}^O\left(J^O\right)^2 \tag{3.33}$$

In order to express the equations in terms of stiffnesses rather than compliances, we can re-write (3.25) as

$$f_{\mathrm{a}} = K_{\mathrm{SC}} u_{\mathrm{a}} - \Gamma V \tag{3.34}$$

$$q = \Gamma^T u_{\mathrm{a}} + C_{\mathrm{CL}} V \tag{3.35}$$

where

$$f_{\mathrm{a}} = \begin{pmatrix} F_{\mathrm{a}} \\ M_{\mathrm{a}} \\ P_{\mathrm{a}} \end{pmatrix}, u_{\mathrm{a}} = \begin{pmatrix} \eta_{\mathrm{a}} \\ \theta_{\mathrm{a}} \\ \xi_{\mathrm{a}} \end{pmatrix} \tag{3.36}$$

$$K_{\mathrm{SC}} = \begin{pmatrix} k_{\mathrm{t}} & k_{\mathrm{c}} & 0 \\ k_{\mathrm{c}} & k_{\mathrm{r}} & 0 \\ 0 & 0 & k_{\mathrm{a}} \end{pmatrix} = \begin{pmatrix} c_{\mathrm{t}} & c_{\mathrm{c}} & 0 \\ c_{\mathrm{c}} & c_{\mathrm{r}} & 0 \\ 0 & 0 & c_{\mathrm{a}} \end{pmatrix}^{-1} \tag{3.37}$$

$$\Gamma = \begin{pmatrix} \gamma_{\mathrm{t}} \\ \gamma_{\mathrm{r}} \\ \gamma_{\mathrm{a}} \end{pmatrix} = \begin{pmatrix} k_{\mathrm{t}}\beta_{\mathrm{t}} + k_{\mathrm{c}}\beta_{\mathrm{r}} \\ k_{\mathrm{c}}\beta_{\mathrm{t}} + k_{\mathrm{r}}\beta_{\mathrm{r}} \\ k_{\mathrm{a}}\beta_{\mathrm{a}} \end{pmatrix} \tag{3.38}$$

$$C_{\mathrm{CL}} = C - k_{\mathrm{t}}\beta_{\mathrm{t}}^2 - 2k_{\mathrm{c}}\beta_{\mathrm{t}}\beta_{\mathrm{r}} - k_{\mathrm{r}}\beta_{\mathrm{r}}^2 - k_{\mathrm{a}}\beta_{\mathrm{a}}^2. \tag{3.39}$$

Here, K_{SC} is short circuit stiffness, Γ is the piezoelectric transduction factor, and C_{CL} is the clamped capacitance.

3.1.3 Equations of motion.

The effect of the proof mass can now be incorporated into the equations describing beam motion. The forces and moments acting on the center of the proof mass include those from the tip of the beam, from fictitious force due to gravity at the center of the mass, and damping. In this analysis it is assumed that the dynamic behavior of the beam can be ignored since the beam resonance frequency is much higher than that of the beam with the mass attached. The validity of this assumption was checked by calculating the eigenfrequencies for each case.

The mass matrix is

$$M = \begin{pmatrix} m & 0 & 0 \\ 0 & I_{\mathrm{c}} & 0 \\ 0 & 0 & m \end{pmatrix} \tag{3.40}$$

where I_{c} is moment of inertia and m the mass of the proof mass. Equation (3.41) is used to transform the axial, vertical, and rotational displacement variables from the tip of the beam (subscript a) to the center of the proof mass (subscript c) such that $u_{\mathrm{a}} = L_{\mathrm{a}} u_{\mathrm{c}}$. The geometric relationship between the tip of the beam and the center of mass (COM) can be seen in figure 3.1b, where L_{m}, t_{m}, and COM are defined.

$$L_{\mathrm{a}} = \begin{pmatrix} 1 & \frac{-L_{\mathrm{m}}}{2} & 0 \\ 0 & 1 & 0 \\ 0 & \frac{-t_{\mathrm{m}}}{2} + d_{\mathrm{Pb}} & 1 \end{pmatrix} \tag{3.41}$$

Similarly, Γ and K_{SC} must be transformed from the tip of the beam to the center of proof mass and this is given by $\Gamma = L_{\mathrm{a}}\Gamma_{\mathrm{c}}$ and $K_{\mathrm{SC}} = L_{\mathrm{a}} K_{\mathrm{SC,c}}$. Since Γ and K_{SC} are 3x1 and 3x3 matrices respectively, Γ_{c} and $K_{\mathrm{SC,c}}$ are

$$\Gamma_{\mathrm{c}} = L_{\mathrm{a}}^T \Gamma, \quad K_{\mathrm{SC,c}} = L_{\mathrm{a}}^T K_{\mathrm{SC}} L_{\mathrm{a}}. \tag{3.42}$$

The fictitious force, f_{c}, is given by

$$f_{\mathrm{c}} = \begin{pmatrix} -ma \\ 0 \\ 0 \end{pmatrix} \tag{3.43}$$

where a is the acceleration of the ambient vibration source, which is a function of time and may be measured experimentally. Damping must now be determined. First, we must calculate the 3x3 full matrix of the eigenvectors of $K_{\mathrm{SC,c}}$ and M, denoted by W, and the three corresponding eigenfrequencies ω_j, where $j = 1, 2, 3$. From [61], for example, the eigenvectors can be given a normalization

$$W^T M W = n. \tag{3.44}$$

Now damping for each mode can be calculated from

$$b_j = \frac{1}{Q_j}\omega_j n(j,j), \quad j = 1,2,3 \tag{3.45}$$

where Q_j is the quality factor and is measured experimentally. The full damping matrix is given by

$$D = W^{T^{-1}} \begin{bmatrix} b_1 & 0 & 0 \\ 0 & b_2 & 0 \\ 0 & 0 & b_3 \end{bmatrix} W^{-1}. \tag{3.46}$$

Rewriting (3.34) and (3.35) for the center of the proof mass rather than the tip of the beam, the equations of motion are

$$M\ddot{u}_\mathrm{c} = -K_{\mathrm{SC,c}}u_\mathrm{c} - D\dot{u}_\mathrm{c} + \Gamma_\mathrm{c}V + f_\mathrm{c} \tag{3.47}$$

$$q = \Gamma_\mathrm{c}^T u_\mathrm{c} + C_\mathrm{CL}V. \tag{3.48}$$

Finally, in this study the electrical load used is simply a resistor, with Ohm's Law as

$$V = -R\dot{q}. \tag{3.49}$$

3.1.4 Discretization equations for incorporating measured ambient vibration into the model.

The equations that have been presented thus far are continuous, yet we are interested in using discrete experimental acceleration data as an input to the model. Therefore, in order to produce a model that can accept the discrete input data we need to discretize the differential equations that describe the energy harvester response. The first step is to write the equations of motion as a system of three first-order differential equations.

$$\dot{u}_\mathrm{c} = p \tag{3.50}$$

$$\begin{aligned} \dot{p} \; = & -\left(M^{-1}K_{\mathrm{SC,c}} + \frac{M^{-1}\Gamma_\mathrm{c}\Gamma_\mathrm{c}^T}{C_\mathrm{CL}}\right)u_\mathrm{c} \\ & - M^{-1}D\dot{u}_\mathrm{c} + \frac{M^{-1}\Gamma_\mathrm{c}}{C_\mathrm{CL}}q + M^{-1}f_\mathrm{c} \end{aligned} \tag{3.51}$$

$$\dot{q} \; = \frac{\Gamma_\mathrm{c}^T}{C_\mathrm{CL}R}u_\mathrm{c} - \frac{1}{C_\mathrm{CL}R}q \tag{3.52}$$

The system of equations can be represented by the general formula

$$\dot{X} = -AX + B \tag{3.53}$$

where X is the column matrix of state variables u_c, p, and q. A is a 7x7 matrix of constants from equations (52) including mass, stiffness, and damping, and B is a 7x1 matrix containing the acceleration input. Note that A is independent of time but B is time dependent. In discretized form, (3.53) can be written as shown in (3.54) and (3.55) so that the beam response can be computed numerically from the input acceleration.

$$X(t_n) = e^{-A(t_n - t_0)} X(t_0) + \int_{t_0}^{t_n} e^{-A(t_n - \tau)} B(\tau) d\tau \tag{3.54}$$

$$X(t_{n+1}) = e^{-A(t_{n+1} - t_n)} X(t_n) + \int_{t_n}^{t_{n+1}} e^{-A(t_{n+1} - \tau)} B(\tau) d\tau \tag{3.55}$$

This method is exact to machine precision for a piecewise linear driving force. Further details on discretization and linear algebra can be found in [8] and [61], respectively, and appendix B of this document contains detailed steps on the discretization process used here.

3.2 Summary

In this chapter, a model for fixed-frequency piezoelectric energy harvesters that accounts for rotation of the proof mass and accepts arbitrary measured acceleration data as an input was developed. In chapter 4, the predictions of this model will be compared with experimental energy harvester response to validate the model. In chapter 6 this model will be used to perform an optimization on the energy harvester.

Chapter 4

Fixed-Frequency MEMS Piezoelectric Harvester: Design, Fabrication, & Results

4.1 Device design

The focus of this chapter is the fabrication of energy harvesters that function on ambient vibration sources, as opposed to focusing on the production of a specified power output. The successful micro-fabrication of energy harvesters with resonance frequencies of 31 – 232 Hz is presented. This frequency range coincides with the dominant frequencies of most vibration sources surveyed as reported in chapter 2. The energy harvesters are characterized on a vibrometer at low accelerations of 0.03 – 0.7 g and are then deployed in a machine room to harvest energy from industrial ambient vibration sources. The experimental energy harvester output is then compared with the model from chapter 3. This chapter is adapted from [43].

Based on the data collected in the survey of ambient vibrations, most of the vibration energy that is available to harvest is at frequencies of 20 – 200 Hz with accelerations under 0.7 g/$\sqrt{Hz}$. Therefore, the energy harvesters were designed with large beam lengths and masses with the goal of achieving resonance frequencies under 200 Hz for compatibility with low frequency ambient input vibrations. Dimensions of the fabricated cantilevers are given in Table 4.1. Various dimensions of Si mass were used, along with various beam lengths and different degrees of beam tapering, solely to achieve a range of resonance frequencies for testing devices on ambient vibrations sources with different frequencies. Beams were fabricated in rectangular and trapezoidal geometries, which are of interest due to their increased resistance to shocks compared with rectangular beams [17]. A direct comparison of the performance of rectangular versus trapezoidal beams was outside the scope of this study. However, it was observed that trapezoidal beams survived the shocks and impulses of handling and testing better than rectangular beams. This is due to the fact that the highest

Table 4.1: Energy harvester dimensions.

Harvester ID	L_b (μm)	L_m (μm)	w_o (μm)	y_o (μm)	A_s (mm^2)
1	3500	2500	480	400	9.33
2	3000	3000	450	0	10.35
3	3500	2500	480	400	9.33
4	4500	1500	530	395	6.41
5	3000	3000	450	395	11.54
6	4500	1500	530	0	4.64
7	4500	1500	530	0	4.64
8	4500	1500	530	395	6.41

stress in a cantilever beam is at the base, so increasing the width of the beam at the base allows the force to be distributed over a larger area, thereby reducing the stress.

4.2 Device fabrication

MEMS energy harvesters were fabricated in order to test the model. Silicon (001) p-type test wafers were thermally oxidized with a layer 1.4 μm thick, followed by sputter deposition of 10/150 nm of Ti/Pt as a bottom electrode. Sol-gel lead zirconate titanate (PZT) films were spin-coated onto the wafer, as described in [42], to achieve a film 850 nm thick. Cantilever beams were fabricated from these PZT films. The first lithography mask defined the 10/150 nm Cr/Pd electron beam evaporated top electrodes. Second-level lithography used an HF etch to expose the bottom electrodes. The third mask defined the outline of the cantilever using argon ion beam milling, and the fourth lithography step used deep reactive ion etching (DRIE) to construct the mass, dice the wafer, and partially release the energy harvesting cantilever beam from the backside. Final release of the beam was achieved with a XeF_2 dry etch. Figure 4.1 shows the microfabrication process.

The material properties used as input to the model for all cantilevers are reported in Table 4.2. Elastic moduli, permittivity, and density are obtained from the literature [12, 26]. The energy harvesters were mounted on custom printed circuit boards (PCB) for testing. Wirebonds were used to make electrical connections from the harvester electrodes to the PCB, and a Bourns 3314 variable resistor was used for the load, as shown in Figure 4.2. All of the components on the circuit board were surface-mounted so the PCB could be attached flush with the vibrating surface.

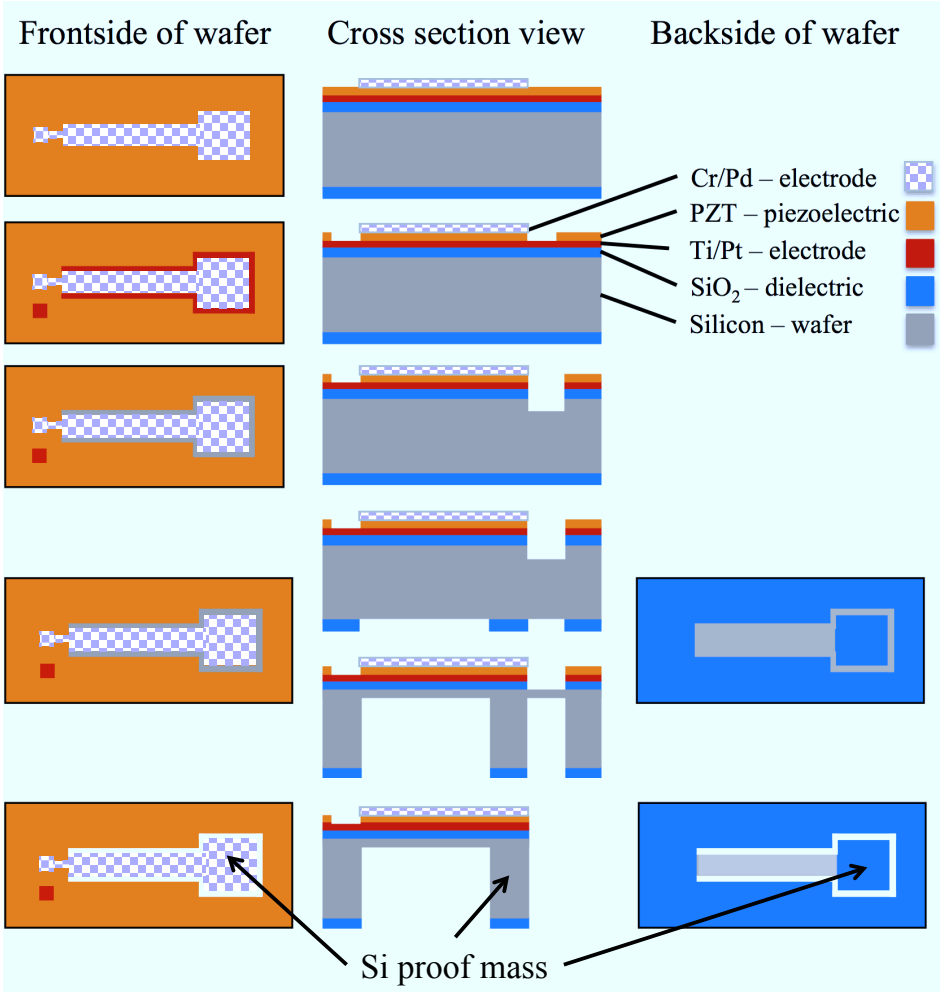

Figure 4.1: Microfabrication process steps. From top to bottom: patterning of top electrode, HF etch to reveal bottom electrode, Ar ion mill etch to define cantilever outline, DRIE oxide etch to expose Si, DRIE Si etch to partially release beam and leave a Si mass, and finally a XeF_2 etch to finish the cantilever release.

4.3 Experimental methods

4.3.1 Harvester characterization on vibrometer

The energy harvesters were characterized on a Labworks ET-126 vibrometer driven by a Labworks SC-121 sine servo controller and Labworks pa-138 power amplifier. Harvester output was recorded at a sampling rate of 1000 Hz using a NI USB-6221 data acquisition device. Analysis was done in MATLAB. Capacitance of each beam was measured directly using an Amprobe 37XR-A meter.

Table 4.2: Model parameters common to all energy harvesting cantilever beams.

Term	Units	Value
t_{P}	μm	0.85
t_{O}	μm	1.4
t_{Wafer}	μm	525
E_{P}	GPa	110
E_{O}	GPa	60
E_{S}	GPa	170
ϵ_{P}	nF/m	11
ρ_{S}	kg/m^3	2330

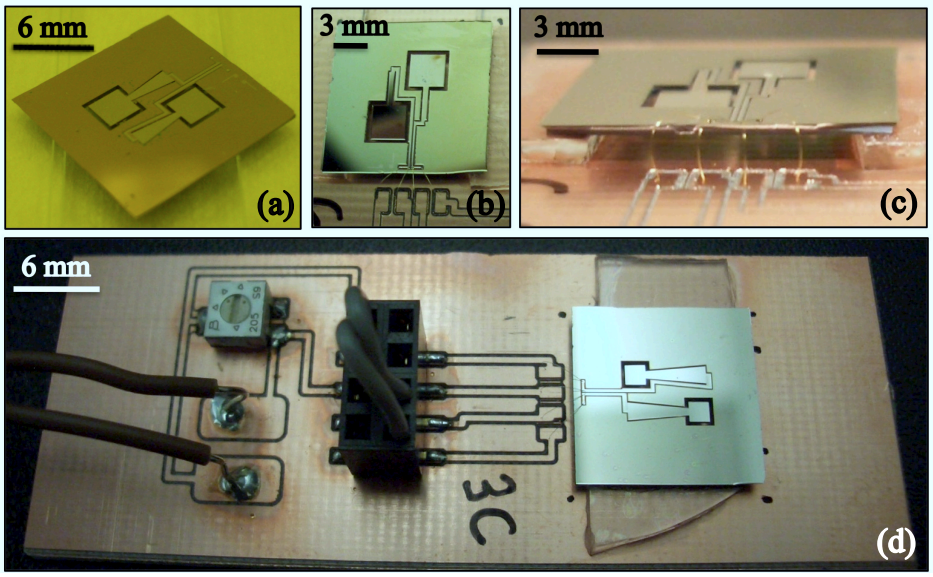

Figure 4.2: Three different energy harvesters: a) cantilever beam 3, b and c) beam 2 top & side views, d) beam 8 mounted on PCB and connected to load resistor.

Frequency sweeps were conducted manually with a step size of 0.1 Hz and a 15 second pause for settling between tests. Quality factor, Q, was determined from the power output vs frequency curve. Load resistance sweeps were done at the harvesters' resonance frequency to obtain R_{opt}. An acceleration sweep was conducted at f_{n} and R_{opt}. Tests were done at various accelerations, from 0.03 to 0.7 g, to mimic the range of most ambient vibration accelerations.

4.3.2 Harvester testing on ambient sources

The energy harvester/PCB assembly was mounted inside a Faraday cage to minimize electrical noise, and was magnetically mounted to the vibrating surfaces. Electrode leads were connected by BNC cable to the data acquisition system described in 4.3.1. An accelerometer was mounted near the harvester while data were collected, as described in chapter 2. Harvesters were tested on 8 out of the 23 vibration sources surveyed, as indicated in Table 2.1, but not all harvesters were tested on all 8 sources. In total, 38 different tests of energy harvesting from an ambient vibration source were conducted.

4.3.3 Model calibration

All model parameters except t_S and d_{31} were known by design, estimated from the literature, or determined with direct experimentation. t_S could not be measured directly without destroying the harvester and was not known by design due to variability across the wafer in the DRIE etch. An oxide etch stop layer will be used in future work to address this issue. d_{31} was measured before the PZT films were etched but it can degrade during MEMS-processing. Also, the effective d_{31} of a large area device is different than that measured over a 50 μm-diameter electrode.

The values of t_S and d_{31} for each harvester were determined by conducting frequency sweeps on the vibrometer at known input frequency and acceleration and comparing the results to a simulated frequency sweep run on the model with the same input conditions. The Q value was determined from the shape of the response, i.e. center frequency divided by the full bandwidth at half maximum. Q is not dependent on the measured amplitude, only the relative bandwidth. Q is also independent of d31 if the coupling is weak enough, which is valid for the devices in this study ($k_{31}^2 Q$ on the order of 0.01 – 0.2). With weak coupling and Q fixed, t_S is entirely given by the center frequency. The only remaining variable to adjust is then d_{31} to get the correct amplitude.

Resistance and acceleration sweeps on the vibrometer were then conducted and experimental results were compared with the model to ensure that the fitted t_S and d_{31} values were appropriate. After verification with controlled vibrometer testing, the model was used to look at harvester response to ambient vibration input.

4.4 Results

4.4.1 Harvester characterization on vibrometer

Energy harvesters with low resonance frequencies were successfully fabricated using MEMS processes. Figure 4.3a shows measured average power output normalized by input acceleration versus frequency for all 8 of the harvesters, with output of 1.2 – 43.8 $\mathrm{nW_{avg}}/g^2$ and f_n of 31 – 232 Hz. Figure 4.3b shows the results of a frequency sweep on harvester beam 8,

Table 4.3: Harvester properties determined from vibrometer tests.

Harvester ID	f_n (Hz)	Q	R_{opt} (kΩ)	d_{31}, fitted (pm/V)	t_S, fitted (μm)	C (nF)	a (g)	P_{avg} (nW)	P_{avg}/a^2 (nW/g^2)
1	31	80	42	18.0	7.85	121	0.3	0.25	2.78
2	40.3	350	32	7.0	14.00	129	0.048	0.003	1.15
3	85.8	182	18	1.9	17.10	105	0.166	0.29	10.35
4	153.7	350	10	5.0	20.95	105	0.048	0.03	11.76
5	169.5	210	8	6.5	30.19	142	0.18	1.42	43.83
6	177.9	290	22	2.5	27.08	49	0.164	0.30	11.00
7	192.8	320	15	1.9	28.64	64	0.149	0.06	2.84
8	232.0	415	9	3.2	25.65	80	0.29	1.72	20.5

where output voltage is 4.6 mV_{rms} and power is 1.72 nW_{avg}. Figure 4.3c shows a resistance sweep on beam 3, where R_{opt} is 8.5 kΩ. After this sweep was conducted beam 3 was etched for several more cycles, which decreased t_S, decreased f_n, and increased R_{opt} to the values reported in Table 4.3. Figure 4.3d shows an acceleration sweep on beam 6. Figures 4.3b-d show that the experiment and model are in close agreement for tests on the vibrometer.

Table 4.3 summarizes the properties for all 8 harvesters. The power output from beams tested on the vibrometer at f_n was 1.2 – 43.8 nW_{avg}/g^2. The varying performance of the harvesters, even with the same geometry, is due in part to different Q values and in part to the fact that the d_{31} value is different for each beam. The different d_{31} values for beams from the same wafer are due to variations in the quality of the piezoelectric film across the wafer. Another factor in varying performance is that harvester #1 is from a different wafer than the others, and it struck the sample holder when excited at resonance due to a mounting misalignment, significantly reducing its power output. Additionally, beams with the same areal geometry still have differing t_S values, which impacts performance.

The devices in this study have very weak coupling, as described in section 4.3.3. Given such a low coupling, the piezoelectric coefficient and the quality factor have very little impact on the resonance frequency of the device compared to geometric parameters. The resonance frequency of the devices in this study is much more dependent on t_S, L_b, L_m, δ, and w_o.

Figure 4.4 shows a comparison of the f_n and test acceleration of the 8 energy harvesters in this study compared to others in the literature and to the acceleration and frequency of most ambient vibrations. The goal of this work to micro-fabricate energy harvesters that operate in the same regime as ambient vibrations was achieved.

4.4.2 Harvester testing on ambient sources

The energy harvesters listed in Table 4.3 were tested on several of the ambient sources surveyed in chapter 2. Experimental power output was compared with the model's predicted

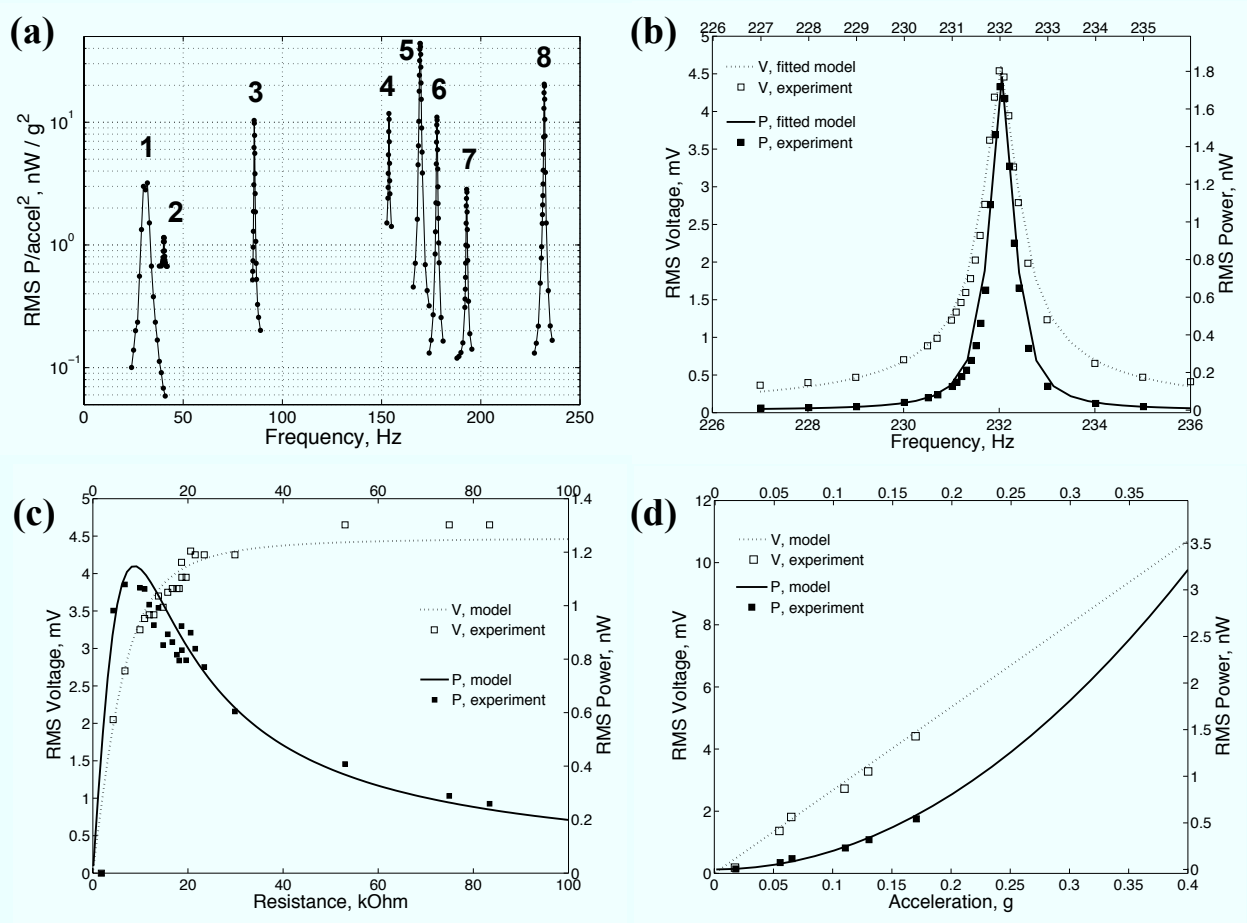

Figure 4.3: Characterization on vibrometer. a) Frequency sweeps, all 8 harvesters, shown on same figure. Normalized power output vs frequency is plotted. b) Frequency sweep, beam 8: a = 0.29 g, R = 12 kΩ. c) Resistance sweep, beam 3, a = 1.55 g, f = 172 Hz. d) Acceleration sweep, beam 6, at f_{n} and R_{opt}.

output when measured ambient acceleration data were used as the model input. Figure 4.5 shows example test results for harvester 8 on the two vibration sources shown in Figure 2.2 (compressor base and fan belt cage in HVAC system). Figures 4.5a and 4.5c show the power spectral density (PSD) as a function of frequency. Figures 4.5b and 4.5d show a close-up of the peak so that modeled and measured signals can be easily compared. Figure 4.6 shows the test results for harvesters 6 and 7 on the compressor base, where plots 4.6a and 4.6c show the full PSD and 4.6b and 4.6d show a close up.

The measured harvester output curve in Figures 4.5 and 4.6 is horizontally flat compared with the modeled output at frequencies away from resonance because the noise floor of the measurement equipment is being reached. Therefore, deviation observed between measured

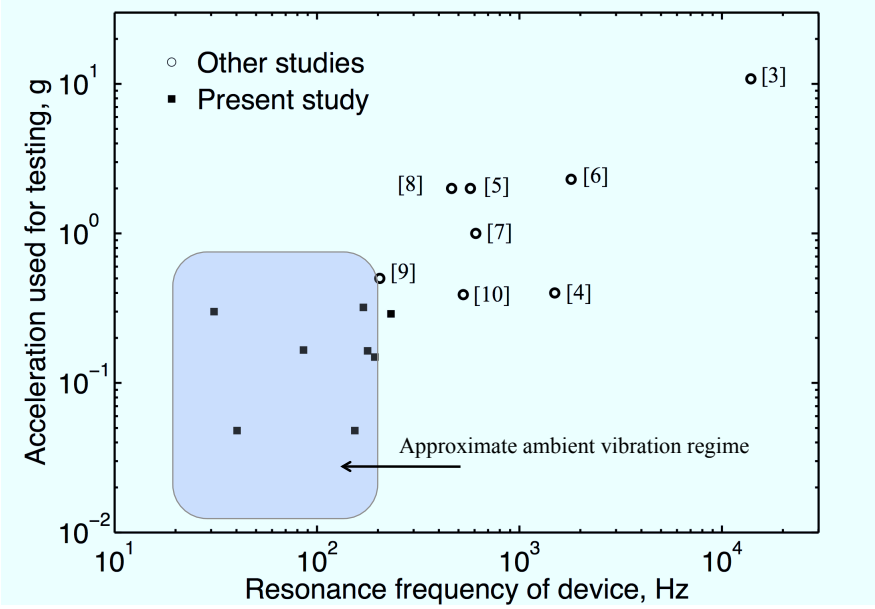

Figure 4.4: Energy harvester f_n plotted versus vibrometer test acceleration for devices presented in this study and other studies. The rectangular shaded area represents the ambient vibration regime. The goal of fabricating energy harvesters that can and will operate in the ambient vibration regime of industrial machinery was achieved.

and modeled beam output signals when the model curve dropped below the experimental noise floor was not a concern since any signal below that power level was undetectable. As seen in these figures, the modeled and measured frequencies and power output agree for these cases.

The power output of the energy harvesters on ambient vibration sources was calculated by integrating the PSD of the measured power output over $f_n \pm 10$ Hz. This is more meaningful than the average power output, as was calculated for the vibrometer tests, because the beam output from ambient sources was not a simple sinusoid. Taking the integral of the signal in the frequency domain allows the noise portion of the beam signal to be ignored, only focusing on the power actually available near the harvester's resonance frequency. The same integration technique was used to find the mean square acceleration, in g^2, for each experiment. Power output from the 8 harvesters tested on ambient vibration sources ranged from 0.63 fW - 202 pW per beam, or 24 pW/g^2 - 10 nW/g^2. The reasons for this range in performance were explained in section 4.4.1.

The model accurately predicts the location of frequency peaks in every case tested. However, the model's ability to predict magnitude of peak power output varies. Figure 4.7 shows a histogram of the ratio between modeled and measured peak power (W/Hz) from the PSD plots in order to quantify the model's ability to predict power output magnitude. There are 38 tests of a harvester on a vibration source represented in the histogram (not all 8

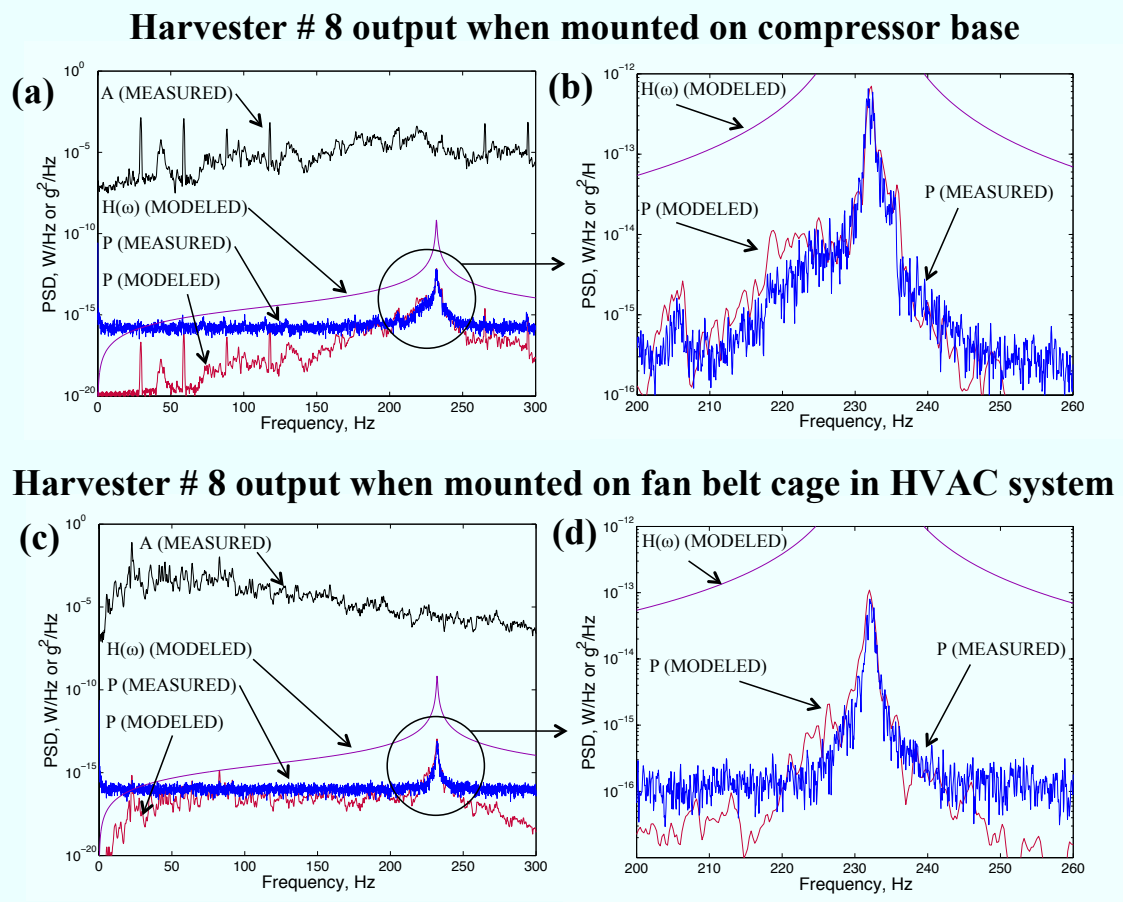

Figure 4.5: Comparison of measured and modeled output from beam 8 on two different ambient vibration sources. Plots show PSD vs frequency, where A is acceleration, H(ω) is transfer function, and P is power output from harvester. a) and c) show full spectrum from 0 - 300 Hz, while b) and d) show a close-up of the peak harvester output.

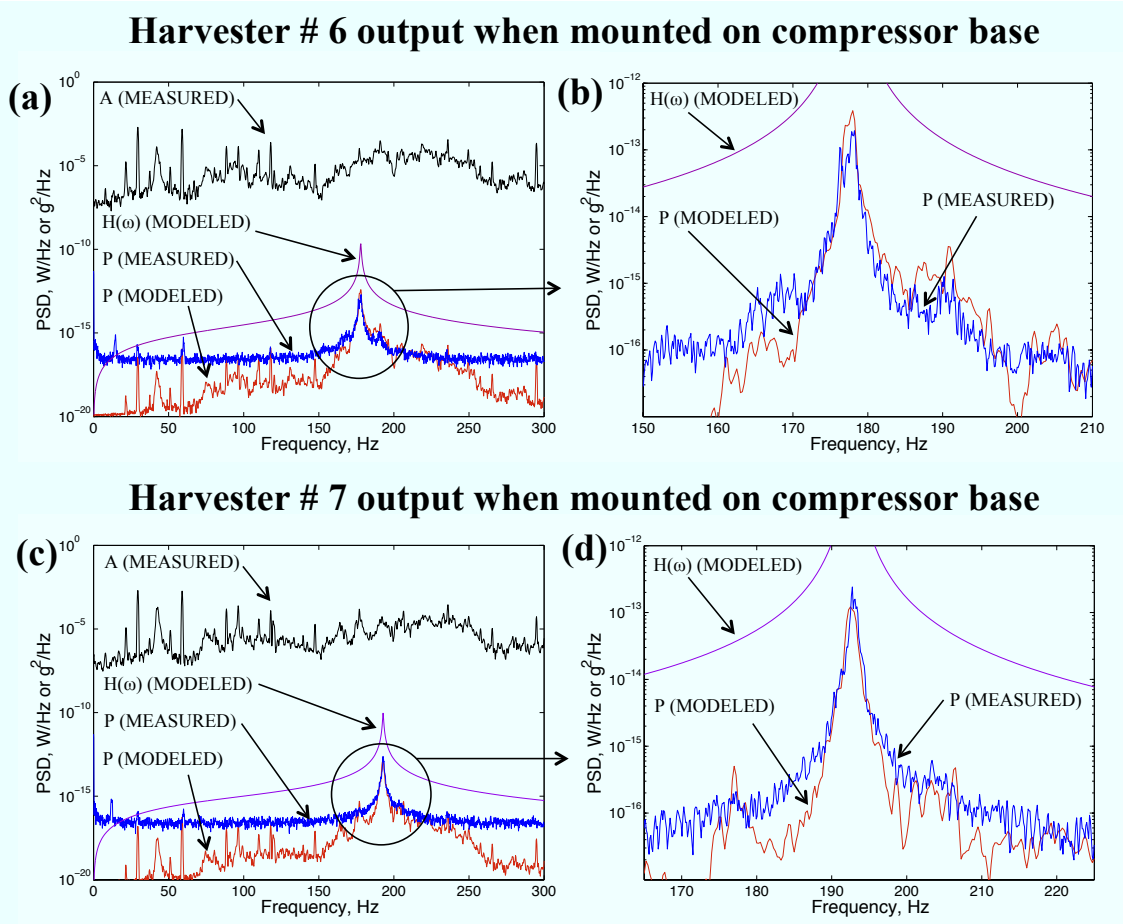

Figure 4.6: Comparison of measured and modeled output from beams 6 and 7 on compressor base. Plots show PSD vs frequency, where A is acceleration, H(ω) is transfer function, and P is power output from harvester. a) and c) show full spectrum from 0 - 300 Hz, while b) and d) show a close-up of the peak harvester output.

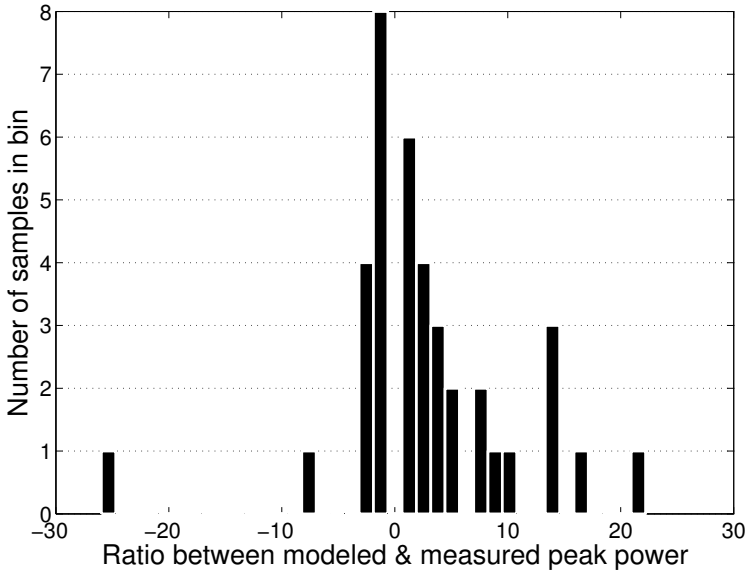

Figure 4.7: Histogram of ratio of modeled to measured peak power output showing how well model and measurement compare. 38 tests are represented. Positive values indicate modeled value is higher, negative indicates measured is higher.

harvesters were tested on all 8 sources). Positive ratios indicate the modeled value is higher, while negative means the measured value is higher.

In an ideal model, the only bar on the histogram would be at $\pm$ 1. The model predicted peak power output within 10x of the experimental value in 82% of tests, and within 5x the experimental value in 68% of the tests. The model is a useful design tool to visualize what the energy harvester frequency response will look like, and estimate the power output within an order of magnitude for an arbitrary ambient vibration source.

4.5 Discussion

One source of inaccuracy in the model is the discrepancy between the measured acceleration and the acceleration experienced by the energy harvester. This issue is two-fold: temporal and spacial. The collection of acceleration input data and harvester output data was not time-synchronized and, although it was collected within the same several-minute interval, the magnitude of frequency peaks can change quickly. The data collection was also not in perfectly spacial-synchronization, since the accelerometer was located several centimeters away from the energy harvester. In future work, both the spacial and temporal aspects will be explored to improve accuracy. Model verification will be achieved by feeding measured ambient acceleration data into a vibrometer and repeating tests to compare with the model.

Another possible cause of discrepancy between the model and experiment is the omission of torsion from the model, while torsion could have occurred due beam geometry. Also, only the z-direction acceleration data was taken into account in this study, yet x- and y-acceleration could have contributed. Future work will incorporate x, y, and z acceleration into the model.

As mentioned in Section 3.1.3, the quality factor was experimentally determined in this study before being entered into the model. When the model is used to investigate the behavior of a new energy harvester design before fabricating it, a value for quality factor will need to be estimated for use in the model, which introduces an uncertainty in the model. In the case that it is critical to achieve a specific quality factor rather than an approximate one, vacuum packaging will be employed to control the damping characteristics and achieve a target quality factor.

The goal in this study was to design micro-fabricated energy harvesters with low resonance frequency, not to optimize power output. Nevertheless, it is worthwhile to consider the power output goal for the energy harvester and ways to achieve it. The customized power conditioning circuitry and ultra low power radio for which the energy harvester needs to supply power require a minimum of 1 μW for low duty cycle functioning. To reach this goal, work is ongoing by researchers in our group to improve the quality of the piezoelectric film. It is realistic to expect an increase in d_{31} to 50–60 pm/V [70], significantly improving power conversion.

Additionally, power output can be increased to more than 1 μW through geometric optimization of harvester dimensions, as will be shown in chapter 6. Also, a larger mass can increase the harvester sensitivity to low magnitude ambient vibrations. Such a mass could be realized without sacrificing packing density by dispenser-printing onto a fully released MEMS cantilever in conjunction with a standard Si proof mass [42].

4.6 Summary

MEMS energy harvesters with resonance frequencies of 31 – 232 Hz were fabricated, characterized, and deployed for testing on ambient vibration sources in the machine room of a large building. The modeled and measured harvester power output on ambient vibration sources were compared. The model accurately predicts frequency peaks in the harvester output spectrum in all tests and predicts power output within an order of magnitude in 82% of the 38 tests conducted. The best energy harvesters produced 1.72 nW_{avg} at 232 Hz and 0.29 g on a vibrometer, and 202 pW at 31 Hz and 0.15 g on an ambient vibration source. The harvesters repeatably produced power output on ambient vibration sources. The focus of this work was to achieve low resonance frequency, and future work will focus on increasing power output.

Chapter 5

Printed Mass

5.1 Motivation for using printed mass

One of the major barriers to the widespread adoption of vibration energy harvesters in practical applications is the mismatch between the resonance frequency of the harvester and its input vibration source. This results in a significant reduction in power output compared to the ideal case of matched frequencies, as illustrated by the energy harvester performance in the previous chapter. The options for resolving this issue can include designing a wideband harvester that is less sensitive to input frequency or designing a self-tuning harvester that can match resonance frequency with the input vibration frequency using a fraction of the generated power. Alternatively, the harvester frequency can be customized to suit the application before it is put into use or tuned after it is installed.

Numerous interesting approaches to this challenge have been proposed. Since the square of resonance frequency is directly proportional to stiffness and indirectly proportional to mass, designs focus on ways to alter mass and stiffness of the harvester. For a thorough overview of frequency modification strategies, see [40] and [32]. For example, several authors have presented energy harvester designs that utilize nonlinear stiffness in the frequency response to achieve wideband devices [40, 65]. Other researchers have proposed using a mechanical stopper [59], an array of harvesters with slightly different resonance frequencies [56], a moveable mass [32], and a magnetically applied axial force to modify the beam stiffness [1]. Other techniques for frequency adjustment include applying axial preload through piezoelectric actuators [13] and mechanical screws [37] to change the beam stiffness.

Each of these frequency modification techniques has advantages and disadvantages, making them suitable for different applications. In applications of MEMS energy harvesting from low amplitude ambient vibrations, nonlinear frequency response is impractical because it requires high acceleration input. Likewise, magnetic forces, and mechanical screws cannot be easily fabricated on the micro-scale. Stoppers and arrays of beams are feasible at the MEMS scale and with low acceleration input, but are undesirable because of decreased

device robustness and inefficient use of wafer area, respectively.

In this chapter, which is adapted from [42], a new method is presented for frequency modification of MEMS cantilevers achieved by direct-write printing to dispense drops of a proof mass ink onto the tips of the beams. Dispenser-printed proof mass deposition makes it possible to customize the energy harvester resonance frequency to match that of the input vibration, as well as that of other harvesting cantilevers such that they can then be connected in series to take advantage of signal addition. The printing technique demonstrated in this study is efficient, fast, easily scalable and non-destructive. This process can be carried out in ambient conditions after completion of all microfabrication steps, including release. This printing technology has been successfully demonstrated in various other areas of research [68].

5.2 Experimental Methods

5.2.1 Preparation of printable proof mass

The printable proof mass was prepared by mixing 85 wt% zinc particles (1-10μm) with an epoxy matrix to achieve a composite slurry. The choice of zinc particles was based on the density and dielectric requirements of the system. The mass ratio can be adjusted to achieve the desired ink density and viscosity. The epoxy used in this study cures over several hours at room temperature, or can be heated in an oven to cure more quickly. The slurry has a refrigerated shelf life of several months.

5.2.2 Frequency sweep of energy harvesters

The MEMS energy harvesters were fabricated, mounted, and testing as described in chapter 4 section 4.2. The energy harvesters were characterized by frequency sweep before and after deposition of printed mass. Each die contained two geometrically identical energy-harvesting beams that were tested alone and as beam pairs in series. The optimal load resistance was experimentally determined. All tests were conducted at this optimal value. Accelerations from 0.03 to 0.17 gs were used in order to mimic approximate range of ambient vibration acceleration amplitudes.

5.2.3 Deposition of printable proof mass

The proof mass ink was deposited on the tips of the energy harvesting cantilevers using a pneumatic direct-write dispenser printer. Energy harvesters with mass deposited are shown in figure 5.1 and the printer system itself is shown in figure 5.2. The position of the dispenser tip was controlled using camera alignment. Deposition was controlled through various printing process parameters including the syringe tip diameter, printing pressure and drop height. Multiple layers of ink can be printed on top of each other, allowing great flexibility, and the

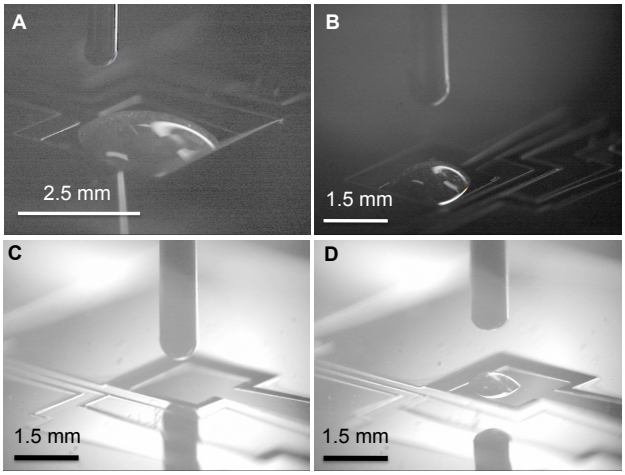

Figure 5.1: Printing proof mass onto the existing square mass of 3 different beams: A) a beam with 3x3 mm^2 mass area, B) a beam with 1.5x1.5 mm^2 mass area, C) & D) before & after printing one drop on a beam with 1.5x1.5 mm^2 mass area

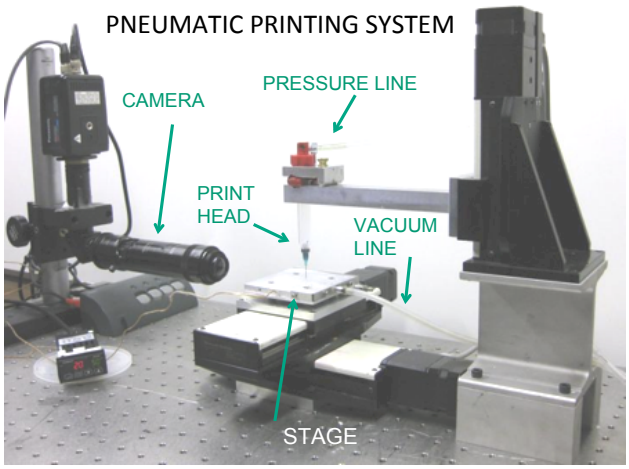

Figure 5.2: Photograph of the pneumatic dispenser printer used to deposit proof mass on the tips of released MEMS cantilever energy harvesters.

process does not damages released MEMS cantilevers. All printing was done in ambient conditions for this study.

5.3 Results

Frequency sweeps revealed that the resonance frequencies of the MEMS energy harvesters ranged from 31 Hz to 232 Hz, which is within the desired range of ambient vibrations

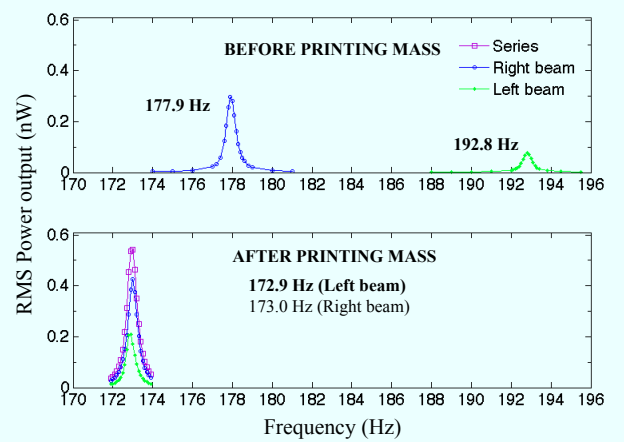

Figure 5.3: Two beams with initially dissimilar resonance frequencies were modified using dispenser-printed proof mass to match within 0.1 Hz.

frequencies as surveyed in chapter 2 and a previous study [51]. The optimal load resistances for 6 beams tested were 1545 kOhm for individual beams and 4485 kOhm for beam pairs in series.

Figure 5.3 shows the frequency response of the left and right energy harvesters on one chip before and after (top and bottom graphs, respectively) deposition of printed proof mass. The harvesters initially had resonance frequencies of 192.8 and 177.9 Hz. After depositing printed proof mass, harvester resonances were 172.9 and 173 Hz, respectively. These results verify that resonance frequency modification of more than 20 Hz with a resolution of 0.1 Hz can be achieved using this printing technique. The frequency shift and resolution results were repeatable with all 6 beams that were tested. Solvent evaporation from the slurry caused a frequency shift of about 0.1 Hz in the first few hours after printing, after which the frequency was stable.

The difference between the magnitudes of the left and right beam output signal is attributed to the presence of localized defects in the piezoelectric sol- gel film, causing slightly different piezoelectric coefficients in each beam. This can be corrected with more careful control of contaminants during sol-gel film deposition.

Figure 5.4 shows a close up of the bottom graph of 5.3 so the relative output signal magnitudes of the left beam, right beam, and beams in series can be seen. In theory, two voltage sources in series add. Similarly, energy harvesters with the same resonance frequency connected in series should have an additive output signal. It can be seen from the graph that the measured signal of the beams connected in series is indeed the sum of the right and left beam signals. This is significant because it means that multiple beams can be used to meet a power output requirement, relaxing the output requirement per beam. The frequency sweep was conducted with an input acceleration of 0.17 g.

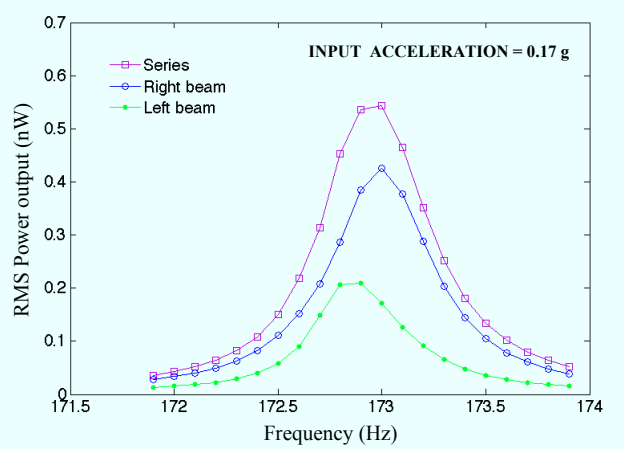

Figure 5.4: Graph illustrating that two beams' voltage outputs add when connected in series if they have the same resonance frequency.

5.4 Discussion

5.4.1 Limiting factors

Minimum resolution: The resolution of 0.1 Hz for frequency modification achieved in this work was limited by the vibrometer controller, which was only able to adjust the vibration frequency by 0.1 Hz increments. The printing process can achieve finer resolution by using slurries with a lower percentage of zinc particles such that each printed droplet has less mass. Of course, a higher-resolution frequency controller would be needed for testing.

Figure 5.5 shows the modeled relationship between the resonance frequency of the two energy harvesters represented in the plots above and the amount of printed mass. This model allows the mass of the printed droplets to be back-calculated based on the measured resonance frequency of the harvester. The mass corresponding to a frequency change of 0.1 Hz is 5 μg.

Maximum frequency modification: Also, the printing process allows for multiple depositions and 3-dimensional structures, so it is not a limiting factor in the frequency reduction attainable. Instead, the limiting factor is the flexural strength of the microfabricated beam, which experiences high stresses when the proof mass becomes very large. Therefore, the 20.6 Hz reduction demonstrated in this study is not the limit of frequency adjustment capability.

Referring again to Figure 5.5, it can be seen that the droplets printed onto the left beam amounted to a mass of 0.67 mg and on the right beam the droplets amounted to a mass of 0.16 mg. The maximum mass of printed droplets deposited in this study was 6.79 mg (data not shown in plots).

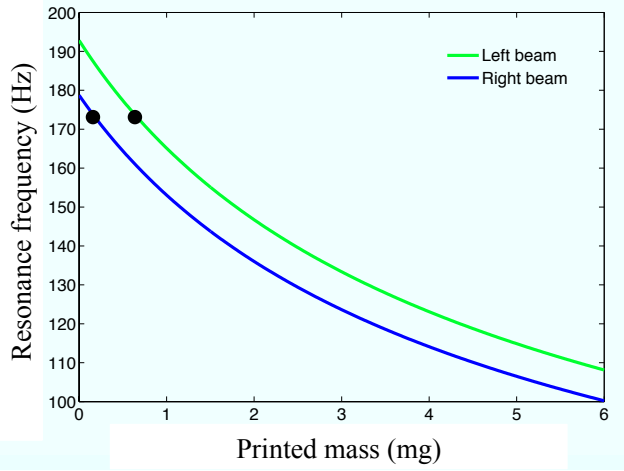

Figure 5.5: The calculated harvester resonance frequency as a function of printed mass is plotted in green and blue for the left and right beams, respectively. The y-intercept of the curves represents the frequency of each harvester before depositing printed mass, and the black dot indicates the experimentally measured frequency after deposition of printed mass. From this, it can be determined that 0.67 mg of mass was printed on the left beam and 0.16 mg was printed on the right beam.

5.4.2 Advantages and disadvantages

An advantage of printing proof masses in addition to those previously mentioned is the ability to increase the packing density by extending mass volume in the thickness direction rather than taking up more area on a silicon wafer. The thickness of the proof mass on an energy harvester is limited by the thickness of the silicon wafer. As a result, an increase in mass can typically only be achieved by increasing area, thereby decreasing packing density. The post-processing method of printing mass onto the tip of the beam takes advantage of the available 3-dimensional space and reduces the required mass area.

The disadvantage of the printing technique in this study is that it requires prior knowledge of the desired resonance frequency and thus the vibration source frequency. Despite this limitation, the ability to make fine-resolution adjustments to the resonance of cantilevers and improve power density with printed masses justifies further exploration.

5.4.3 Printing functional energy storage materials as mass

A potential extension of the printing technique presented here is to deposit energy storage components as the proof mass, such that the harvester charges a printed battery or capacitor, which then provides the appropriate levels of power to the radio and sensor load. This could be achieved by using functional materials as the ink. The use of dispenser printing for constructing micro batteries and micro capacitors has been demonstrated in previous

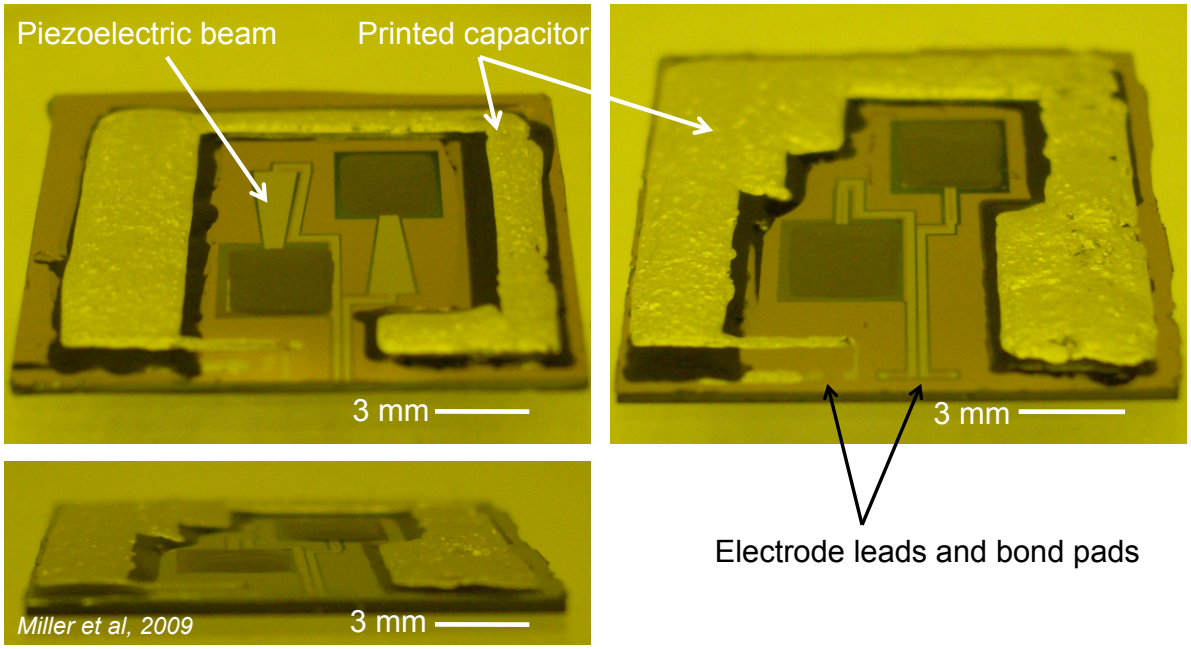

Figure 5.6: Top and side views of electrochemical capacitor printed on energy harvesting device chips. Adapted from [44]. ©2009 IEEE.

works [21, 68], as well as the successful physical integration of a printed capacitor with an energy harvester [44] as shown in figure 5.6. It should be noted that there is no electrical integration between the capacitor and energy harvester in figure 5.6, rather it illustrates how the two systems will be integrated in the future.

5.5 Summary

In this chapter the viability of using direct-write dispenser printing to modify MEMS cantilever resonance frequencies by depositing proof mass ink was demonstrated. Frequency modification of more than 20 Hz with a 0.1 Hz resolution was repeatably achieved. Two beams with initially dissimilar resonance frequencies were modified until their frequencies matched and then connected in series, demonstrating that the voltage and power output signals from the two beams were additive. This verifies that multiple low-output harvesters can be connected in series to generate usable voltage or power, thus relaxing per-beam output requirements.

Chapter 6

Optimization of Fixed-Frequency MEMS Harvester with Resistive Load

6.1 Framing the optimization problem

The device presented in chapter 4 was designed to explore the potential of using MEMS fabrication processes to build cantilevers with resonance frequencies under 200 Hz. This goal was successfully met, and the next task is to optimize the design to maximize power output attainable from such a harvester. There are several questions to be answered in the course of this optimization. First of all, can a MEMS scale harvester produce usable levels of power from ambient vibration levels? If so, what are the optimal dimensions of the device and can a harvester optimized for one frequency produce power at a different frequency? Also, how is the optimization result for single frequency sine wave vibration input different from the result for ambient vibration input? Finally, what do the results tell us about how to design a harvester that can be used on a wide range of ambient vibration sources?

The major constraint imposed on this optimization was that the area of harvester is no more than 1 cm^2. The assumptions used in the optimization were as follows:
1) Only rectangular beams were considered in this optimization.
2) Piezoelectric material was assume to be lead zirconate titanate (PZT) with piezoelectric coefficient of 20 pm/V.
3) Piezoelectric layer was limited to 2 μm or less due to fabrication constraints (it is generally desirable to have a thicker film).
4) Oxide layer thickness was limited to 1 μm or less due to fabrication constraints (this is a structural layer used to improve robustness of the beam and to shift the neutral axis so that the piezoelectric charges do not cancel out). Oxide also serves as an insulating layer but thickness is not critical for this function.
5) The electrodes and piezoelectric material cover the beam area but not the mass area (this impacts the capacitance, which impacts power output).

Table 6.1: Parameters in optimization (unless otherwise noted).

Parameter	**Value**	**Units**	**Comments**
Beam length	1 to 9	mm	optimization variable
Silicon thickness	0 to 50	μm	optimization variable
Beam width	1	cm	set as as wide as possible
Piezoelectric thickness	2	μm	varied manually from 0.5 - 2 μm
Oxide thickness	1	μm	fabrication limits
Mass width	1	cm	set as wide as possible
Mass length	1 - L_b	cm	tradeoff: beam and mass area
Electrode thickness	100	nm	both top & bottom electrodes
Printed mass	4.5	mg	deposited by dispenser printing
Mass height	525	μm	limited by thickness of Si wafer
Electrode elastic modulus	180	GPa	estimate from literature
Piezoelectric elastic modulus	110	GPa	estimate from literature
Oxide elastic modulus	60	GPa	estimate from literature
Silicon elastic modulus	170	GPa	estimate from literature
Quality factor, mode 1	211		measured from previous device
Mass density	2330	kg/m^3	assuming Si mass
Piezoelectric coefficient	20	pm/V	
Dielectric coefficient	11	nF/m	measured on previous device
Dominant frequency, fanbelt	22.5	Hz	
Dominant acceleration, fanbelt	0.203	g's	
Dominant frequency, compressor	29.5	Hz	
Dominant acceleration, compressor	0.043	g's	

6) Power calculations were done assuming a matched resistive load.
7) Power conditioning requirements are not considered in the optimization.

Following from the constraints and assumptions and the fact that it is logical to use the whole available area, the beam length plus mass length should be 1 cm and the beam width should be maximized at 1 cm. The only two variables remaining that make sense to optimize are beam length and silicon layer thickness. Thus the optimization problem is framed in a manageable way. The parameter values used in the optimization model are shown in Table 6.1.

Lastly, the optimization code was verified by checking the results against the experimental results presented in chapter 4. Although the model has compared favorably with experiment there are still sources of uncertainty, including:
1) impact of residual stress is unaccounted for
2) uncertainty in yield stress and elastic modulus values
3) beam theory is used for a beam that has L:W of 1:10 instead of 10:1

4) large deflections are possible, while the model is based on assumptions of small deflections 5) quality factor used in this optimization was constant at 211, based on test with different MEMS piezo harvesters. This value will vary as device geometry varies. The quality factor impacts the magnitude of power output, but does not impact the trend or location of solutions in the "arc" of matching frequencies.

6.2 Optimization results

The optimization was conducted for the two ambient vibration sources that were highlighted in the results of the previous chapters: the fan belt cage and the compressor base. In order to examine the difference between single frequency sine wave and ambient vibration input, the frequency and magnitude of the dominant frequency peak of the ambient source was used as the sine wave case. Additionally, the optimization was carried out for the case in which the input frequency is assumed to match the device resonance frequency. This is not a realistic case but is interesting to see how results differ when the resonance frequency is constrained to match input frequency.

A comparison of the optimized harvester geometry and the original harvester geometry is shown in figure 6.1. The photographs beneath the schematics are from [14] and [43] and are examples of each type of geometry. The general large mass and short wide beam geometric characteristics of the optimal design has been published in the literature, as is evident from [14], but those devices had high resonance frequency of about 500 Hz. The geometry optimized with dimensions such that the resonance frequency is low enough to be compatible with industrial machine vibrations is presented here. It is clear that the large mass is critical to achieving power output and should take up most of the available area. Of course, if the piezoelectric beam had a higher coupling coefficient than the one analyzed in this study, the tradeoff between mass and beam area would change and it is likely that the mass size would decrease to make way for the piezoelectric material. The specific dimensional results of the optimization are given in Table 6.2.

Table 6.2: Optimized beam dimension and power output values

Parameter	**Fan Belt Cage**	**Compressor Base**	**Match Frequency***
Beam length (mm)	0.4	0.2	2.9
Silicon thickness (μm)	3.3	3.0	1.2
Power output** (μW)	33/4.5	1.1/0.25	3.9

*this case uses same amplitude vibration as compressor base case

** single frequency/ambient

The plots of the optimization of beam length and silicon layer thickness versus power output will now be shown so it is clear how the optimized dimensions were found. It should be noted that the spiky, sharp-peaked appearance of the plots of beam length and/or silicon

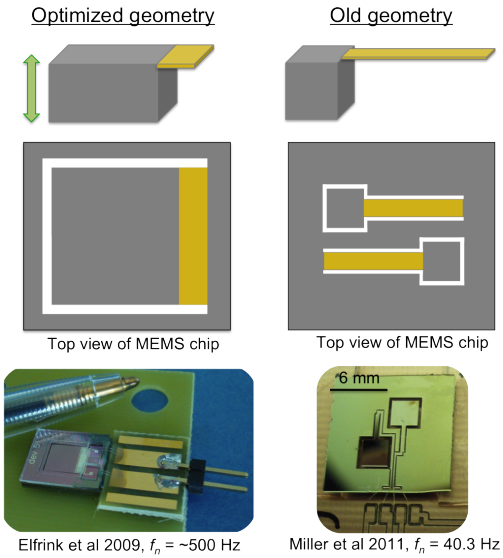

Figure 6.1: This shows the general geometry of the optimized device compared to the old device. The green arrow indicated direction of beam vibration. The yellow areas on the schematics indicated the piezoelectric beam area, while grey indicates silicon support structure or mass. The photographs beneath the schematics are from [14] and [43] and are examples of each type of geometry.

layer thickness versus power output is an artifact of the resolution of the vectors containing beam length or silicon layer thickness values. If the vector resolution is increased by an order of magnitude or two the sharp peaks blend together to form a continuous curve. However, such high resolution demands long computation times. Thus, a tradeoff between computation time and resolution was chosen such that the trends and optimal values can be clearly seen despite the fact that some sharp spiky artifacts remain.

The optimization plots show how sensitive the power output is to a mismatch between the input frequency and the device resonance frequency. If an optimized device were moved to a different vibration source or the operating conditions were to change, altering the frequency, the power output would drop tremendously. Additionally, the resonance frequency of the device is very sensitive to the thickness and length dimensions (as well as mass and other parameters). From a manufacturing perspective, this implies that there is a very narrow tolerance range such that slightly incorrect dimensions cause power output to suffer greatly. These issues raise concerns about the feasibility of using a single-frequency harvester even if the harvester is able to generate plenty of power at one specific frequency.

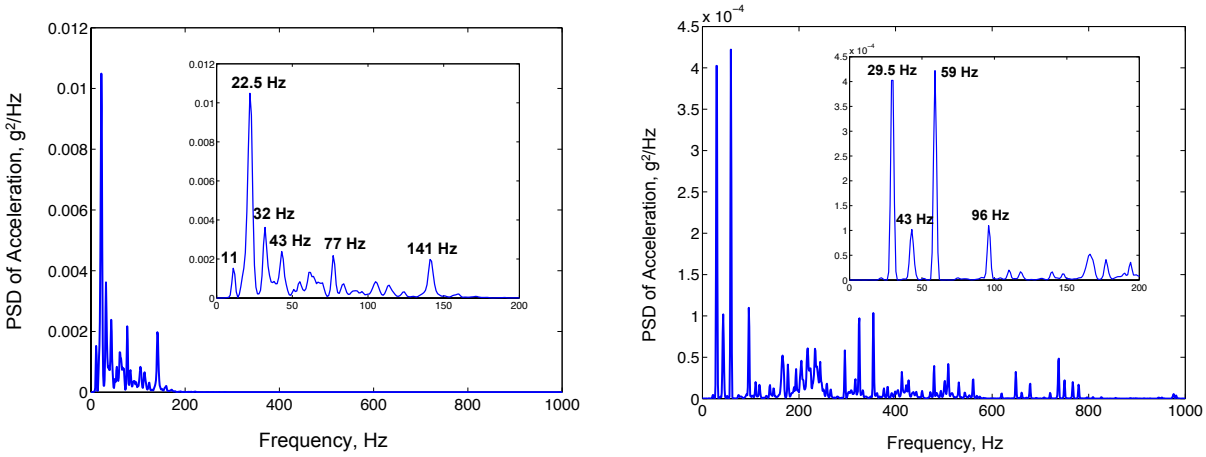

(a) Fan belt cage (b) Compressor base

Figure 6.2: Power spectral density of the vibrations from the fan belt cage (a) and oil compressor (b). The dominant frequency is 22.5 Hz at 0.203 g's for the fan belt cage and 29.5 and 59 Hz at 0.043 g's for the compressor. 22.5 and 29.5 Hz are the frequencies used for the single-frequency sinusoidal comparison case.

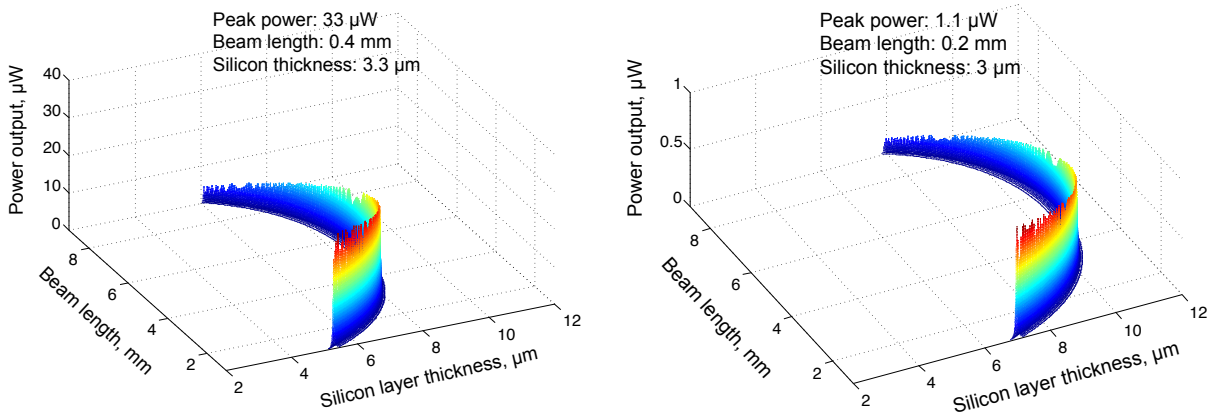

(a) Fan belt cage, dominant single-frequency sine (b) Compressor base, dominant single-frequency sine

Figure 6.3: Power output as a function of beam length and silicon layer thickness. The optimal point cannot be seen in this plot of the full beam lengths.

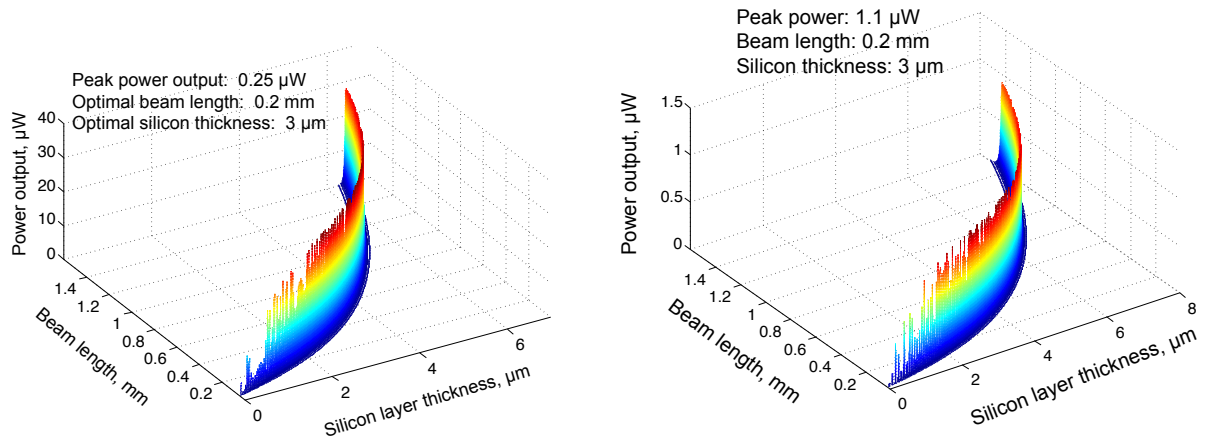

(a) Fan belt cage, dominant single-frequency sine (b) Compressor base, dominant single-frequency sine

Figure 6.4: Close up of power output as a function of beam length and silicon layer thickness, highlighting region where the optimal value occurs.

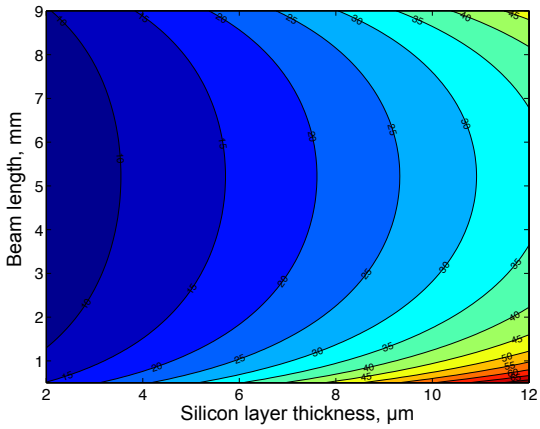

Figure 6.5: This plot illustrated the bands of geometric dimension combinations that result in a specific frequency. This plot explains the reason for the arc shape across the beam length-silicon layer thickness plane.

6.3 Summary

It is now possible to answer the questions that were posed at the beginning of the optimization study. It was found that a MEMS scale harvester can produce several μW of power from ambient vibrations, which is enough to be usable. The optimal dimensions of the device were found and are approximately 0.3 mm beam length and 3 μm silicon layer thickness.

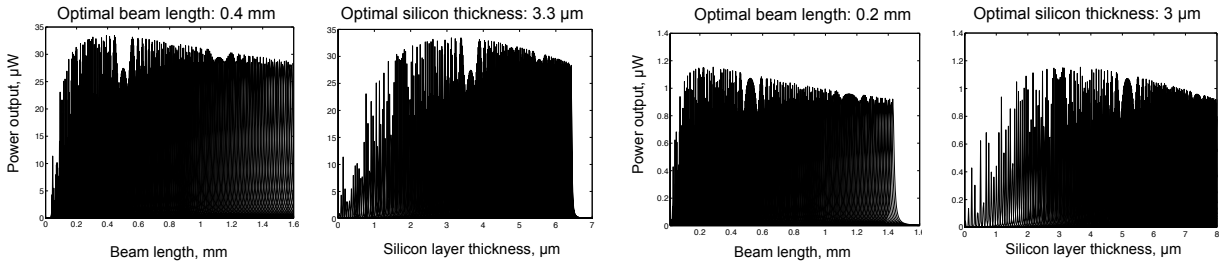

(a) Fan belt cage, dominant single-frequency sine (b) Compressor base, dominant single-frequency sine

Figure 6.6: The values of beam length and silicon layer thickness plotted versus power output reveal the optimal dimensions for fan belt cage of 0.4 mm beam length and 3.3 μm silicon layer thickness, and for compressor base of 0.2 mm and 3.0 μm. This contains the same information as the 3D plot of figure 6.4 but it is easier to see the optimal values in 2D format.

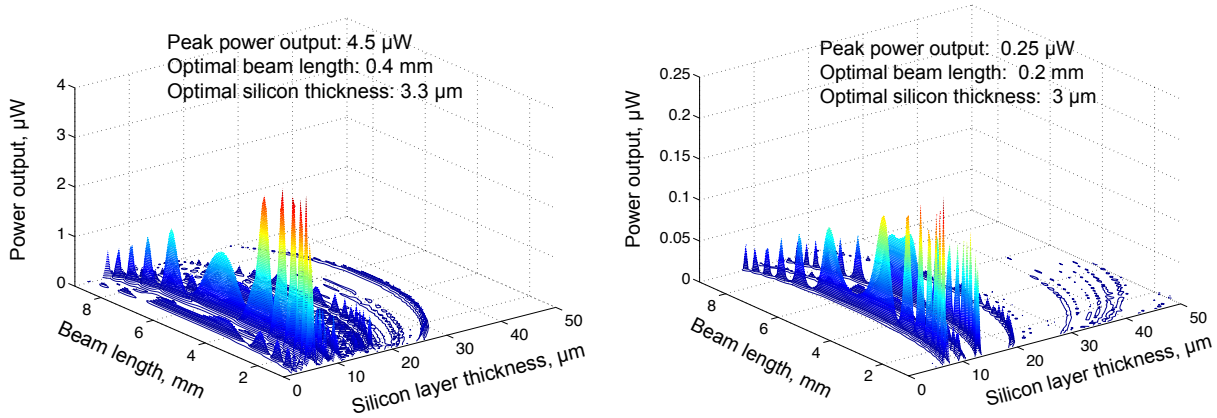

(a) Fan belt cage (b) Compressor base

Figure 6.7: Power output as a function of beam length and silicon layer thickness. The optimal point cannot be clearly seen in this plot of the full beam lengths.

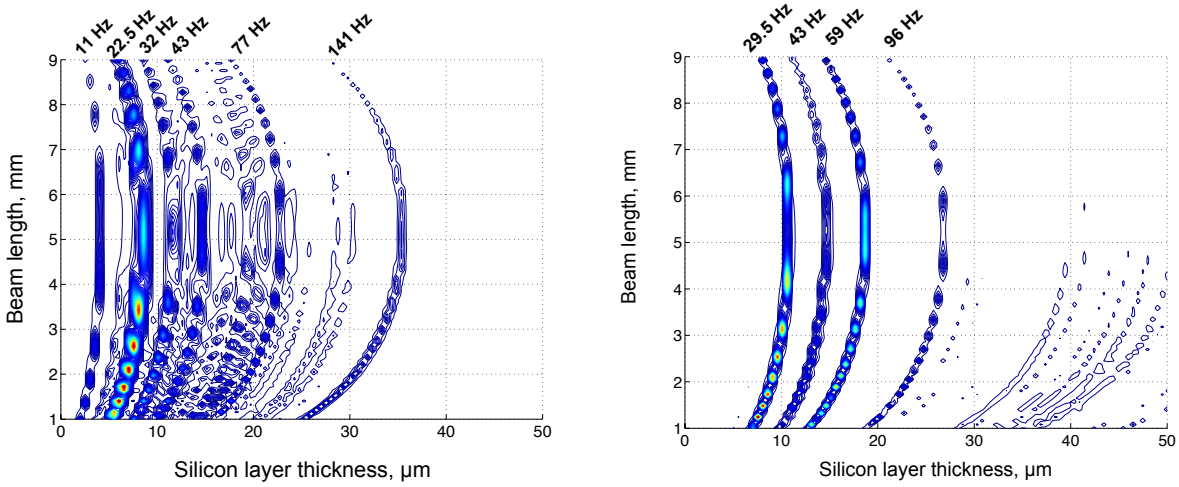

(a) Fan belt cage

(b) Compressor base

Figure 6.8: This plot shows the top view of figures 6.7, revealing the arcs of solutions which correspond to the dominant frequencies in the power spectral density plot of figure 6.2.

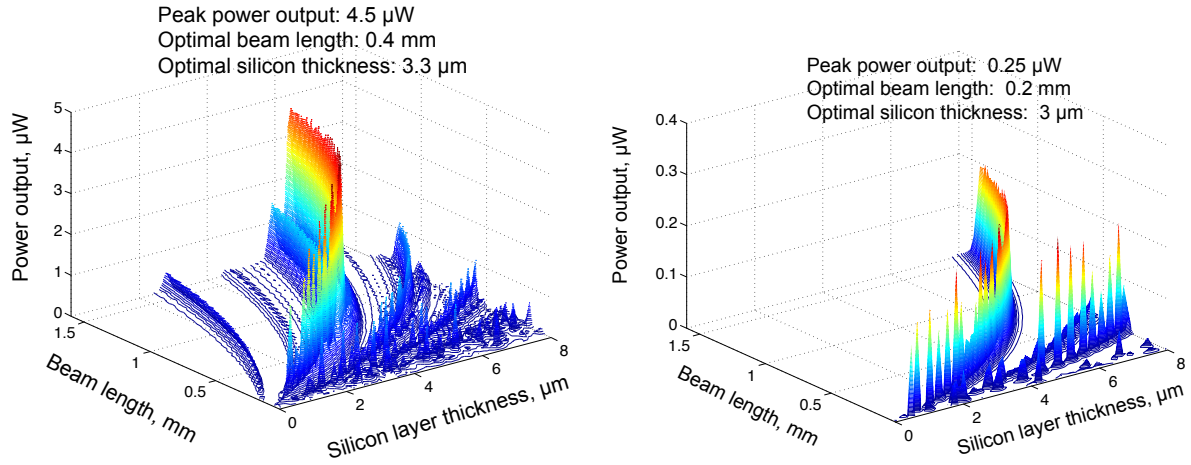

(a) Fan belt cage

(b) Compressor base

Figure 6.9: Close up of power output as a function of beam length and silicon layer thickness, highlighting region where the optimal value occurs.

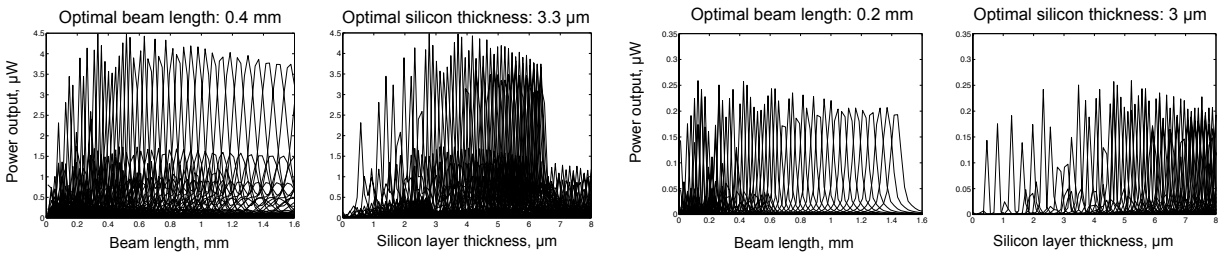

(a) Fan belt cage

(b) Compressor base

Figure 6.10: The values of beam length and silicon layer thickness plotted versus power output reveal the optimal dimensions for fan belt cage of 0.4 mm beam length and 3.3 μm silicon layer thickness, and for compressor base of 0.2 mm and 3.0 μm. This contains the same information as the 3D plot of figure 6.9 but it is easier to see the optimal values in 2D format.

A harvester optimized for a specific frequency cannot produce usable power at a different frequency, and it was determined that the power output from a device optimized with a single frequency sine wave input is about an order of magnitude higher than if the device is optimized for ambient vibration input.

The overarching conclusion from this optimization is that fixed-resonance devices are insufficient for energy harvesting in most real-world conditions. No matter how perfectly a device is optimized and manufactured, it will only work well at it's resonance frequency. In harvesting environments, however, vibration source frequencies change over time and are not usually known *a priori*, before the energy harvester is designed. These findings point to the need to develop a broadband or tunable energy harvester design in order to achieve a device that can function effectively on different vibration sources over a long span of time.

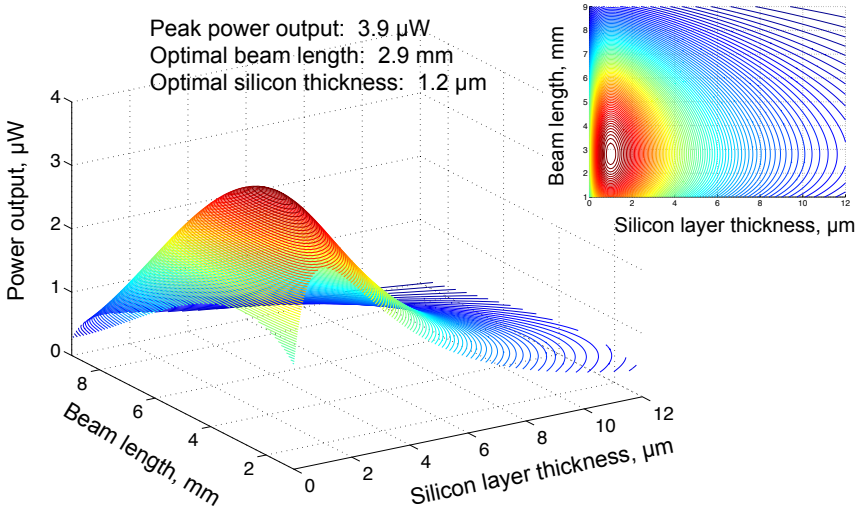

Figure 6.11: Power output as a function of beam length and silicon layer thickness for the case where input frequency is matched to whatever the harvester resonance frequency is. (Input vibration source: single frequency sine wave with frequency matching the harvester's resonance frequency, input acceleration is 0.043 g's.)

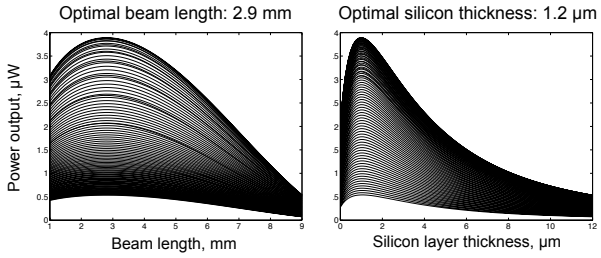

Figure 6.12: The values of beam length and silicon layer thickness plotted versus power output reveal the optimal dimensions of 2.9 mm beam length and 1.2 μm silicon layer thickness. This contains the same information as the 3D plot of figure 6.11 but it is easier to see the optimal values in 2D format. (Input vibration source: single frequency sine wave with frequency matching the harvester's resonance frequency)

Chapter 7

Analytical Framework to Enable Optimization of Fixed-Frequency Harvester with a Synchronous Piezoelectric Pre-bias Circuit

7.1 Optimizing full mechanical and electrical system

In the optimization presented in chapter 6 the only relationship between the piezoelectric harvester and electrical system was the resistive load that was impedance matched to the capacitance of the piezoelectric beam. The mechanical system in this case is essentially unaffected by the electrical system. However, in order to actually use the power out of a harvester it is necessary to convert the alternating current signal into a direct current signal of a voltage level compatible with the battery. Additionally, there are special circuit configurations that can increase the amount of energy extracted from the harvester by using a synchronous pre-bias step where a portion of charge generated is moved from the battery back to the piezoelectric beam. This introduces significant coupling between the mechanical and electrical parts of the system, in contrast to the largely uncoupled case of a resistive electrical load. Optimization then requires having a set of equations to describe the interaction of the mechanical and electrical systems. This chapter presents a system of equations that enables optimization of the full mechanical plus electrical system.

7.2 Insufficiency of resistive and simple rectifying loads

When piezoelectric material is used as the transduction mechanism in an energy harvester it can be advantageous to employ switching interface circuits that increase the electrical damping over what is achievable using a simple passive rectifier interface. Such switching

circuits synchronously modify the charge on the piezoelectric material at the end points of cantilever travel with two common implementations being synchronous switched harvesting on inductor (SSHI) [18], and piezoelectric pre-biasing (PPB) [10]. In this chapter it is shown that, when a piezoelectric transducer is coupled to a circuit which implements the piezoelectric pre-biasing technique, the harvester behaves as a Coulomb-damped resonant generator (CDRG) who's Coulomb damping force can be set by modifying the pre-biasing voltage. This behavior allows such energy harvester systems to be analyzed using a well known analytical framework and highlights the fact that, subject to practical constraints on materials and semiconductor devices, the required electrical damping to achieve maximum power density can be achieved with this technique. The derivation of the pre-bias voltage and Coulomb damping force as a function of the harvester parameters and piezoelectric properties for a harvester connected to a PPB circuit is presented.

7.3 Synchronously switched piezoelectric pre-bias circuit interface

One of the challenges to obtaining successful piezoelectric energy harvesting devices is achieving an electrical damping high enough to obtain the desired levels of power output. This is especially true for MEMS-scale devices as the thin-film piezoelectric materials tend to exhibit lower electromechanical coupling coefficients than bulk piezoelectric materials [7]. Furthermore, MEMS devices tend to have a larger fraction of non-piezoelectric structural material in the cantilever which may further reduce the device electromechanical coupling factor.

Several interface circuit schemes to improve the achievable electrical damping for piezoelectric harvesters have been explored, such as synchronous electric charge extraction (SECE) [34], synchronous switched harvesting on inductor (SSHI) [18], and piezoelectric pre-biasing (PPB) [10]. These circuits, and subsequent iterations of them, have shown that improvements of the order of 10x in power output [18] from the piezoelectric harvesters are possible and this could be further increased if high-Q current paths can be achieved in the interface circuit. The combined electromechanical analysis of piezoelectric harvesters connected to these switching circuits can be highly complex and this in turn makes the combined design a difficult task. Here a simple and intuitive approach to analyzing such systems is provided.

In this chapter we describe how piezoelectric harvesters with a PPB interface can be analyzed in a framework already known to the energy harvesting community, that of the Coulomb-damped resonant generator (CDRG) [46], [41]. We then use this CDRG analysis to present the derivation of the Coulomb damping force in terms of the pre-bias voltage and other system parameters for a piezoelectric harvester connected to a PPB interface circuit. In this paper we consider interface circuits that modify the charge on the piezoelectric capacitor at the endpoints of travel of the cantilever (*e.g.* SSHI, SECE and PPB circuits). We do

not consider switched mode resistive emulation circuits, such as that presented by D'hulst *et al.* [9] as they do not provide the possibility of increasing the electrical damping force over that of a simple passive resistive load. We also assume the generator operates at resonance.

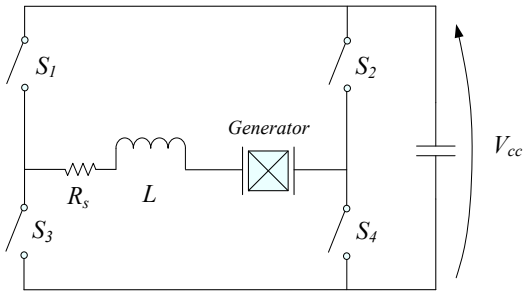

Figure 7.1: Schematic of a simple PPB circuit configuration.

An example of a PPB interface circuit is shown in Figure 7.1 and the operation of that circuit is explained in detail in [10]. In the special case when the pre-bias voltage is zero, the PPB becomes a SECE configuration. Figure 7.2 shows how the voltage, charge and force on the cantilever vary as the tip mass of the cantilever oscillates when the harvester is mechanically excited and connected to a PPB circuit. These diagrams show that switching occurs when the tip mass reaches its maximum and minimum positions, and that charge is exchanged with the external circuit only at these instants.

With these waveforms in mind, we now examine the mechanical behavior of a piezoelectric harvester coupled to a PPB circuit. The piezoelectric constitutive equations are, for our purposes, most conveniently written as

$$F = K_{\mathrm{o}} z + \frac{\Gamma}{C_0} q \tag{7.1}$$

$$V = \frac{\Gamma}{C_0} z + \frac{1}{C_0} q \tag{7.2}$$

where F and V are force and voltage, K_{o} is open circuit stiffness of the beam, z is displacement of the proof mass attached to the end of the beam, Γ is the piezoelectric transduction factor, q is charge on one of the piezoelectric transducer metal electrodes, and C_0 is the clamped capacitance.

The first term in equation (7.1) is the spring force (being proportional to mass tip position) and varies sinusoidally if the cantilever oscillates sinusoidally, while the second term is the force due to the charge present on the electrodes of the piezoelectric transducer due to action of the interface circuit. The value and variation over time of this second term depends on the behavior of the electrical circuit connected to the harvester, as well as the harvester's piezoelectric capacitance. The split between the two contributions to the force in (7.1) allows us to view $\Gamma q/C_0$ as an electrical force and it is clear that if the charge is held

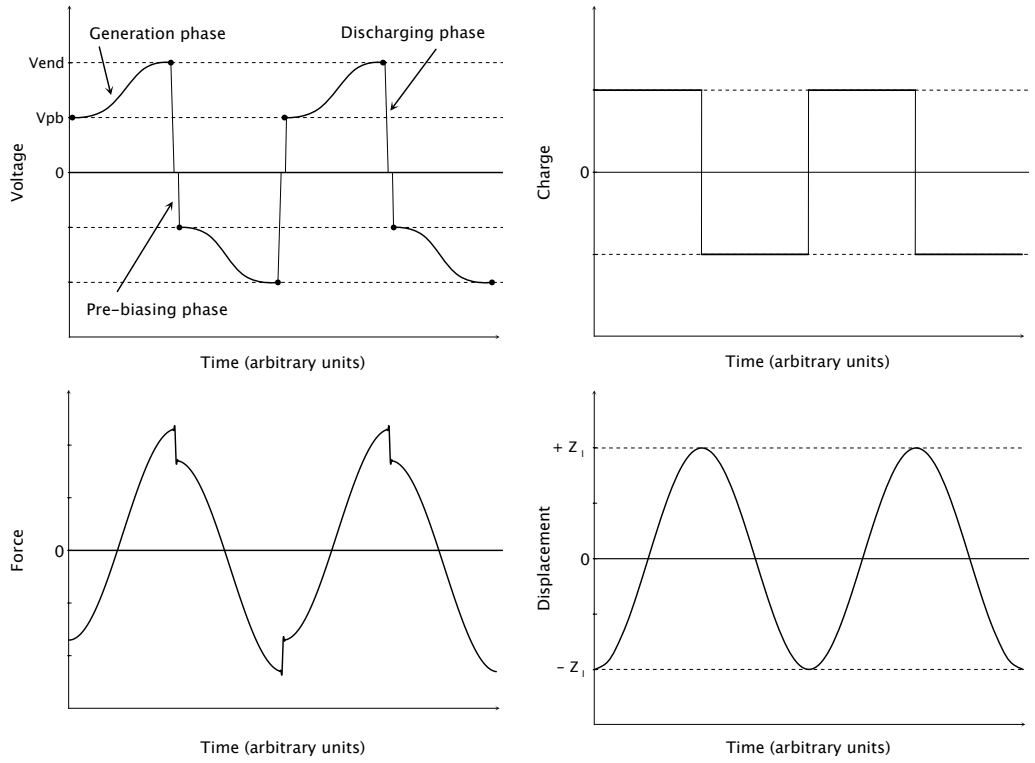

Figure 7.2: Waveforms illustrating the voltage, charge, and force on the piezoelectric harvester when connected with the PPB circuit and the corresponding harvester displacement.

constant for some time interval, then so is this electrical force. Hence, a circuit that remains disconnected from the piezoelectric electrodes on a half-cycle, such that the electrical force opposes the proof mass motion, implements a CDRG.

The sum of the two forces on the piezoelectric cantilever, F, is illustrated in the force diagram of Figure 7.2, where the sinusoidal shape comes from the spring force and the offset that occurs at the peaks comes from the constant force due to charge. As can be seen in Figure 7.2, the PPB technique implements a perfect CDRG as the total force on the piezoelectric cantilever is the sum of a force which is proportional to cantilever position and a constant opposing force (between switching events) equivalent to a Coulomb damper.

Considering the alternative, but equivalent, formulation of the constitutive equation of the form $F = K_{\mathrm{s}} z + \Gamma V$ where $K_{\mathrm{s}} = K_{\mathrm{o}} - \Gamma^2/C_0$ is the short circuit stiffness of the beam, we see that a similar argument can be made for circuits that give a piecewise constant voltage. This is the case for a perfect SSHI implementation, i.e. one with perfect charge inversion, as the piezoelectric voltage is clamped by the conduction of the diode rectifier during the entire half-cycle. However, for a realistic SSHI implementation with imperfect charge inversion, the voltage across the piezoelectric transducer is only clamped by the action of the diode rectifier

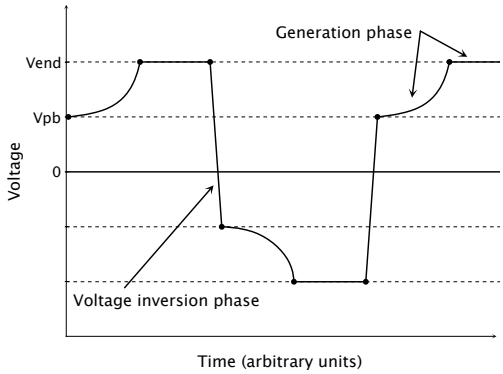

Figure 7.3: Waveform illustrating the piezoelectric voltage with harvester connected to SSHI circuit. This is not a CDRG.

as the cantilever approaches the extremes of its travel, as figure 7.3 illustrates. Therefore, a realistic SSHI implementation is not a perfect CDRG.

We now derive the system equations for a piezoelectric harvester connected to a PPB interface circuit in order to relate the piezoelectric parameters and pre-bias voltage to the Coulomb damping force and system spring constant. An analysis has previously been presented in which the optimal Coulomb damping force has been calculated for a CDRG [46] and, consequently, relating the Coulomb damping force to the piezoelectric properties will allow an optimal pre-bias voltage to be determined to maximize power generation. From [46], the optimal Coulomb damping force on a displacement-constrained CDRG harvester is

$$F_{\mathrm{opt_{CZ}}} = \frac{mY_0\omega^2\omega_c}{|U|}\sqrt{\frac{1}{\left(1-{\omega_c}^2\right)^2} - \frac{1}{{\omega_c}^4}\left(\frac{Z_l}{Y_0}\right)^2} \tag{7.3}$$

$$\text{where} \quad U = \frac{\sin\left(\frac{\pi}{\omega_c}\right)}{1+\cos\left(\frac{\pi}{\omega_c}\right)} \tag{7.4}$$

and m is the proof mass, Y_0 is the input vibration amplitude, ω is the input excitation frequency, ω_c is the ratio of input excitation frequency to device resonance frequency, and Z_l is the maximum possible displacement due to packaging constraints. When $\omega_c = 1$, equation (7.3) simplifies to

$$F_{\mathrm{opt_{CZ}}} = \frac{\pi}{4}m\omega^2 Y_0 = \frac{\pi}{4}mA_{\mathrm{input}}. \tag{7.5}$$

Assuming that the cantilever is at its maximum positive displacement, Z_l, $F_{\mathrm{opt_{CZ}}}$ is equal to the Coulomb damping component of the force on the cantilever (second term in equation (7.1)). Solving this equality for q gives the relation,

$$q = -\frac{\pi}{4}mA_{\mathrm{input}}\frac{C_0}{\Gamma}. \tag{7.6}$$

The sign is negative because the Coulomb damping opposes the relative motion of the cantilever, acting against the spring restoring force. Substituting this expression for q into (7.2) and collecting terms gives the pre-bias voltage, V_{PB}, as

$$V_{\mathrm{PB}} = \left(-\frac{\pi}{4} m A_{\mathrm{input}} + \frac{\Gamma^2 Z_l}{C_0} \right) \frac{1}{\Gamma}, \tag{7.7}$$

which is the pre-bias voltage needed to obtain the optimal Coulomb damping force. When the cantilever is at the negative extreme of its travel, the polarity of the pre-bias voltage is reversed.

It should be noted that, under certain operating conditions, the CDRG can exhibit start-stop motion which is undesirable due to difficulties in control [46]. However this phenomenon does not occur with optimal damping at resonance and so is not considered here.

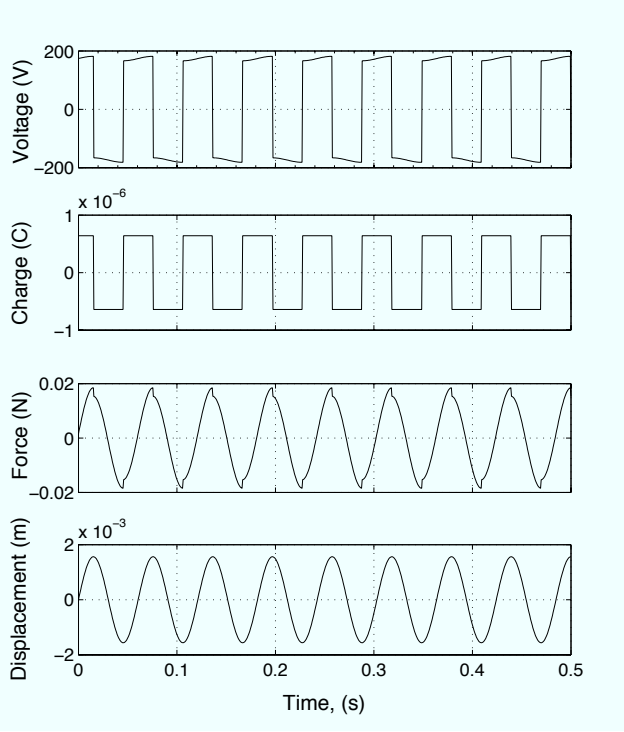

Figure 7.4: Voltage, charge, force, and displacement on piezoelectric cantilever with PPB circuit calculated using CDRG framework.

Figure 7.4 shows results using this CDRG framework with realistic energy harvester parameters for an aluminum nitride MEMS scale harvester. The voltage, charge, and force on the piezoelectric cantilever corresponding with the position of the cantilever proof mass as it oscillates are shown. This illustrates the relative magnitudes of each variable for a realistic system.

7.4 Summary

This chapter has discussed how a piezoelectric energy harvester can be made a perfect CDRG by connecting the mechanical system to a synchronously switched piezoelectric pre-biasing interface circuit. The differences in approximate and perfect CDRG behavior for piezoelectric harvesters with SSHI and piezoelectric pre-biasing circuits, respectively, were explained. Finally, equations were derived within the CDRG framework to find an expression for the pre-bias voltage which maximizes the power generation as a function of the input excitation and piezoelectric energy harvester parameters. These equations give the designer an easy way to calculate optimal pre-bias voltages for a piezoelectric transducer. Although it is not done here, it is possible to use this analytical framework to conduct an optimization of the full mechanical and electrical piezoelectric energy harvester system with a synchronous pre-biasing interface circuit for power conditioning.

Chapter 8

Adaptable-Frequency Nonlinear Resonator: Model

8.1 Switching from lumped model to continuous, nonlinear, coupled model

Until this point, the model presented in chapter 3 has been used to predict and explain the response of the fixed-frequency cantilever energy harvester. However, as discovered in chapter 6, the energy harvester design that resonates only at one specific fixed frequency is not sufficient for successfully harvesting energy from ambient vibration sources. There is clearly a need to develop an energy harvester that works well at an arbitrary frequency by using a broadband or tunable device design.

The broadband type harvester designs found in literature are classified here as active or passive devices. Active methods to achieve frequency matching between the device and the environment entail schemes to control stiffness or mass of the system using an externally supplied force or electronic signal to change the resonance of the energy scavenger. Conversely, passive methods are defined here to mean that no external energy is required to adjust the frequency (i.e. no manual adjustments, no electric input, no control circuits). Broadband type harvesters can be classified in many different ways, but this active versus passive classification scheme was chosen because an ideal device design would not require pre-installation customization of a harvester, nor would it require manual adjustment or maintenance over time. Additionally, active schemes typically rely on a power input to control a logic circuit and/or to actuate or initiate a change in the physical characteristics of the scavenger. The scavenger must then be generating enough power that it can afford to sacrifice a portion of the output to the active tuning, which typically requires higher acceleration input vibrations than what are available in the ambient environment and is therefore not an ideal solution.

For a thorough review of broadband type energy harvester designs available in the literature, see [63], [40], and [69]. Several examples of such harvester designs, along with their

advantages and disadvantages, were given in section 5.1. Several additional device designs include magnetic field induced nonlinearities due to interaction between a stationary magnet and a magnet attached to the harvester beam [60] and frequency up conversion, a technique in which a piezoelectric beam is plucked by a lower-frequency structure and allowed to resonate freely [33, 50]. These magnetically nonlinear and up conversion systems are novel, yet still pose implementation concerns. Achieving broadband response using nonlinear hysteresis requires that the harvester follow the high energy branch of its hysteretic response, which is difficult to ensure. The harvester may, instead, follow the low energy branch of its hysteretic response, which is very similar to that of a standard fixed-frequency harvester rather than broadband. The frequency up conversion configurations can be effective in some applications, but the system still relies on operating at the single resonance frequency of the lower-frequency structure or using impulse as opposed to vibration as the input excitation.

A type of system in the literature which has the potential to avoid many of the aforementioned problems with existing broadband energy harvesters, such as requiring energy input for active tuning, requiring very large input excitation, or requiring impact between components, is that of a beam with a sliding proof mass. In this type of system, the proof mass is constrained to the beam but is free to move along the length of the beam, thereby adding a degree of freedom to the standard beam-mass system. This extra degree of freedom introduces complex nonlinearities to the beam-mass system. One set of papers on this topic presents the sliding proof mass as a technique for passive self-damping of system [2,31,45,64], while another set of papers presents it as a technique for passive self-tuning [5,32]. Interestingly, these two sets of papers never reference each other.

The passive self-damping system literature includes a sliding mass on a cantilever with a restoring spring force attached to the mass to prevent it from sliding off the cantilever [45], a fixed-fixed rubber band with a sliding washer [2], a string with sliding mass subjected to axial (rather than transverse) excitation [64], and a sliding mass on a cantilever with no restoring spring force [31]. The passive self-tuning systems proposed in the literature include a bead on a tensioned fixed-fixed wire which did demonstrate self-tuning [5] and a hollow cylindrical cantilever with a sliding bead inside, which did not show self-tuning behavior [32].

Based on the theoretical and experimental work presented in these papers, it appears that the one of the major factors impacting whether self-damping or self-tuning occurs is how much clearance exists between the beam and the inside diameter of the sliding mass. In all of the papers that found self-damping to occur [2,31,45,64], and the paper that intended to show tuning but showed damping instead [32], the mass had the ability to "bounce" or spin in place on the string or beam, thereby dissipating energy. Boudaoud *et al* reported coupling between bead rotation about its center and string vibration when the bead was threaded directly through its center, so they performed experiments with a bead threaded through an off-center hold to avoid this coupling [5]. The intriguing self-tuning behavior observed by Boudaoud *et al* motivated the development of the beam-mass resonator design which is presented in this chapter.

The lumped model that was used prior to this chapter ignored the dynamics of the

beam vibration, which was reasonable since the resonance frequency of the beam with proof mass was one to two orders of magnitude lower than that of the beam alone (hence the system could be treated quasi-statically). However, in the case of the redesigned system, the dynamics of the beam absolutely must be taken into account because a central feature is that the beam shape influences the mass position along the beam, and vice versa. This means that a continuous, rather than lumped, model must be used. Additionally, rather than having a proof mass whose position is fixed along the beam, the new system design has a proof mass that is allowed to slide along the length of the beam. This adds a good deal of complexity to the behavior of the dynamic system and the model that explains it.

A mathematical model to represent the new energy harvester design will be presented in this chapter. The model presented here builds on research presented in the literature previously by incorporating five particular physical system attributes that have not been combined into the same model by any previous study:

1. This model analyzes a beam rather than a string.
2. This model analyzes a beam with fixed-fixed boundary conditions rather than cantilever boundary conditions.
3. This model accounts for rotary inertia of the mass about the beam rather than treating it as a point mass.
4. This model accounts for the mass's impact on beam shape as well as the beam's impact on mass position rather than assuming that the mass is small enough that it has no impact on beam shape.
5. This model is applicable for multiple eigenmodes of beam excitation rather than only the first mode. This study includes the first two modes, but more could be included if desired.

8.2 Physical system definition

The system, shown in figure 8.1, is defined as follows: input vibrations are described by $W_o(t)$. A point along the beam is denoted by the coordinate X, beam vertical position is described by $W(X,t)$, mass horizontal position is $Y(t)$, and mass vertical position is $W(Y(t),t)$. Derivatives with respect to time are denoted with a dot and derivatives with respect to X are denoted with a prime. Derivatives with respect to $Y(t)$ are written out explicitly. The coordinate system is defined as the x-axis along the length of beam and the z-axis in the direction of vertical displacement. The beam properties are defined by its bending stiffness, EI, linear density, ρA, and length, L. Slope and angular rotation of the

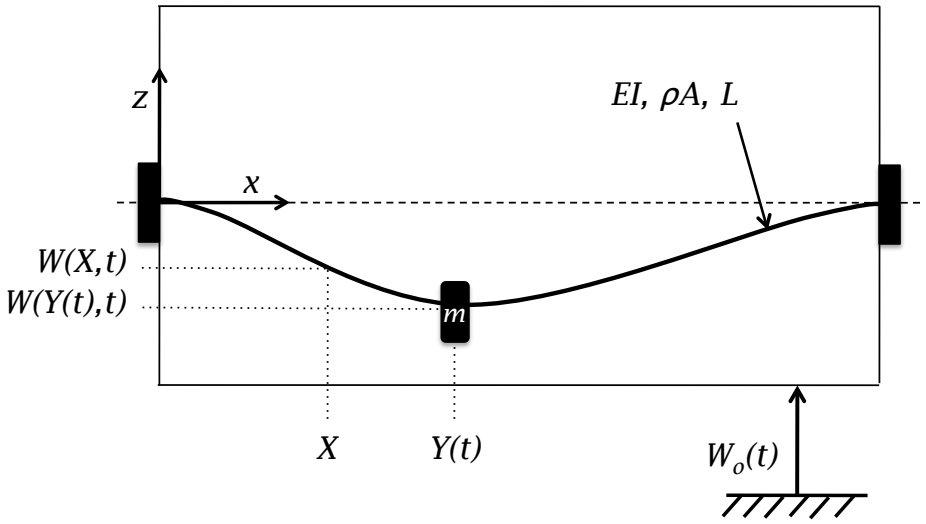

Figure 8.1: Schematic of the spring-mass system. The fixed-fixed beam is secured to a reference frame which is subjected to input vibrations. The mass is free to slide along the beam and has a moment of inertia.

beam due to the mass are given, respectively, by

$$\theta = \left.\frac{\partial W}{\partial X}\right|_{X=Y(t)} = W'(Y(t),t) \tag{8.1}$$

$$\dot{\theta} = \frac{d}{dt}\left(\left.\frac{\partial W}{\partial X}\right|_{X=Y(t)}\right) = (W''\dot{Y} + \dot{W}')|_{X=Y(t)} \tag{8.2}$$

Similarly, the velocity of the mass due to constrained motion with the beam is found by taking the time derivative of the mass position, resulting in

$$\frac{d}{dt}\big(W_o(t) + W(Y(t),t)\big) = \dot{W}_o + \dot{W} + W'\dot{Y}. \tag{8.3}$$

8.3 Equations of motion

The kinetic energy of the beam and the sliding mass is

$$\begin{aligned} T &= \int_0^L \frac{1}{2}\rho A(\dot{W}_o + \dot{W})^2 dX \\ &\quad + \frac{1}{2}m\big[\dot{Y}^2 + (\dot{W}_o + \dot{W} + W'\dot{Y})^2\big]_{X=Y(t)} + \frac{1}{2}I_m\big[(W''\dot{Y} + \dot{W}')^2\big]_{X=Y(t)} \end{aligned} \tag{8.4}$$

where ρ is density of the beam, A is cross sectional area of the beam, L is length of the beam, m is the proof mass, and I_m is moment of inertia of the mass about the y-axis. The first

term represents kinetic energy of the beam due to vertical motion, second term is kinetic energy of the mass due to horizontal motion along the beam and kinetic energy of the mass due to vertical motion with the beam, and the last term is kinetic energy of the mass due to rotation about the beam. Potential energy of the system is simply due to elastic deformation of the beam and is given by

$$V = \int_0^L \frac{1}{2} EI(W'')^2 dX \tag{8.5}$$

where E is the young's modulus of the beam and I is moment of inertia of the beam about the y-axis. The Lagrangian density $\mathcal{L}$ of the system, kinetic minus potential energy density, is

$$\begin{aligned} \mathcal{L} &= \frac{1}{2}\rho A(\dot{W}_o + \dot{W})^2 - \frac{1}{2}EI(W'')^2 \\ &\quad + \left\{ \frac{1}{2}m\dot{Y}^2 + \frac{1}{2}m(\dot{W}_o + \dot{W} + W'\dot{Y})^2 + \frac{1}{2}I_m(W''\dot{Y} + \dot{W}')^2 \right\} \delta(X - Y). \end{aligned} \tag{8.6}$$

Taking the variation of the action integral and using Hamilton's Principle results in the Euler-Lagrange equations for the beam and mass, respectively, as

$$-\frac{d}{dt}\frac{\partial \mathcal{L}}{\partial \dot{W}} - \frac{d}{dX}\frac{\partial \mathcal{L}}{\partial W'} + \frac{d^2}{dtdX}\frac{\partial \mathcal{L}}{\partial \dot{W}'} + \frac{d^2}{dX^2}\frac{\partial \mathcal{L}}{\partial W''} = 0 \tag{8.7}$$

$$\frac{\partial \mathcal{L}}{\partial Y} - \frac{d}{dt}\frac{\partial \mathcal{L}}{\partial \dot{Y}} = 0. \tag{8.8}$$

Computing the necessary derivatives and partial derivatives of (8.6) according to equations (8.7) and (8.8) results in the beam and mass equations of motion, respectively, as

$$\begin{aligned} 0 &= \rho A(\ddot{W}_o + \ddot{W}) + m(\ddot{W}_o + \ddot{W} + 2\dot{W}'\dot{Y} + W''\dot{Y}^2 + W'\ddot{Y})\delta(X - Y) + EIW'''' \\ &\quad - \frac{d}{dX}\left[I_m(\ddot{W}' + 2\dot{W}''\dot{Y} + W'''\dot{Y}^2 + W''\ddot{Y})\delta(X - Y) \right] \end{aligned} \tag{8.9}$$

$$\begin{aligned} 0 &= m\ddot{Y} + m(\ddot{W}_o + \ddot{W} + 2\dot{W}'\dot{Y} + W''\dot{Y}^2 + W'\ddot{Y})W' \\ &\quad + I_m(\ddot{W}' + 2\dot{W}''\dot{Y} + W'''\dot{Y}^2 + W''\ddot{Y})W''. \end{aligned} \tag{8.10}$$

The equations of motion are nondimensionalized by introducing the following nondimensional time, frequency, and displacements for the system, closely following the notation used by Miranda *et al* [45]:

$$\tau = \tilde{\omega}_1 t, \quad \Omega = \frac{\omega}{\tilde{\omega}_1}, \quad w_o = \frac{W_o}{L}, \quad w = \frac{W}{L}, \quad x = \frac{X}{L}, \quad y = \frac{Y}{L}, \tag{8.11}$$

where τ is nondimensional time, $\tilde{\omega}_1$ is the fundamental frequency of the beam with no mass present, Ω is nondimensional frequency, and for displacements the lowercase letters represent

nondimensional versions of the uppercase letters. The derivatives are nondimensionalized according to the same parameters. Substituting the nondimensional terms into equations (8.9) and (8.10), dividing the mass equation by $mL\tilde{\omega}_1^2$ and the beam equation by $\rho AL\tilde{\omega}_1^2$, and then adding terms for damping and friction results in the nondimensional equations of motion,

$$\begin{aligned} 0 &= \ddot{y} + c_m\dot{y} + (\ddot{w}_o + \ddot{w} + 2\dot{w}'\dot{y} + w''\dot{y}^2 + w'\ddot{y})w' \\ &\quad +\chi(\ddot{w}' + 2\dot{w}''\dot{y} + w'''\dot{y}^2 + w''\ddot{y})w'' \\ &\quad +\mu\Big[(\ddot{w}_o + \ddot{w} + 2\dot{w}'\dot{y} + w''\dot{y}^2 + w'\ddot{y} + \bar{g})\text{sgn }(\dot{y} + w'(\dot{w}_o + \dot{w} + w'\dot{y}))\Big] \qquad (8.12) \\ 0 &= (\ddot{w}_o + \ddot{w}) + c_b(\dot{w}_o + \dot{w}) + \alpha(\ddot{w}_o + \ddot{w} + 2\dot{w}'\dot{y} + w''\dot{y}^2 + w'\ddot{y})\delta(x-y) \\ &\quad +\nu w'''' - \gamma\frac{d}{dx}\Big[(\ddot{w}' + 2\dot{w}''\dot{y} + w'''\dot{y}^2 + w''\ddot{y})\delta(x-y)\Big] \qquad (8.13) \end{aligned}$$

with dimensionless parameters defined as

$$\alpha = \frac{m}{\rho AL}, \quad \nu = \frac{EI}{\rho AL^4\tilde{\omega}_1^2}, \quad \gamma = \frac{I_m}{\rho AL^2}, \quad \chi = \frac{I_m}{mL^2} \qquad (8.14)$$

$$c_m = \frac{C_m}{m\tilde{\omega}_1}, \quad c_b = \frac{C_b}{\rho AL\tilde{\omega}_1}, \quad \bar{g} = \frac{g}{L\tilde{\omega}_1^2}, \qquad (8.15)$$

where α is a nondimensional mass, ν is nondimensional stiffness, γ and χ are nondimensional rotational moment of inertia of the proof mass relative to the beam inertia and the mass inertia respectively, c_m and c_b are linear viscous damping of the mass motion and beam motion respectively, $\bar{g}$ is nondimensional gravity, and μ is dry friction of mass sliding.

8.4 Eigenfunctions and boundary conditions

To obtain the expression for the beam shape as a function of time, we start with the homogenous case of equation (8.13), where $w_o = 0$. Neglecting damping but including rotational inertia of the mass, as well as assuming that mass is considered fixed because it moves on a much slower timescale than the beam, we have

$$0 = \ddot{w} + \alpha\ddot{w}\delta(x-y) + \nu w'''' - \gamma\ddot{w}'(y,\tau)\delta'(x-y) \qquad (8.16)$$

which can also be written, with a different representation of the last term, as

$$0 = \ddot{w} + \alpha\ddot{w}\delta(x-y) + \nu w'''' - \gamma\frac{d}{dx}\Big[\delta(x-y)\ddot{w}'(x,\tau)\Big]. \qquad (8.17)$$

Using separation of variables,

$$w(x,\tau) = u(x)T(\tau). \qquad (8.18)$$

If we substitute this into equation (8.17), rearrange, divide through by ν, and substitute $\ddot{T}(\tau)/T(\tau) = -\Omega^2$, we arrive at

$$u''''(x) - \frac{1+\alpha\delta(x-y)}{\nu}u(x)\Omega^2 + \frac{\gamma}{\nu}\frac{d}{dx}\Big[\delta(x-y)u'(x)\Big]\Omega^2 = 0. \tag{8.19}$$

Rearranging equation (8.19) to give

$$u''''(x) = \frac{\Omega^2}{\nu}\left\{[1+\alpha\delta(x-y)]u(x) - \gamma\frac{d}{dx}\big[\delta(x-y)u'(x)\big]\right\} \tag{8.20}$$

where two linear operators are defined:

$$\hat{K} = \frac{d^4}{dx^4}, \quad \hat{M} = 1 + \alpha\delta(x-y) - \gamma\frac{d}{dx}\delta(x-y)\frac{d}{dx}. \tag{8.21}$$

Note that the operations in the last term of M should be done in order from right to left. Substituting into equation (8.20) gives

$$\hat{K}u_n(x) = \beta_n^4\hat{M}u_n(x), \quad \text{where} \quad \beta_n^4 = \frac{\Omega_n^2}{\nu}. \tag{8.22}$$

The solution to equation (8.22) is of the form

$$\begin{aligned} u_{L,n}(x) &= A_{L,n}\cos\beta_n x + B_{L,n}\sin\beta_n x + C_{L,n}\cosh\beta_n x + D_{L,n}\sinh\beta_n x, \quad x < y \\ u_{R,n}(x) &= A_{R,n}\cos\beta_n(1-x) + B_{R,n}\sin\beta_n(1-x) \\ &\quad + C_{R,n}\cosh\beta_n(1-x) + D_{R,n}\sinh\beta_n(1-x), \quad x > y. \end{aligned} \tag{8.23}$$

The eight unknown coefficients in these equations must be found using eight boundary conditions. The first four boundary conditions are given by the fact that the beam has fixed-fixed end conditions, so the deflection and slope at both ends of the beam, $x = 0$ and $x = 1$, must be zero. This is written as

$$u(0) = u(1) = 0, \quad u'(0) = u'(1) = 0. \tag{8.24}$$

Additionally, there are four boundary conditions that come from continuity requirements. Those are found by the following procedure, recalling that θ is the Heaviside function, where $\theta(x-y) = 0$ if $x < y$ but $\theta(x-y) = 1$ if $x > y$. Also, the derivative of the Heaviside function is the Dirac delta.

$$u_n(x) = \theta(x-y)u_{R,n}(x) + \theta(y-x)u_{L,n}(x) \tag{8.25}$$

$$u_n'(x) = \delta(x-y)\big[u_{R,n}(y) - u_{L,n}(y)\big] + \theta(x-y)u_{R,n}'(x) + \theta(y-x)u_{L,n}'(x) \tag{8.26}$$

Equation (8.19) has no δ''' terms, so the δ term must drop out of equation (8.26). To ensure this, the expression in brackets must equal zero, giving the fifth boundary condition. Taking the second and third derivatives of $u_n(x)$ leads to

$$u_n''(x) = \delta(x-y)\big[u_{R,n}'(y) - u_{L,n}'(y)\big] + \theta(x-y)u_{R,n}''(x) + \theta(y-x)u_{L,n}''(x) \quad (8.27)$$

$$u_n'''(x) = \delta(x-y)\big[u_{R,n}''(y) - u_{L,n}''(y)\big] + \theta(x-y)u_{R,n}'''(x) + \theta(y-x)u_{L,n}'''(x) \quad (8.28)$$

where the terms inside the brackets in equation (8.27) also must equal zero since there are no δ'' terms in equation (8.19), thus giving a sixth boundary condition. However, the term inside the brackets in equation (8.28) must not equal zero since there is a δ' in the equation (8.19). Therefore, the fourth derivative of $u_n(x)$ is

$$\begin{aligned} u_n''''(x) = \quad & \delta(x-y)\big[u_{R,n}'''(y) - u_{L,n}'''(y)\big] && (8.29)\\ + \quad & \delta'(x-y)\big[u_{R,n}''(y) - u_{L,n}''(y)\big] \\ + \quad & \theta(x-y)u_{R,n}''''(x) + \theta(y-x)u_{L,n}''''(x). && (8.30) \end{aligned}$$

The final two boundary conditions are found by equating the coefficients of the various derivatives of δ. Recalling the original beam equation, (8.19), and multiplying (8.30) by ν gives

$$\begin{aligned} \nu u''''(x) = \quad & \nu\delta(x-y)\big[u_{R,n}'''(y) - u_{L,n}'''(y)\big] \\ + \quad & \nu\delta'(x-y)\big[u_{R,n}''(y) - u_{L,n}''(y)\big] \\ + \quad & \nu\theta(x-y)u_{R,n}''''(x) + \nu\theta(y-x)u_{L,n}''''(x) && (8.31)\\ \nu u''''(x) = \quad & \Omega^2(1+\alpha\delta(x-y))u_n(x) - \Omega^2\gamma\delta'(x-y)u_n'(y) && (8.32) \end{aligned}$$

from which boundary conditions 7 and 8 are found to be, respectively,

$$\nu\big[u_{R,n}''(y) - u_{L,n}''(y)\big] = -\Omega^2\gamma u_n'(y) \quad (8.33)$$

$$\nu\big[u_{R,n}'''(y) - u_{L,n}'''(y)\big] = \Omega^2\alpha u_n(x) \quad (8.34)$$

To summarize, the eight boundary conditions are

$$\begin{aligned} &1) \quad u(0) = 0 \\ &2) \quad u(1) = 0 \\ &3) \quad u'(0) = 0 \\ &4) \quad u'(1) = 0 \\ &5) \quad u_{R,n}(y) - u_{L,n}(y) = 0 \\ &6) \quad u_{R,n}'(y) - u_{L,n}'(y) = 0 \\ &7) \quad u_{R,n}''(y) - u_{L,n}''(y) = -\frac{\Omega_n^2\gamma}{\nu}u_n'(y) \\ &8) \quad u_{R,n}'''(y) - u_{L,n}'''(y) = \frac{\Omega_n^2\alpha}{\nu}u_n(y). \end{aligned} \quad (8.35)$$

Applying boundary conditions 1-4 to equation (8.19) shows that $A_{L,n} = -C_{L,n}$, $B_{L,n} = -D_{L,n}$, $A_{R,n} = -C_{R,n}$ and $B_{R,n} = -D_{R,n}$, leaving

$$\begin{aligned} u_{L,n}(x) &= A_{L,n}(\cos\beta_n x - \cosh\beta_n x) + D_{L,n}(\sin\beta_n x - \sinh\beta_n x) && (8.36) \\ u_{R,n}(x) &= A_{R,n}(\cos\beta_n(1-x) - \cosh\beta_n(1-x)) \\ &+ D_{R,n}(\sin\beta_n(1-x) - \sinh\beta_n(1-x)) && (8.37) \end{aligned}$$

The first, second, and third derivatives of $u_n(x)$ can now be computed and substituted into boundary conditions 5-8. This yields four expressions with five unknowns for each mode (β_n, $A_{L,n}$, $D_{L,n}$, $A_{R,n}$, and $D_{R,n}$). This system is solved numerically in MATLAB by assuming one mass position at a time, assuming a vector of input "guesses" for the value of β_n, and then solving the system of four equations and four unknowns for each value of β_n guess. The condition number of the matrix of coefficients ($A_{L,n}$, $D_{L,n}$, $A_{R,n}$, and $D_{R,n}$ for each boundary condition) is then plotted as a function of β_n. The values of β_n that result in the condition number spiking to a very large value (meaning that the coefficient matrix is singular) indicate nontrivial solutions. These β_n solutions are then inserted into the four equations and four unknowns to find the values for $A_{L,n}$, $D_{L,n}$, $A_{R,n}$, and $D_{R,n}$ for the desired number of modes. Two modes were calculated in this study, and singular value decomposition method was used to solve the system.

With all coefficients now known, the beam shape can be calculated for the mass fixed in a given position. Before using the beam shape expressions in computation they need to be normalized. Details regarding the normalization procedure can be found in Appendix C. Going forward, w_n refers to the full beam shape solution including segments of the beam both left and right, $u_{L,n}$ and $u_{R,n}$, of the position of the proof mass. Finally, the fundamental frequency of the beam with no mass present, $\tilde{\omega}_1$, is needed in order to nondimensionalize the system of equations according to the parameters defined in equations (8.11), (8.14), and (8.15). To find this frequency, the characteristic equation of a fixed-fixed beam with no mass,

$$\cos\lambda_n \cosh\lambda_n = 1, \tag{8.38}$$

is solved numerically for the eigenvalues, λ_n, from which frequency can be calculated using $\tilde{\omega}_1^2 = EI\lambda_1^4/\rho AL^4$.

8.5 Fixed-mass eigenmode expansion

We now solve the equations of motion that were derived in the previous sections using eigenmode expansion. If $w_n(x, y, \tau)$ is the solution of (8.17) corresponding to the natural frequency ω_n, we write

$$w(x, \tau) = \sum_{n=0}^{\infty} \eta_n(\tau) w_n(x, y, \tau) \tag{8.39}$$

and insert into equations (8.12) and (8.13), multiply from the left by $w_m(x,y)$ and integrate over x. In these w_n terms, $y = y(\tau)$, but will be written at simply y for ease. Similarly, all integrals are evaluated from 0 to 1 (the nondimensional length of the beam). Also, note that w, w_n, w_m, and ω_n are all distinct variables. Performing these operations for the beam equation and expanding for $n = 0, 1$ and $m = 0, 1$ yields a set of equations which can be expressed in matrix form as

$$\begin{bmatrix} A_0 & B_0 \\ A_1 & B_1 \end{bmatrix} \begin{bmatrix} \ddot{\eta}_0 \\ \ddot{\eta}_1 \end{bmatrix} + \begin{bmatrix} C_0 & D_0 \\ C_1 & D_1 \end{bmatrix} \begin{bmatrix} \dot{\eta}_0 \\ \dot{\eta}_1 \end{bmatrix} + \begin{bmatrix} E_0 & F_0 \\ E_1 & F_1 \end{bmatrix} \begin{bmatrix} \eta_0 \\ \eta_1 \end{bmatrix} = \begin{bmatrix} Q_0 \\ Q_1 \end{bmatrix} \tag{8.40}$$

where, for $m = 0$,

$$\begin{aligned}
Q_0 &= -\ddot{w}_o \int_0^1 w_0(x,y)dx - \alpha \ddot{w}_o w_0(y,y) - c_b \dot{w}_o \int_0^1 w_0(x,y)dx \qquad (8.41)\\
A_0 &= 1 \\
B_0 &= 0 \\
C_0 &= c_b + 2\dot{y}\Bigg(\alpha w_0(y,y) w_0'(y,y) - \gamma w_0(y,y) w_0'''(y,y) + \gamma w_0'(y,y) w_0'''(y,y) \\
&\quad + \alpha w_0(y,y) \frac{\partial w_0(y,y)}{\partial y} - \gamma w_0(y,y) \frac{\partial w_0''(y,y)}{\partial y} + \gamma w_0'(y,y) \frac{\partial w_0''(y,y)}{\partial y} \\
&\quad + \int_0^1 w_0(x,y) \frac{\partial w_0(x,y)}{\partial y} dx \Bigg) \\
D_0 &= 2\dot{y}\Bigg(\alpha w_0(y,y) w_1'(y,y) - \gamma w_0(y,y) w_1'''(y,y) + \gamma w_0'(y,y) w_1'''(y,y) \\
&\quad + \alpha w_0(y,y) \frac{\partial w_1(y,y)}{\partial y} - \gamma w_0(y,y) \frac{\partial w_1''(y,y)}{\partial y} + \gamma w_0'(y,y) \frac{\partial w_1''(y,y)}{\partial y} \\
&\quad + \int_0^1 w_0(x,y) \frac{\partial w_1(x,y)}{\partial y} dx \Bigg)
\end{aligned}$$

$$
\begin{aligned}
E_0 &= \nu\beta_0^4 + \ddot{y}\alpha w_0(y,y)\frac{\partial w_0(y,y)}{\partial y} + \dot{y}^2 2\alpha w_0(y,y)\frac{\partial w_0'(y,y)}{\partial y} - \ddot{y}\gamma w_0(y,y)\frac{\partial w_0''(y,y)}{\partial y} \\
&+\ddot{y}\gamma w_0'(y,y)\frac{\partial w_0''(y,y)}{\partial y} - \dot{y}^2 2\gamma w_0(y,y)\frac{\partial w_0'''(y,y)}{\partial y} + \dot{y}^2 2\gamma w_0'(y,y)\frac{\partial w_0'''(y,y)}{\partial y} \\
&+\ddot{y}\int_0^1 w_0(x,y)\frac{\partial w_0(x,y)}{\partial y}dx + c_b\dot{y}\int_0^1 w_0(x,y)\frac{\partial w_0(x,y)}{\partial y}dx \\
&+\dot{y}^2\Bigg(\alpha w_0(y,y)\frac{\partial^2 w_0(y,y)}{\partial y^2} - \gamma w_0(y,y)\frac{\partial^2 w_0''(y,y)}{\partial y^2} + \gamma w_0'(y,y)\frac{\partial^2 w_0''(y,y)}{\partial y^2} \\
&+\int_0^1 w_0(x,y)\frac{\partial^2 w_0(x,y)}{\partial y^2}dx\Bigg) \\
&+\dot{y}^2\Big(\alpha w_0(y,y)w_0''(y,y) - \gamma w_0(y,y)w_0''''(y,y) + \gamma w_0'(y,y)w_0''''(y,y)\Big) \\
&+\ddot{y}\Big(\alpha w_0(y,y)w_0'(y,y) - \gamma w_0(y,y)w_0'''(y,y) + \gamma w_0'(y,y)w_0'''(y,y)\Big) \\
F_0 &= \ddot{y}\alpha w_0(y,y)\frac{\partial w_1(y,y)}{\partial y} + \dot{y}^2 2\alpha w_0(y,y)\frac{\partial w_1'(y,y)}{\partial y} - \ddot{y}\gamma w_0(y,y)\frac{\partial w_1''(y,y)}{\partial y} \\
&+\ddot{y}\gamma w_0'(y,y)\frac{\partial w_1''(y,y)}{\partial y} - \dot{y}^2 2\gamma w_0(y,y)\frac{\partial w_1'''(y,y)}{\partial y} + \dot{y}^2 2\gamma w_0'(y,y)\frac{\partial w_1'''(y,y)}{\partial y} \\
&+\ddot{y}\int_0^1 w_0(x,y)\frac{\partial w_1(x,y)}{\partial y}dx + c_b\dot{y}\int_0^1 w_0(x,y)\frac{\partial w_1(x,y)}{\partial y}dx \\
&+\dot{y}^2\Bigg(\alpha w_0(y,y)\frac{\partial^2 w_1(y,y)}{\partial y^2} - \gamma w_0(y,y)\frac{\partial^2 w_1''(y,y)}{\partial y^2} + \gamma w_0'(y,y)\frac{\partial^2 w_1''(y,y)}{\partial y^2} \\
&+\int_0^1 w_0(x,y)\frac{\partial^2 w_1(x,y)}{\partial y^2}dx\Bigg) \\
&+\dot{y}^2\Big(\alpha w_0(y,y)w_1''(y,y) - \gamma w_0(y,y)w_1''''(y,y) + \gamma w_0'(y,y)w_1''''(y,y)\Big) \\
&+\ddot{y}\Big(\alpha w_0(y,y)w_1'(y,y) - \gamma w_0(y,y)w_1'''(y,y) + \gamma w_0'(y,y)w_1'''(y,y)\Big)
\end{aligned}
$$

The terms for $m = 1$ follow the same form as for $m = 0$ and are not stated explicitly here. The mass equation expressed in matrix form after performing eigenmode expansion operations and expanding for $n = 0, 1$ (the mass equation is independent of m) is

$$G\ddot{y} + H\dot{y} + (HH)\dot{y}^2 = K - J, \tag{8.42}$$

where

$$
\begin{aligned}
G &= 1+\left[\eta_0\frac{\partial w_0(y,y)}{\partial y}+\eta_1\frac{\partial w_1(y,y)}{\partial y}\right]\left[\eta_0 w_0'(y,y)+\eta_1 w_1'(y,y)\right] \\
&\quad +\chi\left[\eta_0\frac{\partial w_0'(y,y)}{\partial y}+\eta_1\frac{\partial w_1'(y,y)}{\partial y}\right]\left[\eta_0 w_0''(y,y)+\eta_1 w_1''(y,y)\right] \\
&\quad +\mu\left[\eta_0\frac{\partial w_0(y,y)}{\partial y}+\eta_1\frac{\partial w_1(y,y)}{\partial y}\right]\mathrm{sgn}\big(\,*\,\big) \\
&\quad +\left[\eta_1 w_0'(y,y)+\eta_1 w_1'(y,y)\right]^2+\chi\left[\eta_0 w_0''(y,y)+\eta_1 w_1''(y,y)\right]^2 \\
&\quad +\mu\left[\eta_0 w_0'(y,y)+\eta_1 w_1'(y,y)\right]\mathrm{sgn}\big(\,*\,\big) \\
H &= c_m+2\left[\dot\eta_0\frac{\partial w_0(y,y)}{\partial y}+\dot\eta_1\frac{\partial w_1(y,y)}{\partial y}\right]\left[\eta_0 w_0'(y,y)+\eta_1 w_1'(y,y)\right] \\
&\quad +2\chi\left[\dot\eta_0\frac{\partial w_0'(y,y)}{\partial y}+\dot\eta_1\frac{\partial w_1'(y,y)}{\partial y}\right]\left[\eta_0 w_0''(y,y)+\eta_1 w_1''(y,y)\right] \\
&\quad +2\mu\left[\dot\eta_0\frac{\partial w_0(y,y)}{\partial y}+\dot\eta_1\frac{\partial w_1(y,y)}{\partial y}\right]\mathrm{sgn}\big(\,*\,\big) \\
&\quad +2\left[\dot\eta_0 w_0'(y,y)+\dot\eta_1 w_1'(y,y)\right]\left[\eta_0 w_0'(y,y)+\eta_1 w_1'(y,y)\right] \\
&\quad +2\chi\left[\dot\eta_0 w_0''(y,y)+\dot\eta_1 w_1''(y,y)\right]\left[\eta_0 w_0''(y,y)+\eta_1 w_1''(y,y)\right] \\
&\quad +2\mu\left[\dot\eta_0 w_0'(y,y)+\dot\eta_1 w_1'(y,y)\right]\mathrm{sgn}\big(\,*\,\big)
\end{aligned}
\tag{8.43}
$$

$$
\begin{aligned}
HH &= \left[\eta_0\frac{\partial^2 w_0(y,y)}{\partial y^2}+\eta_1\frac{\partial^2 w_1(y,y)}{\partial y^2}\right]\left[\eta_0 w_0'(y,y)+\eta_1 w_1'(y,y)\right] \\
&\quad +\chi\left[\eta_0\frac{\partial^2 w_0'(y,y)}{\partial y^2}+\eta_1\frac{\partial^2 w_1'(y,y)}{\partial y^2}\right]\left[\eta_0 w_0''(y,y)+\eta_1 w_1''(y,y)\right] \\
&\quad +\mu\left[\eta_0\frac{\partial^2 w_0(y,y)}{\partial y^2}+\eta_1\frac{\partial^2 w_1(y,y)}{\partial y^2}\right]\mathrm{sgn}(*) \\
&\quad +2\left[\eta_0\frac{\partial w_0'(y,y)}{\partial y}+\eta_1\frac{\partial w_1'(y,y)}{\partial y}\right]\left[\eta_0 w_0'(y,y)+\eta_1 w_1'(y,y)\right] \\
&\quad +\left[\eta_0 w_0''(y,y)+\eta_1 w_1''(y,y)\right]\left[\eta_0 w_1'(y,y)+\eta_1 w_1'(y,y)\right] \\
&\quad +2\chi\left[\eta_0\frac{\partial w_0''(y,y)}{\partial y}+\eta_1\frac{\partial w_1''(y,y)}{\partial y}\right]\left[\eta_0 w_0''(y,y)+\eta_1 w_1''(y,y)\right] \\
&\quad +\chi\left[\eta_0 w_0'''(y,y)+\eta_1 w_1'''(y,y)\right]\left[\eta_0 w_0''(y,y)+\eta_1 w_1''(y,y)\right] \\
&\quad +2\mu\left[\eta_0\frac{\partial w_0'(y,y)}{\partial y}+\eta_1\frac{\partial w_1'(y,y)}{\partial y}\right]\mathrm{sgn}(*)+\mu\left[\eta_0 w_0''(y,y)+\eta_1 w_1''(y,y)\right]\mathrm{sgn}(*) \\
J &= \left[\ddot{\eta}_0 w_0(y,y)+\ddot{\eta}_1 w_1(y,y)\right]\left[\eta_0 w_0'(y,y)+\eta_1 w_1'(y,y)\right] \\
&\quad +\chi\left[\ddot{\eta}_0 w_0'(y,y)+\ddot{\eta}_1 w_1'(y,y)\right]\left[\eta_0 w_0''(y,y)+\eta_1 w_1''(y,y)\right] \\
&\quad +\mu\left[\ddot{\eta}_0 w_0(y,y)+\ddot{\eta}_1 w_1(y,y)\right]\mathrm{sgn}(*) \\
K &= \ddot{w}_o\left[\eta_0 w_0'(y,y)+\eta_1 w_1'(y,y)\right]+\mu(\ddot{w}_o+\bar{g})\mathrm{sgn}(*)
\end{aligned}
\tag{8.44}
$$

where

$$
\begin{aligned}
* &= \dot{y}+\left(\dot{w}_o+\left[\dot{\eta}_0 w_0(y,y)+\dot{\eta}_1 w_1(y,y)\right]+\dot{y}\left[\eta_0\frac{\partial w_0(y,y)}{\partial y}+\eta_1\frac{\partial w_1(y,y)}{\partial y}\right]\right. \\
&\quad \left.+\dot{y}\left[\eta_0 w_0'(y,y)+\eta_1 w_1'(y,y)\right]\right)\left[\eta_0 w_0'(y,y)+\eta_1 w_1'(y,y)\right]
\end{aligned}
\tag{8.45}
$$

These expressions can be solved numerically. Many of the terms used in the above equations depend on mass position, y, including $A_{L,n}$, $D_{L,n}$, $A_{R,n}$, $D_{R,n}$, β_n, ω_n, and the normalization coefficient. Using a computer program, the value of each of those terms for each discrete mass position along the length of the beam was calculated and a curve fit was done for each term's dependence on y. Then, partial derivatives of the beam deflection, w_n, with respect to y were computed using the curve fits before evaluating those partial derivatives at $x = y$ to get the value needed for the above equations. Similarly, integrals were evaluated numerically

only after the partial derivatives of beam deflection with respect to y were determined. Integration is along the full length of the beam, so the integrals were split into two terms for the left side (evaluated from 0 to y) and the right side (evaluated from y to 1) of the beam.

8.6 Summary

In this chapter a derivation was carried out to find the coupled nonlinear equations of motion for a spring mass system consisting of a fixed-fixed beam with a sliding proof mass. At this point it is possible to solve these equations using a computer program. The next chapter will contain the numerical and experimental results. For a more detailed account of how this derivation was done and how the equations were solved, see Appendix C.

Chapter 9

Adaptable-Frequency Nonlinear Resonator: Design, Fabrication, & Results

A prototype device was built in order to gain intuition about the fixed-fixed beam with sliding proof mass system, whose complex nonlinear nature makes its behavior difficult to predict, and to achieve a proof-of-concept of an adaptable-frequency, or "self-tuning", system. This chapter describes the design, fabrication, and experimental results of the adaptable-frequency prototype device, and compares these results to the numerical results from the model presented in chapter 8.

9.1 Prototype device design

The prototype adaptable-frequency device was designed to be meso scale rather than micro scale for ease of fabrication, experimentation, configuration of the sliding proof mass, and observation of system behavior. Other design requirements were that the device have a resonance frequency below 100 Hz, to fit within the frequency range of ambient vibrations, and that it be fabricated in a way that ensures validity of using fixed-fixed boundary conditions for the beam. Additionally, the sliding proof mass needed to be designed in a way that the mass, moment of inertia of the mass, and clearance with the beam could be adjusted, or that the mass could be removed entirely if necessary.

Aluminum was chosen as the beam structural material because it is low cost and easy to machine. Beam dimensions were chosen as 30 cm long, 4.8 mm wide, and 1.1 mm thick in order to achieve a beam first-mode resonance frequency of 87 Hz. No piezoelectric materials were incorporated into this prototype because the goal of this prototype was to understand the complex nonlinear interactions between the beam and mass. In future prototypes, a piezoelectric layer should be added to the beam in the region near the fixed walls. Adding

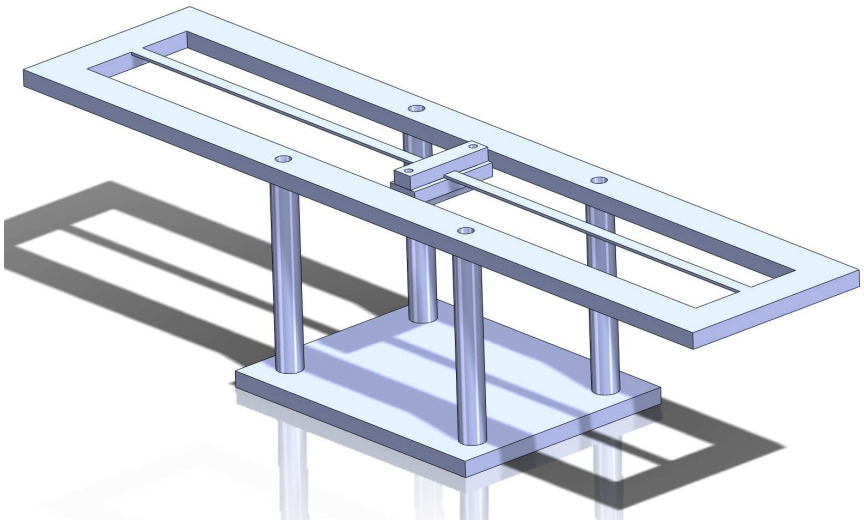

Figure 9.1: Computer aided design graphic of the prototype adaptable-frequency beam-mass assembly and support structure. The assembly is mounted to the vibrometer with the base platform.

piezoelectric material only near the base is not expected to dramatically impact the beam shapes or behavior compared to the case with no piezoelectric material.

Tungsten was chosen as the mass material because of its high density. The mass dimensions were chosen as 2.51 cm long, 4.8 mm wide, and 3.22 mm thick, which were small enough to be compatible with beam geometry yet massive enough to have an impact on beam shape. In order to adjust the mass, multiple pieces of tungsten mass could be stacked together. In order to adjust the moment of inertia of the mass, the rectangular tungsten pieces could be mounted in different orientations relative to beam length.

A sliding mass holder was required to couple the mass to the beam. The mass holder needed to be removable, have adjustable clearance with the beam, introduce as little torsional rotation to the beam as possible, and have as little sliding friction as possible. A two piece clamp design was chosen and was affixed around the beam using small screws, as shown in figure 9.1. Clearance was adjusted by adding layers of thin tape between the top and bottom mass holder pieces. Tungsten mass pieces were mounted to the bottom of the mass holder using double sided tape. The torsion introduced by the mass holder was minimized by keeping the dimensions in the beam's width direction as small as possible, using plastic rather than metal to reduce mass of mass holder, and using small screws rather than large to reduce the mass that was outside the width of the beam. The sliding friction was minimized by designing the contact surface of the mass holder to be a narrow line of contact rather than a large rectangular contact surface. In future designs, ball bearings could potentially be incorporated.

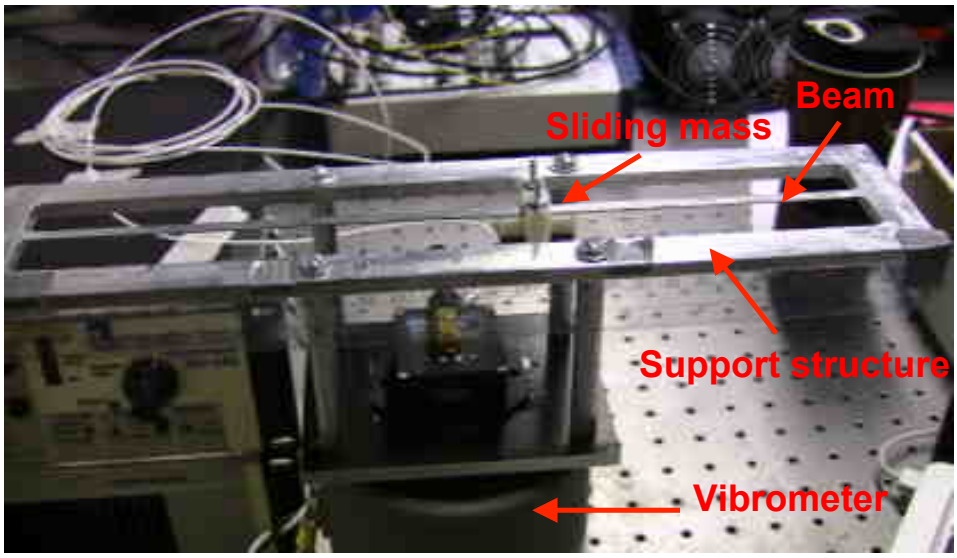

Figure 9.2: Prototype adaptable-frequency beam with sliding mass assembled and mounted to the vibrometer.

9.2 Prototype device fabrication

The beam was machined from a solid piece of aluminum to assure fixed-fixed boundary conditions, and conventional machining processes were used. The outside structure supporting the beam was nearly an order of magnitude thicker than the beam and more than twice as wide so that the support structure's resonance frequency would be much higher than the beam, thereby avoiding unwanted interaction between the dynamics of the support structure and the beam. The beam surface was sanded and polished to remove machining grooves and burrs to achieve low friction between the beam and sliding mass. Tri-glide lubricant was also applied to the beam surface. The tungsten mass rectangular pieces were cut using wire electrical discharge machining and the plastic mass holder was fabricated using a 3D rapid prototype printer. The completed beam-mass assembly was mounted to a vibrometer as shown in figure 9.2.

9.3 Methods

9.3.1 Experimental

The adaptable-frequency prototype was tested on a Labworks ET-126 vibrometer with a Labworks pa-138 power amplifier. The vibrometer acceleration was controlled through Labview using a Kistler 8315A single axis accelerometer to close the feedback loop, and frequency was set at a constant value in Labview. If a different frequency was desired it was changed

manually. Strain at the base of the beam was measured with an Omega KFG-02-120-C1-11L3M3R strain gage. A NI USB-6221 data acquisition device was used to interface input and output signals with Labview, and sampling rates of either 1000 or 10000 Hz were used. The impact of driving acceleration, driving frequency, mass, and mass starting position on the behavior of the system were investigated. The effect of changing the moment of inertia of the mass was not investigated in this study but is expected to impact the stability of the mass equilibrium positions.

There were two types of tests conducted to investigate the self-tuning ability of the system. For both types of self-tuning tests, the mass was placed at a chosen initial position and the system was excited at a chosen frequency and acceleration as set in Labview. The system was then left untouched while the mass moved to its equilibrium position. Under certain conditions the mass moved considerable distances along the beam while under other conditions the mass did not move. The mass position over time was recorded using a video camera and visual observation, while the beam's relative amplitude of deflection was quantified from the strain gage voltage output. For the first type of test, the system was shut off once the mass's equilibrium position was reached and the next test parameters were set up before restarting the excitation. Conversely, for the second type of test, the system was left running once the mass had found its equilibrium position and the frequency of excitation was changed in 1 Hz increments over a given range. The purpose of the first type of test was to determine whether the mass would slide to a position that tuned the beam-mass system's resonance frequency to match the driving frequency, and the purpose of the second type of test was to study the ability of the system to stay tuned if frequency was adjusted.

9.3.2 Numerical

The equations from section 8.5 were solved in MATLAB using the ode15s function. The input parameter values used are shown in table 9.1. First, a vector for β_n was defined from 0.5 to 15 with 10,000 linearly spaced values, a vector for mass position, y, was defined from 0 to 1 with 62 linearly spaced values, and a vector for x-position along the beam was defined with 50 points. These vectors were used along with the boundary conditions of the beam to iteratively calculate the resonance frequency, beam shape coefficients, and normalization coefficients for every mass position along the beam, as described in detail in section 8.4. Derivatives of the beam shapes with respect to both x and y were also needed, and were calculated analytically when possible. If there was not a known expression for the parameter's variation with y which needed to be differentiated with respect to y, MATLAB's polyfit and polyval functions were used to curve fit to the parameter calculated at all values of y from the previously defined y vector. Then the polyder function was used to take a polynomial derivative of the fitted curve. The time step typically used for numerical solution was 0.055. The driving frequency, acceleration magnitude, and mass starting position were variables in the numerical code just as they were in the experiment.

Table 9.1: Parameters used in numerical solution of adaptable-frequency resonator

Variable description	Variable	Value	Unit
Beam length	L	30e-2	m
Beam width	W	4.8e-3	m
Beam thickness	H	1.1e-3	m
Beam elastic modulus	E	130e9	Pa
Beam density	ρ	2630	kg/m^3
Number of tungsten masses	n	1	
Mass of tungsten piece	m_{tungsten}	12e-3	kg
Mass length*	L_{mass}	2.51e-2	m
Mass thickness*	H_{mass}	n x 3.22e-3	m
Mass clamp thickness	H_{clamp}	8.13e-3	m
Mass of mass clamp	m_{clamp}	5e-3	kg
Total mass	m	$nm_{\text{tungsten}} + m_{\text{clamp}}$	kg
Beam viscous damping	c_b	0.01	
Mass viscous damping	c_m	0.01	
Sliding friction coefficient	μ	0	
First mode eigenvalue**	λ_1	4.730040744074408	

* If the mass is reoriented relative to the beam to adjust moment of inertia, L_{mass} and H_{mass} must be adjusted accordingly. ** Found by solving the characteristic equation (8.38) numerically with no mass present. The reason for the number of decimal places is that the precision of this value impacts precision of the code and is a way to improve the simulated results without adding much computation time.

9.4 Results

Passive self-tuning was experimentally and numerically demonstrated in the system at a variety of driving frequencies, confirming that an adaptable-frequency resonant system was achieved. The numerical model successfully reproduced the phenomena that were observed experimentally, although there were discrepancies between experiment and model in the exact details of mass motion. The mass moves along the vibrating beam when the sum of the forces from the beam motion and the moment of inertia of the mass have a net component along the length direction of the beam. It was observed that the driving acceleration needed to exceed a critical level, typically about 1.2 - 1.5 g's for this prototype, before the mass would slide to self-tune. At the same time, accelerations above around 3 g's were observed to impede mass motion. Further investigation is needed to determine the full set of acceleration and frequency driving conditions that results in self-tuning behavior. Because the system is very sensitive to driving conditions and the experimental variable space is large, it would be most efficient to use the numerical model to develop a regime map and then verify the model with experimental results.

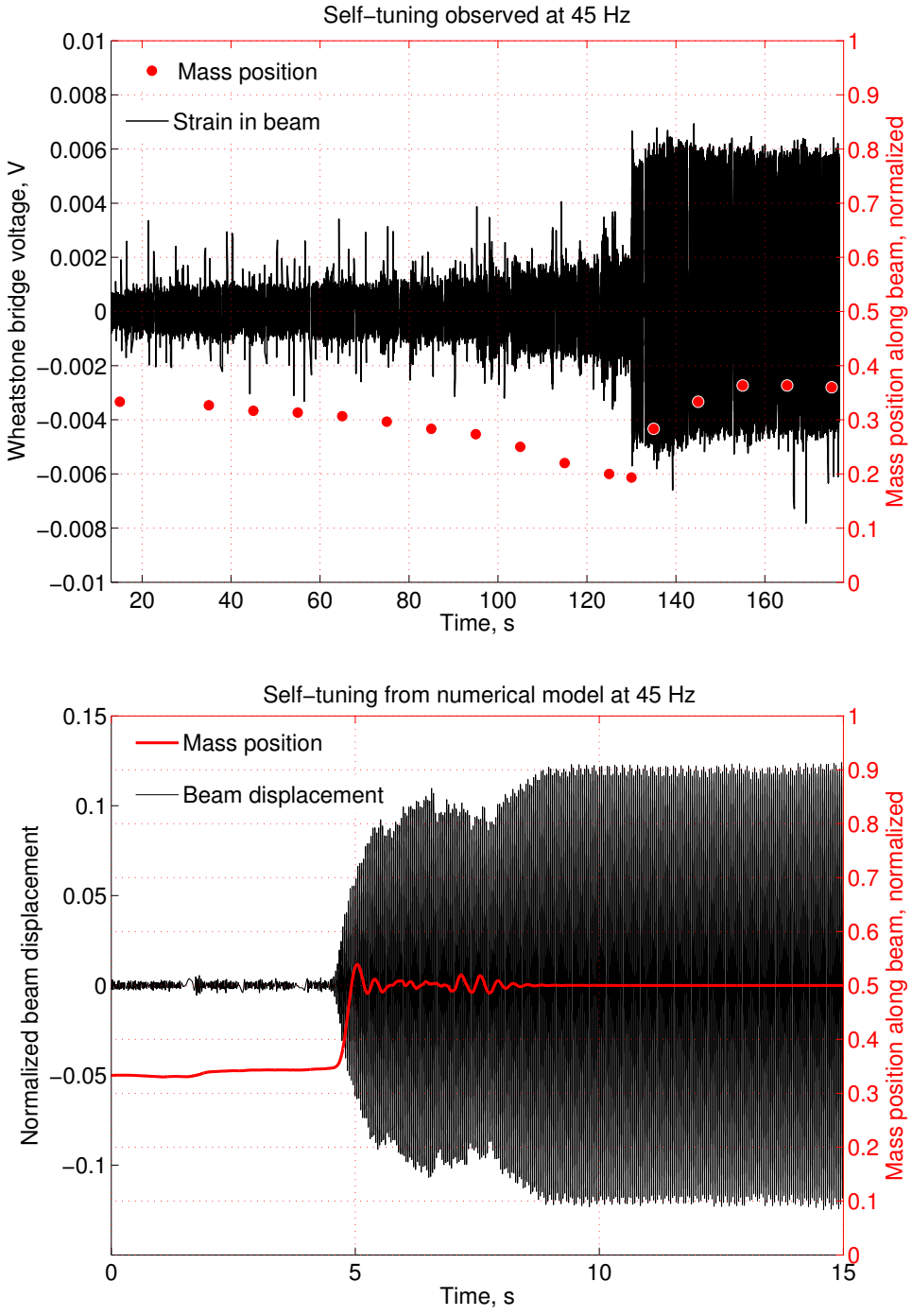

Figure 9.3: Experimental and numerical self-tuning observed with driving frequency of 45 Hz, acceleration of 2 g, and normalized mass starting position of 0.33.

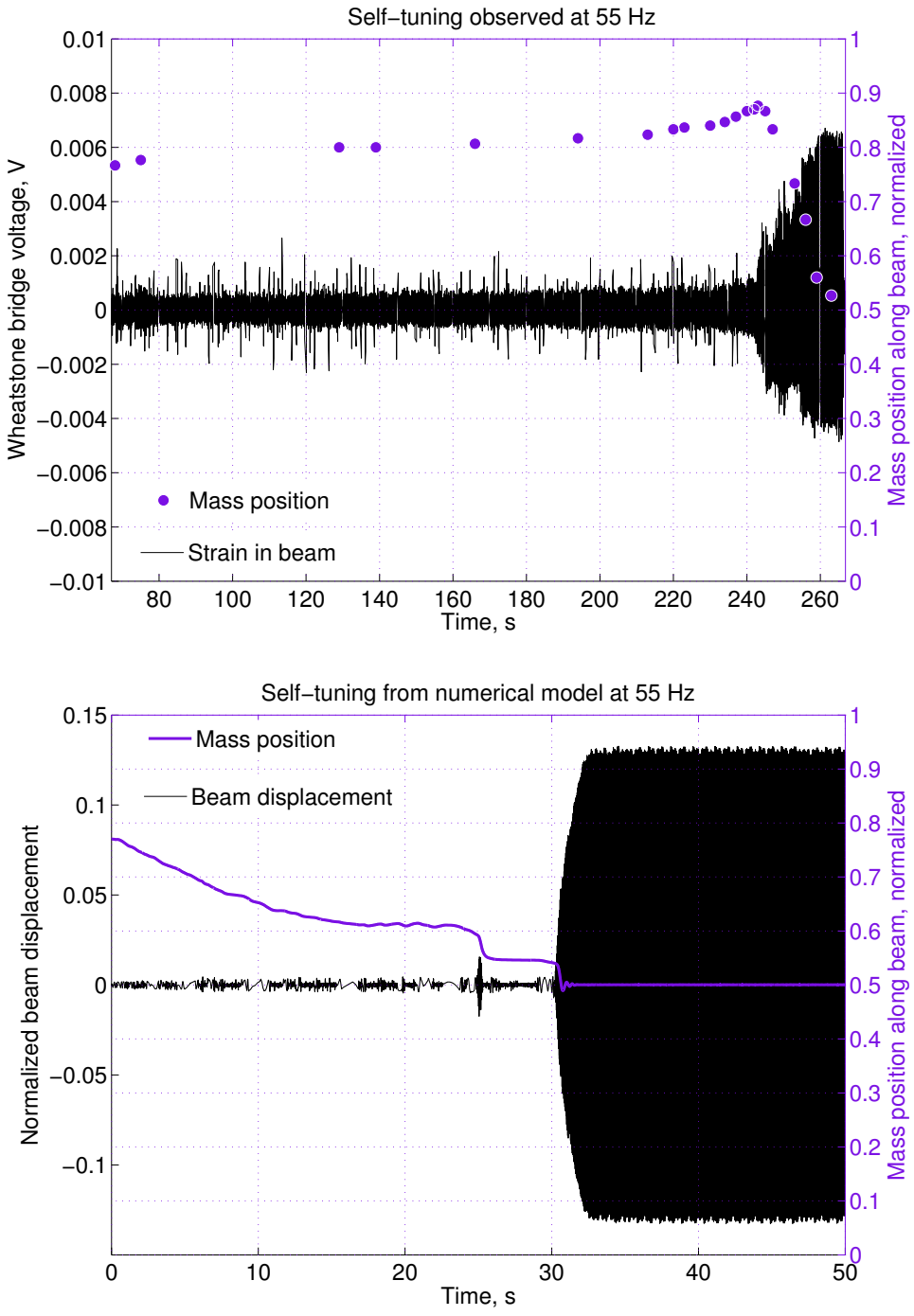

Figure 9.4: Experimental and numerical self-tuning observed with driving frequency of 55 Hz, acceleration of 1.6 g, and normalized mass starting position of 0.77.

The first type of self-tuning tests, where the goal was to determine whether the mass would slide to a position that tuned the beam-mass system's resonance frequency to match the driving frequency, were carried out at 45, 55, 60, and 70 Hz. The experimental and numerically simulated results are shown side by side in figures 9.3, 9.4, 9.5, and 9.6. Both the experiment and model show that the driving vibration of the beam induces the mass to slide, resulting in self-tuning of the system such that resonance is achieved, the beam displacement is amplified, and the mass ends up at the center of the beam. These figures show that, once the mass reaches the resonant position and induces amplified beam motion, the amplified motion of the beam is maintained. The reason that the strain amplitude is higher in one polarity than the other is that the strain gage was mounted on the top surface of the beam rather than both top and bottom.

For the second type of self-tuning tests, where the goal was to investigate the ability of the system to stay tuned as the frequency was adjusted, it was found that the system was fairly robust to maintaining its tuned state once resonance was achieved. The driving frequency could be adjusted significantly before resonance was lost. In one test, the driving frequency was adjusted from 58 Hz to 64 Hz and back without losing resonance with acceleration of 4.5 g, normalized mass starting position of 0.6, and one piece of tungsten mass. In another test, the driving frequency was adjusted from 58 Hz to 67 Hz and back down to 50 Hz without losing resonance with acceleration of 2.4 g, normalized mass starting position of 0.6, and no tungsten mass pieces (only the mass clamp, which has a mass of 5 g). In general, the mass moved in order to maintain resonance of the system, but there were cases where the mass did not move until several Hz frequency change had been made.

Figure 9.7 shows results from a test where the initial driving frequency was 60 Hz and frequency was swept up to 66 Hz, acceleration was 2 g, normalized mass starting position was 0.8, and one piece of tungsten mass was attached. The points in time where frequency was changed are indicated on the plot. The reason that the frequencies were changed rather quickly instead of giving it longer to establish equilibrium is that the system was resonating very intensely and, without end stops in this design to constrain mechanical motion, there was concern that the self-tuning resonator would be damaged. This figure shows that the amplification of beam motion was maintained as frequency was changed, and the mass rearranged itself along the beam in order to maintain this resonance condition.

The top plot of figure 9.8 shows the motions of the sliding mass from figures 9.3, 9.4, 9.5, and 9.6 plotted together. This plot shows that the "turn around" position for the mass, at which point resonance of the beam-mass system begins, moves closer toward the edge of the beam as the frequency increases. The location of the turn around position where the beam-mass system suddenly begins to resonate for a given driving frequency can be explained by the bottom plot of figure 9.8. The bottom plot shows the first and second mode resonance frequencies of the beam-mass system calculated for the case in which the mass is fixed at a given position along the beam (mass position not coupled with beam motion). These results show good agreement between experiment and model, and suggest that the mass motion occurs in two phases. In the first phase, the mass moves slowly along the beam, which

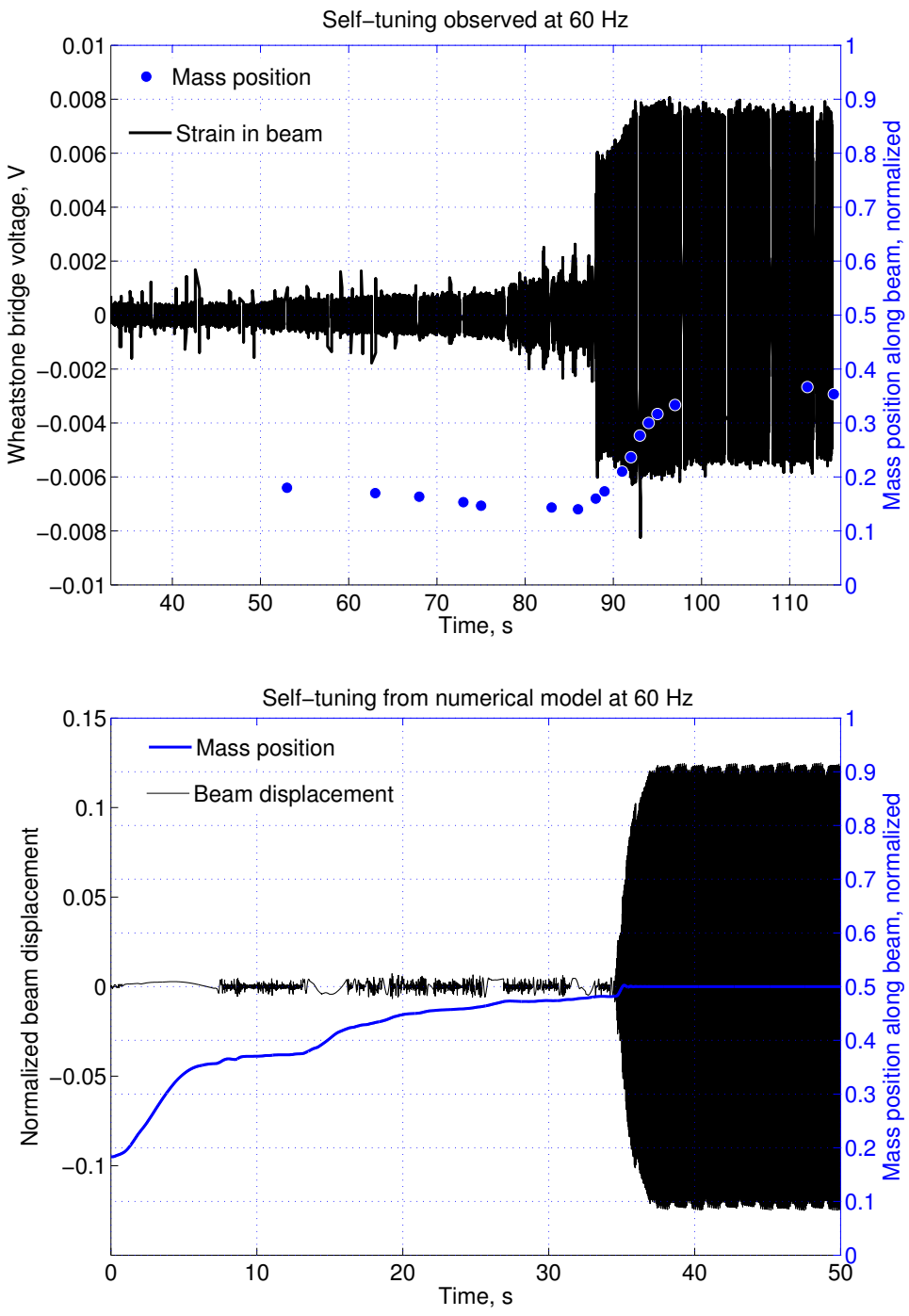

Figure 9.5: Experimental and numerical self-tuning observed with driving frequency of 60 Hz, acceleration of 1.8 g, and normalized mass starting position of 0.1833.

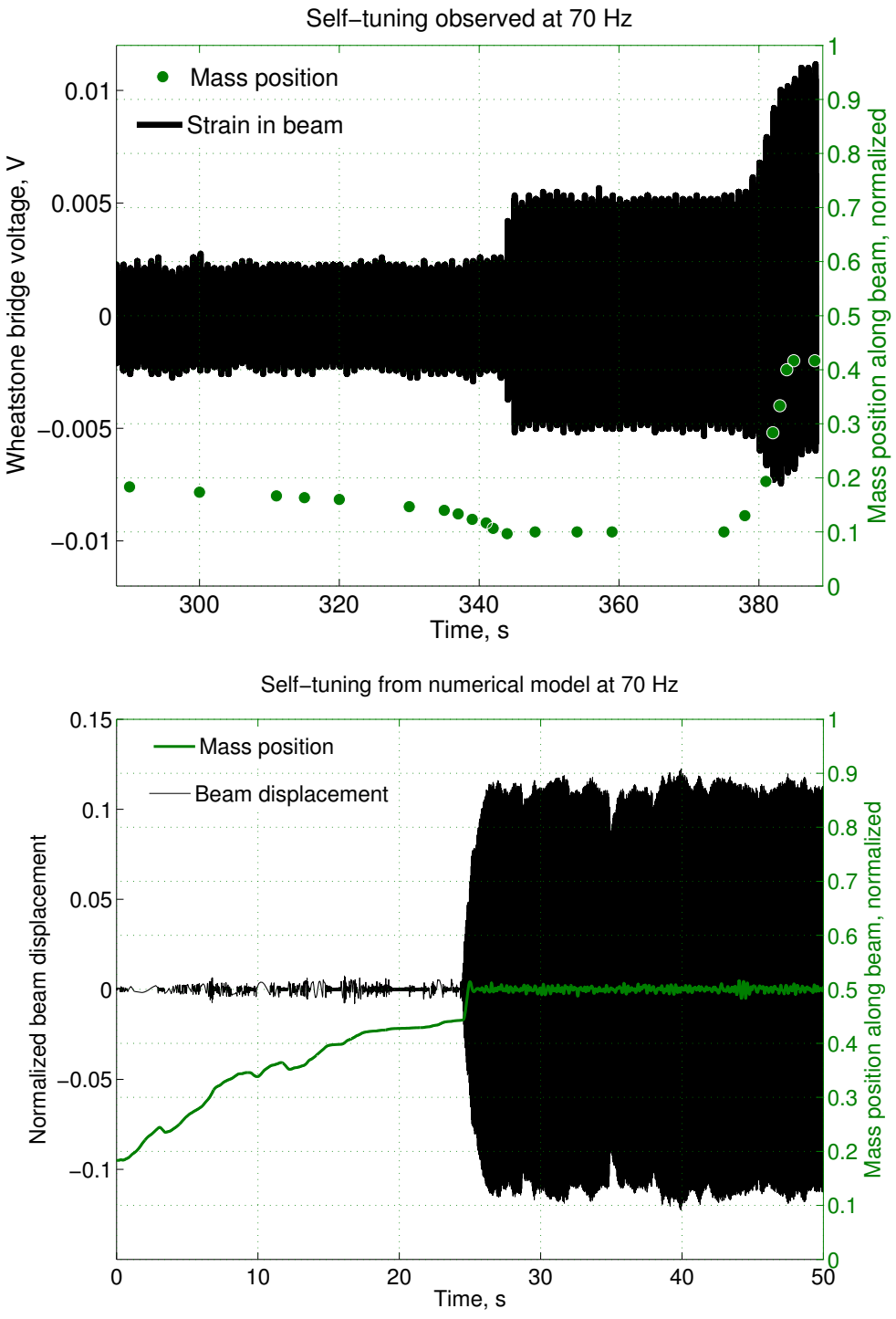

Figure 9.6: Experimental and numerical self-tuning observed with driving frequency of 70 Hz, acceleration of 2 g, and normalized mass starting position of 0.1833.

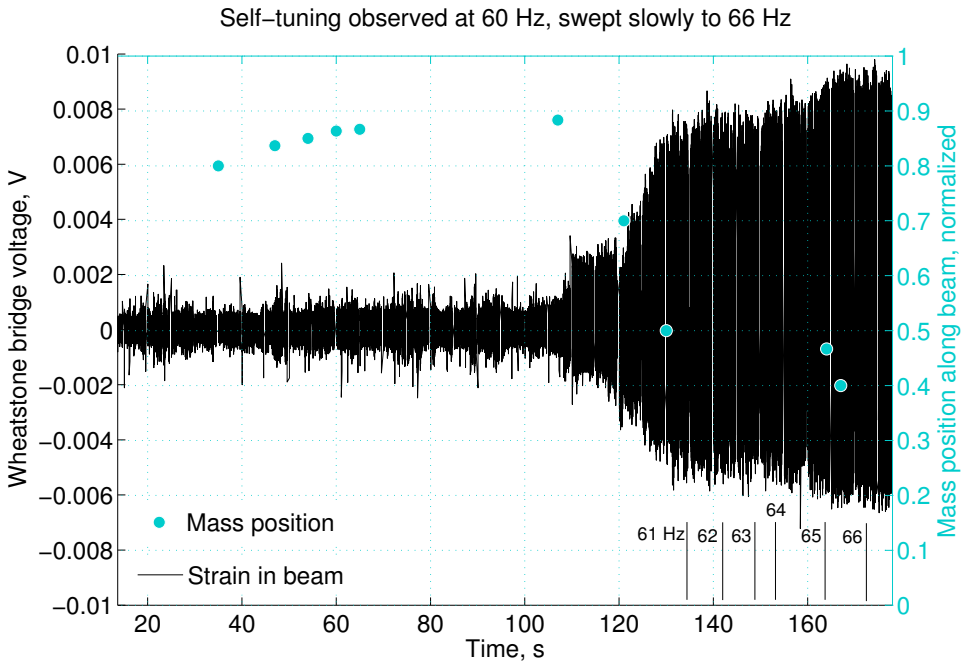

Figure 9.7: Experimentally observed self-tuning as driving frequency was swept from 60 to 66 Hz, with acceleration of 2 g, and normalized mass starting position of 0.8.

is vibrating with small amplitudes, to the position along the beam which would make the beam-mass system resonance frequency match the driving frequency if the mass were fixed rather than free to slide. When the mass reaches that position, the system is at resonance and the displacement amplitude grows. In the second phase, the mass slides rapidly back toward the center of the beam, driven by the suddenly very large amplitude displacement of the beam.

9.5 Discussion

9.5.1 Experimental imperfections

Two factors that impact the experiment and should be accounted for in the next prototype design are nonlinearities introduced due to large deflections of the aluminum beam and interaction of the self-tuning beam-mass system with the mass of the vibrometer. The first effect, nonlinearities due to large beam deflection, is believed to have had only a minor impact on the experiment initially, but during one test the system was driven at higher acceleration than previously and this resulted in observable plastic deformation of the aluminum beam. The data and results reported in this chapter were taken prior to plastic deformation of the beam so there is not a concern of invalid results, but future designs should incorporate

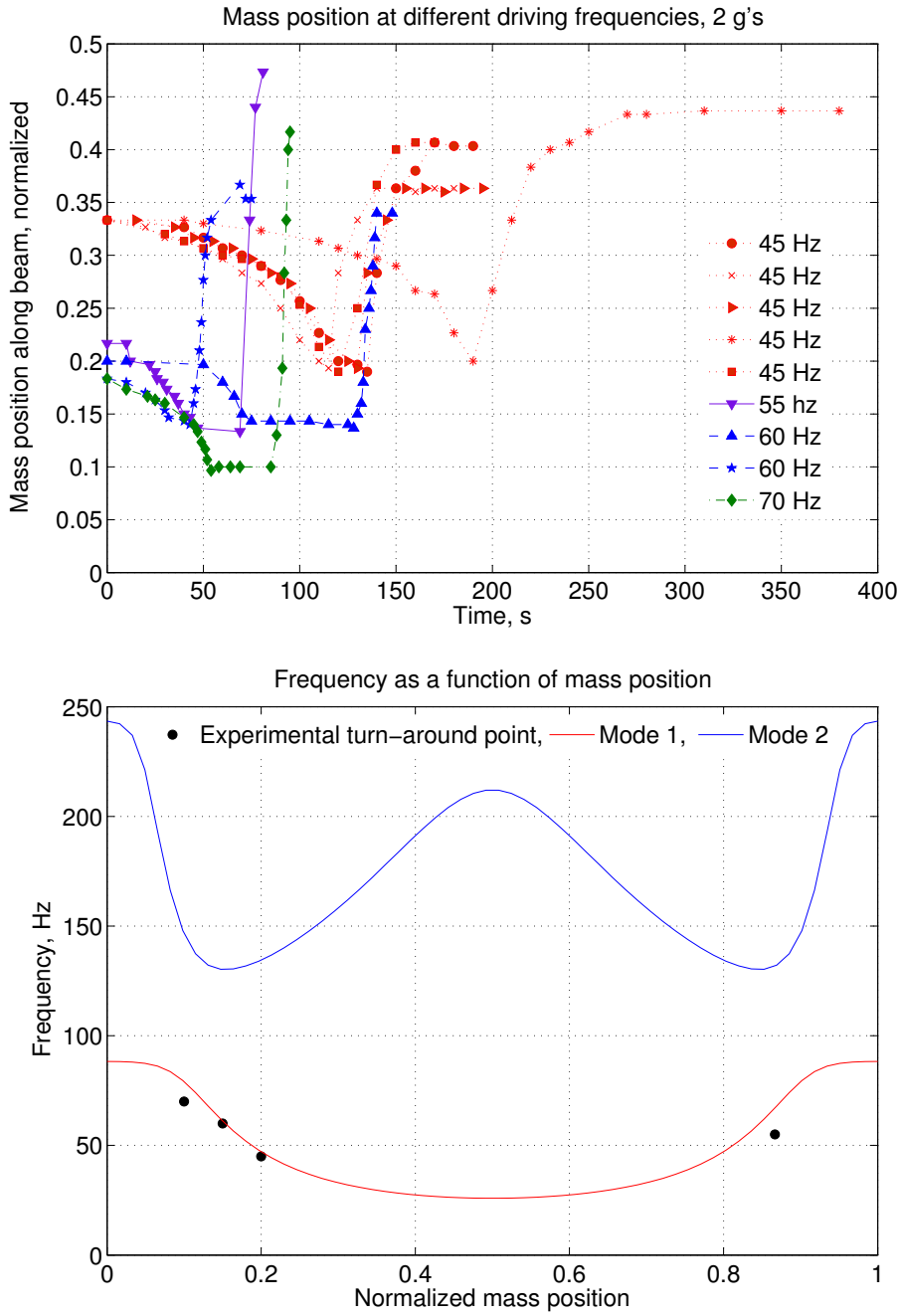

Figure 9.8: Top figure shows experimentally observed mass motion along the vibrating beam at 2 g. Bottom figure shows the uncoupled modeled system frequencies corresponding to each mass position along the beam for first and second modes of beam vibration. Black points correspond with the experimentally observed position at which the mass-beam system began to resonate and mass turned around to move back toward center.

mechanical end stops to prevent excessive displacement or a structural beam material with a higher yield stress than aluminum to avoid plastic deformation issues.

The second effect, interaction of the self-tuning resonator with the mass of the vibrometer, can occur if the mass of the device is on the same order of magnitude as the mass of the shaker and the system is at resonance. Because these conditions could have been met during the testing done for this study, the possibility of the prototype interacting with the vibrometer should be considered. However, the results presented in this chapter clearly show the onset of passive self-tuning, which occurs before and just as resonance begins, even if some interaction with the vibrometer impacts the behavior later on after the system is fully resonating. Therefore, the conclusion that passive self-tuning was achieved is still valid. Future devices should be much smaller than this initial prototype with smaller mass and so interaction with the shaker mass is not expected to be a problem. However, if future devices do have similarly large masses, coupling with the shaker can be avoided by adding extra mass to the base of the resonator system to effectively increase the mass of the vibrometer.

9.5.2 Successes and shortcomings of the model

The model correctly reproduced the main phenomena that were observed experimentally, correctly predicting the equilibrium position of the mass and whether or not self-tuning occurred for a given set of driving parameters and initial conditions. It also successfully captured the mass's slow-moving nature relative to the timescale of beam vibration, and the rapid sliding of the mass toward center as the system became self-tuned and began to resonate. However, it did not accurately reproduce the exact trajectory of the mass along the beam. Specifically, the mass was experimentally observed to move towards the edge of the beam until self-tuning occurred, after which the mass moved towards the center of the beam, while the model showed the mass moving directly towards the center of the beam. It should be noted that the mass slid all the way to the center of the beam in some experimental cases, but in other cases it did not make it all the way back to center. This is due to experimental imperfections, such as friction between the beam and mass, rather than modeling inconsistency. Overall, the model is a very useful tool for understanding this complicated nonlinear coupled system and determining operating regimes, as numerical simulations can be run much more quickly than experimental tests.

The causes of the discrepancies between the model and experiment may stem from both numerical and physical sources. Numerical inaccuracies are introduced with the discrete nature of the input vectors for β_n, y, and x, and the approximated curve fits and derivatives using polyfit, polyval, and polyder functions. Restrictions on the size of the time step due to memory limits of the machine placed a limit on solver resolution. Physical inaccuracies in the model are due to the fact that the model does not account for any torsion in the beam, "walking" behavior of the mass along the beam, or spring nonlinearities of the beam at large deflection. Additionally, although the model has parameters to account for friction and damping, it is difficult to determine accurate coefficients for these terms and this could

be a source of error. Lastly, even though moment of inertia of the mass was accounted for, the model treats the mass contact area with the beam as point contact when in reality it is a rectangular contact area.

9.5.3 Fabrication challenges in micro/meso "no-mans land"

This self-tuning resonator system poses an interesting manufacturing challenge because the dimensions required for a small-scale, low frequency system are on the boundary of what makes sense for MEMS fabrication processes. To scale down to a length of several centimeters and width of several millimeters for the fixed-fixed beam would require beam thickness on the order of tens of microns in order to maintain the necessary low resonance frequencies. The thickness requirement is more suitable for MEMS fabrication, but the large area required is more suitable for meso scale fabrication. Additionally, the use of bulk piezoelectric materials is generally preferable in order to obtain the large coupling coefficients that are difficult to obtain from thin film piezoelectric materials, but the low frequency requirement makes using the thicker bulk piezoelectric sheets challenging. Finally, the requirement that the mass be able to slide along the beam introduces additional complexity for MEMS processing due to fabrication release step difficulties and potential problems with stiction. There is a need for new hybrid manufacturing processes to fabricate this type of system.

9.6 Summary

In this chapter, the design, fabrication, and test results of an adaptable-frequency resonant system were presented. Both the numerical and experimental results show that self-tuning was successfully and repeatably achieved. Further testing and characterization is needed to develop a behavioral regime map of the system's self-tuning behavior at different driving parameters to ensure that a design works over the full frequency range desired. The strengths and shortcomings of the numerical model were discussed. This system is worthy of continued research, including use of the model to develop an smaller optimized device and testing of the system on ambient, rather than sinusoidal, vibration sources.

Chapter 10

Conclusion

10.1 Specific conclusions

1. A detailed survey of ambient vibrations in a machine room setting was conducted, finding that the dominant frequency peaks from the majority of the sources surveyed lie between 20-60 Hz, with another set of frequencies between 120-140 Hz. Three sources also contain peaks around 350 Hz. The accelerations of the ambient vibrations were all below 0.7 $g/\sqrt{Hz}$, with most accelerations on the order of 10^{-2} to 10^{-1} $g/\sqrt{Hz}$.

2. The data suggest that the peak frequencies in the spectra do not usually vary over time, but the relative magnitudes of the frequencies can change significantly. This can be a result of duty cycles of equipment and differences in system settings. In addition to temporal sensitivity, spacial sensitivity was observed when data were gathered from different parts of the same machine or structure.

3. A lumped parameter model for the response of a fixed-frequency piezoelectric energy harvester to an arbitrary input excitation was developed. The model improves upon what was previously presented in literature by accounting for rotational inertia of the proof mass and accounting for rectangular or trapezoidal beam shapes. The discretization method was used to solve the model equations with sampled acceleration inputs such that any arbitrary measured acceleration data can be used as input to the model.

4. Fixed-frequency MEMS piezoelectric energy harvesters with frequencies of 31–232 Hz were successfully fabricated using sol-gel PZT as the piezoelectric thin film. This is the lowest resonance frequency for MEMS energy harvesters reported in literature, and falls within the frequency range of ambient vibrations. The low frequency was achieved by using beam lengths of 4–6 mm and mass areas of 1.5 - 3 mm^2, which are unusually large areal dimensions for MEMS devices, while utilizing the standard thin film capabilities of MEMS to keep the beam only microns thick.

5. Fixed-frequency MEMS piezoelectric energy harvesters were characterized on a vibrometer, producing power output of 1.2 – 43.8 nW_{avg}/g^2, and the best harvester produced 1.72 nW_{avg} at 232 Hz and 0.29 g. The impedance of the energy harvesters tested ranged from 8–42 kΩ and their piezoelectric coefficients ranged from 1.9–18.0 pm/V. The range of values is due to variations in the quality of the piezoelectric film across the wafer and variations from wafer to wafer because of processing factors.

6. Energy was harvested from ambient vibration sources in a campus building machine room using the fabricated MEMS piezoelectric devices. Power output levels were low but repeatable, ranging from 0.63 fW - 202 pW per beam, or 24 pW/g^2 - 10 nW/g^2. This was a successful proof-of-concept, especially given that the energy harvesters were not fully optimized or customized specifically for the vibration sources they were harvesting from. Even though their resonance frequencies fell within the proper range, they were not matched exactly and therefore were not producing maximum possible output.

7. The fixed-frequency energy harvester model accurately predicted the location of frequency peaks in every case tested. However, the model's ability to predict magnitude of peak power output varied. The model predicted peak power output within 10x of the experimental value in 82% of tests, and within 5x the experimental value in 68% of the tests. The model is a useful design tool to visualize what the energy harvester frequency response will look like and estimate the power output within an order of magnitude for an arbitrary ambient vibration source.

8. A new method was developed for frequency modification of MEMS cantilevers using direct-write printing to dispense drops of a proof mass ink onto the tips of the beams. This technique is efficient, fast, easily scalable, and non-destructive. Printing was carried out in ambient conditions after completion of all microfabrication steps, including release. Resonance frequency modification of more than 20 Hz with a resolution of 0.1 Hz was repeatably achieved, and greater frequency shift and resolution are possible with modifications to the experimental setup.

9. A geometrically optimized MEMS scale harvester with a matched resistive load produces several μW of power from ambient vibrations, according to the model, which is enough to be usable. The optimal dimensions are approximately 0.3 mm beam length and 3 μm silicon layer thickness, depending on driving frequency. A harvester optimized for a specific frequency cannot produce usable power at a different frequency. The power output from a device optimized for a single frequency sine wave input is about an order of magnitude higher than a device optimized for ambient vibration input.

10. Fixed-frequency devices are insufficient for energy harvesting in most real-world conditions. No matter how perfectly a device is optimized and manufactured, it will only

work well at its resonance frequency. In harvesting environments, however, vibration source frequencies change over time and are not usually known *a priori*, before the energy harvester is designed. Therefore, a broadband or tunable energy harvester design is needed in order to achieve a device that can function effectively on different vibration sources over a long span of time.

11. It is of interest to optimize the energy harvester with an electrical load more useful than a resistor in order to take into account power conditioning, but the system equations can be quite complicated due to coupling between the electrical and mechanical systems. An analytical framework in which the piezoelectric harvester is represented as a Coulomb-damped resonant generator was developed to enable the full system optimization of the energy harvester connected with a synchronous pre-biasing interface circuit for power conditioning.

12. A derivation was carried out to find the continuous coupled nonlinear equations of motion for a spring mass system consisting of a fixed-fixed beam with a sliding proof mass. The model for an adaptable-frequency resonator improves upon research in the literature in that it analyzes a beam, rather than a string, with fixed-fixed instead of cantilever boundary conditions. It accounts for rotary inertia of the mass about the beam, rather than treating it as a point mass, and for the mass's impact on beam shape. The model is applicable for multiple Eigenmodes of beam excitation rather than only the first mode.

13. A meso scale prototype adaptable-frequency resonator was built to test the self-tuning concept and validate the model. Self-tuning was repeatably observed in the experimental prototype over a range of frequencies. Rich nonlinear behavior was observed as frequency, acceleration, and mass starting position were varied.

14. The adaptable-frequency resonator model correctly reproduced the important phenomena that were observed experimentally, correctly predicting the equilibrium position of the mass and whether or not self-tuning occurred for a given set of driving parameters and initial conditions. It also successfully captured the mass's slow-moving nature relative to the timescale of beam vibration, and the rapid sliding of the mass toward center as the system became self-tuned and began to resonate.

15. The model did not accurately reproduce the exact trajectory of the mass along the beam. Discrepancies are attributed to numerical inaccuracies as well as torsional motion, "walking" behavior of mass, and nonlinear elastic response from the beam that are not accounted for in the model, and difficulty achieving realistic depiction of viscous damping and sliding friction in the model.

10.2 General conclusions

1. MEMS piezoelectric energy harvesting can be a viable power supply for power wireless sensor nodes as long as harvester is either optimized for specific source or designed to be broadband or self tuning. Additionally, the wireless sensor node must be designed to be compatible with the power levels achievable with the harvester.

2. Realistic operating environments must be taken into account when designing and testing energy harvesters. An energy harvester that performs well when driven by a single sinusoidal acceleration at the same frequency as the harvester's resonance may produce no energy when mounted on an arbitrary ambient vibration source.

3. Some applications are only possible using MEMS energy harvesters but others are far less sensitive to size constraints. If size constraints are not an issue, small meso scale devices should be considered as a power source along with MEMS devices.

10.3 Recommendations for future work

1. Lead zirconate titanate (PZT) should be replaced by aluminum nitride (AlN), or another suitable material, for MEMS scale piezoelectric harvesters. This recommendation is based on the fact that, in general, it is easier to achieve a high quality AlN than PZT thin film, AlN is CMOS compatible and nontoxic while PZT is not, and the piezoelectric coupling coefficient of AlN is comparable to that of PZT.

2. Future efforts in vibration energy harvesting research should emphasize investigation and development of self-tuning methods including, but not limited to, that of a sliding proof mass on a fixed-fixed beam.

3. Future work in vibration energy harvesting should focus on integrating electrical power conditioning and mechanical device design research rather than pursuing these separately.

Bibliography

[1] I.N. Ayala, D. Zhu, M.J. Tudor, and S.P. Beeby. Autonomous tunable energy harvester. In *Technical Digest PowerMEMS*, pages 49–52, 2009.

[2] V I Babitsky and A M Veprik. Damping of beam forced vibration by a moving washer. *Journal of Sound and Vibration*, 166(1):77–85, 1993.

[3] Thomas G Bifano, Harley T Johnson, Paul Bierden, and Raji Krishnamoorthy Mali. Elimination of stress-induced curvature in thin-film structures. *Journal of Microelectromechanical Systems*, 11:592–597, 2002.

[4] Lars-Cyril J Blystad, Einar Halvorsen, and Svein Husa. Piezoelectric mems energy harvesting systems driven by harmonic and random vibrations. *IEEE Transactions on Ultrasonics, Ferroelectrics and Frequency Control*, 57:908–19, 2010.

[5] A Boudaoud, Y Couder, and M Ben Amar. A self-adaptive oscillator. *European Physics Journal B*, 9:159–165, 1999.

[6] Kari Burman and Andy Walker. Ocean energy technology overview, doe/go-102009-2823. Technical report, US Department of Energy, Energy Efficiency and Renewable Energy, 2009.

[7] F Calame. Growth and properties of gradient free sol-gel lead zirconate titanate thin films. *Applied Physics Letters*, 90:062907, 2007.

[8] Chi-Tsong Chen. *Linear System Theory and Design*. Oxford University Press, 3nd edition, 1999.

[9] R D'hulst and J Driesen. Power processing circuits for vibration based energy harvesters. In *Power Electronics Specialists Conference*, 2008.

[10] James Dicken, Paul D Mitcheson, I Stoianov, and Eric M Yeatman. Power-extraction circuits for piezoelectric energy harvesters in miniature and low-power applications. *IEEE Transactions on Power Electronics and Industrial Electronics Special Issue 2012*, 2012.

[11] Noel E. duToit, Brian L. Wardle, and Sang-Gook Kim. Design consideration for mems-scale piezoelectric mechanical vibration energy harvesting. *Integrated Ferroelectrics*, 71:121–160, 2005.

[12] F F C Duval, S A Wilson, G Ensell, N M P Evanno, M G Cain, and R W Whatmore. Characterisation of pzt thin film micro-actuators using a silicon micro-force sensor. *Sensors and Actuators A*, 133:35 – 44, 2007.

[13] Christoph Eichhorn, Frank Goldschmidtboeing, Y Porro, and Peter Woias. A piezoelectric harvester with an integrated frequency tuning mechanism. In *Technical Digest PowerMEMS*, pages 45–48, 2009.

[14] R Elfrink, T M Kamel, M Goedbloed, S Matova, D Hohlfeld, Y van Andel, and R van Schaijk. Vibration energy harvesting with aluminum nitride-based piezoelectric devices. *Journal of Micromechanics and Microengineering*, 19:094005, 2009.

[15] Alper Erturk and Daniel Inman. A distributed parameter electromechanical model for cantilevered piezoelectric energy harvesters. *Journal of Vibration and Acoustics*, 130:041002, 2008.

[16] Hua-Bin Fang, Jing-Quan Liu, Zheng-Yi Xu, Lu Dong, Li Wang, Di Chen, Bing-Chu Cai, and Yue Liu. Fabrication and performance of mems-based piezoelectric power generator for vibration energy harvesting. *Microelectronics Journal*, 37:1280–1284, 2006.

[17] Frank Goldschmidtboeing and Peter Woias. Characterization of different beam shapes for piezoelectric energy harvesting. *Journal of Micromechanics and Microengineering*, 18:104013, 2008.

[18] Daniel Guyomar, Adrien Badel, Elie Lefeuvre, and Claude Richard. Toward energy harvesting using active materials and conversion improvement by nonlinear processing. *IEEE Transactions on Ultrasonics, Ferroelectrics, and Frequency Control*, 52:584–595, 2005.

[19] Einar Halvorsen. Energy harvester driven by broadband random vibrations. *Journal of Microelectromechanical Systems*, 17(5):1061–1071, 2008.

[20] Einar Halvorsen and Tao Dong. Analysis of tapered beam piezoelectric energy harvesters. In *Proceedings of PowerMEMS2008*, Sendai, Japan, November 2008.

[21] Christine C Ho, James W Evans, and Paul K Wright. Direct write dispenser printing of zinc microbatteries. In *Technical Digest PowerMEMS*, pages 141–144, 2009.

[22] Christine C Ho, James W Evans, and Paul K Wright. Direct write dispenser printing of a zinc microbattery with an ionic liquid gel electrolyte. *Journal of Micromechanics and Microengineering*, 20:104009, 2010.

[23] Christine C Ho, Daniel A Steingart, James W Evans, and Paul K Wright. Tailoring electrochemical capacitor energy storage using direct write dispenser printing. *ECS Transactions*, 16(1):35–47, 2008.

[24] http://www.analog.com/static/imported-files/data sheets/ADXL345.pdf. Analog devices adxl345 datasheet, March 2012.

[25] http://www.dustnetworks.com/products/list. Dust networks smartmesh ip dn6000/m6000 datasheet, March 2012.

[26] http://www.memsnet.org/material/, February 2010.

[27] http://www.st.com/internet/com/TECHNICAL RESOURCES/TECHNICAL-LITERATURE/DATASHEET/CD00274221.pdf. Stmicroelectronics lis3dh datasheet, March 2012.

[28] Nicholas S Hudak and Glenn G Amatucci. Small-scale energy harvesting through thermoelectric, vibration, and radiofrequency power conversion. *Journal of Applied Physics*, 103:101301, 2008.

[29] Takuro Ikeda. *Fundamentals of Piezoelectricity*. Oxford University Press, 1990.

[30] Y.B. Jeon, R. Sood, J. h. Jeong, and S.-G. Kim. Mems power generator with transverse mode thin film pzt. *Sensors and Actuators A*, 122:16–22, 2005.

[31] F Khalily, M F Golnaraghi, and G R Heppler. On the dynamic behaviour of a flexible beam carrying a moving mass. *Nonlinear Dynamics*, 5:493–513, 1994.

[32] Inna Kozinsky. Study of passive self-tuning resonator for broadband power harvesting. In *Technical Digest PowerMEMS*, pages 388–391, 2009.

[33] D Lee, G Carman, D Murphy, and C Schulenburg. Novel micro vibration energy harvesting device using frequency up conversion. In *Proceedings of 14th International Conference on Solid-State Sensors, Actuators and Microsystems, 10-14 June, Lyon*, pages 871–874, 2007.

[34] Elie Lefeuvre, Adrien Badel, Claude Richard, and Daniel Guyomar. Piezoelectric energy harvesting device optimization by synchronous electric charge extraction. *Journal of Intelligent Material Systems and Structures*, 16:865, 2005.

[35] Elie Lefeuvre, Adrien Badel, Claude Richard, and Daniel Guyomar. Energy harvesting using piezoelectric materials: Case of random vibrations. *Journal of Electroceramics*, 19:349–355, 2007.

[36] Eli Leland. *A MEMS sensor for AC electric current*. PhD thesis, University of California, Berkeley, 2009.

[37] Eli Leland and Paul K Wright. Resonance tuning of piezoelectric vibration energy scavenging generators using compressive axial preload. *Smart Materials and Structures*, 15:1413–1420, 2006.

[38] M Marzencki, B Charlot, S Basrour, M Colin, and L Valbin. Design and fabrication of piezoelectric micro power generators for autonomous microsystems. In *Symp. on Design Testing Integration and Packaging of MEMS/MOEMS*, Montreux, Switzerland, 2005.

[39] Marcin Marzencki, Yasser Ammar, and Skandar Basrour. Integrated power harvesting system including a mems generator and a power management circuit. *Sensors and Actuators A*, 145-146:363–370, 2008.

[40] Marcin Marzencki, Maxime Defosseux, and Skandar Basrour. Mems vibration energy harvesting devices with passive resonance frequency adaptation capability. *Journal of Microelectromechanical Systems*, 18(6):1444–1453, 2009.

[41] Daigo Miki, Yuji Suzuki, and Nobuhide Kasagi. Effect of nonlinear external circuit on electrostatic damping force of micro electret generator. In *Solid-State Sensors, Actuators and Microsystems Conference TRANSDUCERS*, 2009.

[42] Lindsay M Miller, Alic Chen, Paul K Wright, and James Evans. Resonance frequency modification of mems vibration energy harvesters using dispenser-printed proof mass. In *Proceedings of PowerMEMS2010*, Leuven, Belgium, December 2010.

[43] Lindsay M Miller, Einar Halvorsen, Tao Dong, and Paul K Wright. Modeling and experimental verification of low-frequency mems energy harvesting from ambient vibrations. *Journal of Micromechanics and Microengineering*, 21:045029, 2011.

[44] Lindsay M Miller, Christine C Ho, Padraic C Shafer, Paul K Wright, James W Evans, and R Ramesh. Integration of a low frequency, tunable mems piezoelectric energy harvester and a thick film micro capacitor as a power supply system for wireless sensor networks. In *Proc. IEEE Energy Conversion Congress & Expo*, 2009.

[45] E C Miranda and J J Thomsen. Vibration induced sliding: theory and experiment for a beam with a spring-loaded mass. *Nonlinear Dynamics*, 16:167–186, 1998.

[46] Paul D Mitcheson, Tim C Green, Eric M Yeatman, and Andrew S Holmes. Architectures for vibration-driven micropower generators. *Journal of Microelectromechanical Systems*, 13:429–440, 2004.

[47] Jong Cheol Park, Jae Yeong Park, and Yoon-Pyo Lee. Modeling and characterization of piezoelectric d_{33}-mode mems energy harvester. *Journal of Microeletromechanical Systems*, 19(5):1215–1222, 2010.

[48] R Ramesh and Nicola A Spaldin. Multiferroics: progress and prospects in thin films. *Nature Materials*, 6:21–29, 2007.

[49] Singiresu S. Rao. *Vibrations of continuous systems*. John Wiley & Sons, 2007.

[50] J Rastegar, C Pereira, and H-L Nguyen. Piezoelectric-based power sources for harvesting energy from platforms with low- frequency vibration. In *Proceedings SPIE*, 2006.

[51] Elizabeth K Reilly, Lindsay M Miller, Romy Fain, and Paul K Wright. A study of ambient vibrations for piezoelectric energy conversion. In *Technical Digest PowerMEMS*, pages 312–315, 2009.

[52] M. Renaud, K. Karakaya, T. Sterken, P. Fiorini, C. Van Hoof, and R Puers. Fabrication, modelling and characterization of mems piezoelectric vibration harvesters. *Sensors and Actuators A*, 145-146:380–386, 2008.

[53] Shad Roundy. *Energy Scavenging for Wireless Sensor Nodes with a Focus on Vibration to Electricity Conversion*. PhD thesis, University of California Berkeley, 2003.

[54] Shad Roundy, Paul K. Wright, and Jan Rabaey. A study of low level vibrations as a power source for wireless sensor nodes. *Computer Communications*, 26:1131–1144, 2003.

[55] Michael Seeman, Seth Sanders, and Jan Rabaey. An ultra-low-power power management ic for energy-scavenged wireless sensor nodes. In *IEEE 39th Power Electronics Specialists Conference Proceedings*, pages 925–931, June 2008.

[56] S. M. Shahruz. Design of mechanical band-pass filters with large frequency bands for energy scavenging. *Mechatronics*, 16:523–531, 2006.

[57] Dongna Shen, Jung-Hyun Park, Jyoti Ajitsaria, Song-Yul Choe, Howard C Wikle III, and Dong-Joo Kim. The design, fabrication and evaluation of a mems pzt cantilever with an integrated si proof mass for vibration energy harvesting. *Journal of Micromechanics and Microengineering*, 18:055017, 2008.

[58] Henry A. Sodano, Daniel J. Inman, and Gyuhae Park. Generation and storage of electricity from power harvesting devices. *Journal of Intelligent Material Systems and Structures*, 16:67–75, 2005.

[59] Mostafa S. M. Soliman, Eihab M. Abdel-Rahman, Ehad F. El-Saadany, and Raafat R. Mansour. A design procedure for wideband micropower generators. *Journal of Microelectromechanical Systems*, 18(6):1288–1299, 2009.

[60] S C Stanton, C C McGehee, and B P Mann. Reversible hysteresis for broadband magnetopiezoelastic energy harvesting. *Applied Physics Letters*, 95:174103, 2009.

[61] Gilbert Strang. *Introduction to Linear Algebra*. Wellesly-Cambridge Press, 2nd edition, 1998.

[62] Ellad B. Tadmore and Gabor Kosa. Electromechanical coupling correction for piezoelectric layered beams. *Journal of Microelectromechanical Systems*, 12:899–906, 2003.

[63] L Tang, Y Yang, and C-K Soh. Toward broadband vibration-based energy harvesting. *Journal of Intelligent Material Systems and Structures*, 21:1867–1897, 2010.

[64] JJ Thomsen. Vibration suppression by using self-arranging mass: effects of adding restoring force. *Journal of Sound and Vibration*, 197 (4):403–425, 1996.

[65] Lars Geir Whist Tvedt, Duy Son Nguyen, and Einar Halvorsen. Nonlinear behavior of an electrostatic energy harvester under wide- and narrowband excitation. *Journal of Microelectromechanical Systems*, 19(2):305–316, 2010.

[66] Andrew C Waterbury. *Vibration harvesting using electromagnetic transduction*. PhD thesis, University of California Berkeley, 2011.

[67] Lee A Weinstein, Martin R Cacan, Peter M So, and Paul K Wright. Vortex shedding induced energy harvesting from piezoelectric materials in heating, ventilation and air conditioning flows. *Smart Materials and Structures*, 21:045003, 2012.

[68] Paul K Wright, David A Dornfeld, Alic Chen, Christine C Ho, and James W Evans. Dispenser printing for prototyping microscale devices. In *Trans. of NAMRI/SME*, number 38, pages 555–561, 2010.

[69] J Yang, Y Wen, P Li, X Dai, and M Li. Design, analysis of broadband vibration energy harvesting using magnetoelectric transducer. In *Proceedings PowerMEMS 2010, Leuven, Belgium, 1-3 December 2010*, 2010.

[70] Yiping Zhu. *Study on silicon-based ferroelectric micromachined ultrasonic transducers*. PhD thesis, Tsinghua University, 2007.

Appendix A

Detailed Survey of Ambient Vibrations

A.1 Spectra of 23 vibration sources

This Appendix presents power spectral density plots for all 23 of the vibration sources listed in Table 2.1 of Chapter 2, and data was collected as described there. The plots in this Appendix show only the spectra from 0 to 200 Hz since that is where nearly all of the dominating frequency peaks appear. This can be understood by looking at Figure 2.2 of Chapter 2.

The graphs are grouped according to type of vibration source. Vibrations from HVAC fans are shown figures A.1 and A.2, HVAC ducts are in figures A.3 and A.4, and motors are in figures A.5 and A.6. The x-axes are all identical on the following plots, but y-axes are different to better visualize the details of the peaks. Unfortunately, the magnitude of the ambient vibrations varies too much to use an identical y-axis for all plots.

The general conclusions from the observations in this survey are that ambient vibrations are low amplitude (on the order of 0.1 to 0.01 g's), and are low frequency (typically under 200 Hz) and multi frequency. Additionally, nearly every vibration source had a unique spectra. The survey showed a surprising lack of consistent peaks at the 60 and 120 Hz frequencies that are commonly assumed to be present due to the power mains. For energy harvesting, this means that a "one size fits all" solution may be hard to attain without a passively self-tuning device.

A.2 Spectra of 1 vibration source over time

This section presents the results of a survey of the compressor base vibrations over time. These results are typical of vibration sources in general that were observed over time. Data were collected over a period of several months, with some data points minutes, hours, and

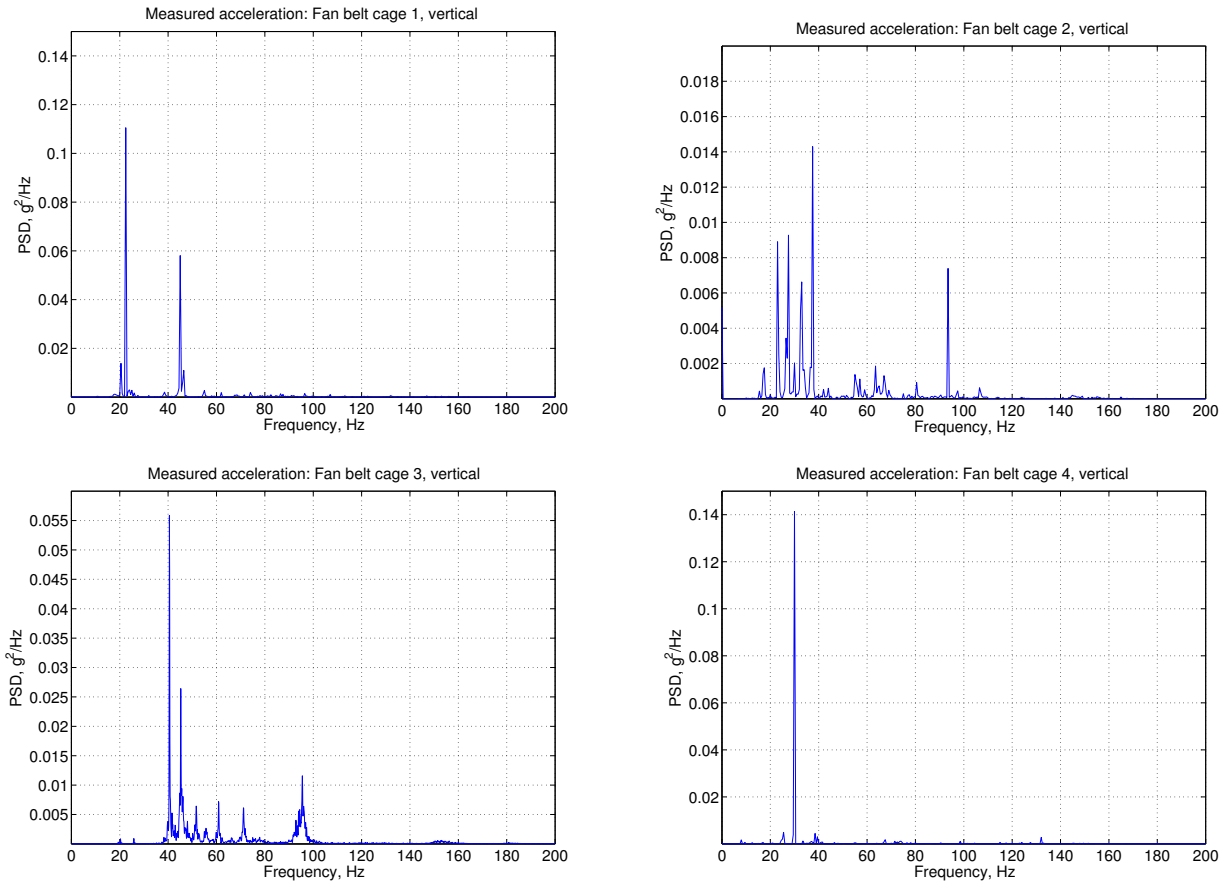

Figure A.1: Vertical fan belt cage vibrations

days apart. The data collection method was the same as described in Chapter 2.

Figure A.7 shows all of 18 spectra from various point in time on the same graph. Figure A.8 shows two plots with semi-log scale. The purpose of the top plot is to illustrate the full 0 to 1000 Hz frequency spectrum for the compressor base so that it is clear why the rest of the plots show the spectra only from 0 to 200 Hz. The frequencies above 200 Hz are much lower magnitude and so are not the focus for harvesting. The lower plot shows the frequency spectrum when the compressor is in the idle mode of its cycle.

The conclusions based on observations of this survey over time are:

1. The dominant frequency peak locations are fairly consistent, within 1 Hz, over time.
2. There are smaller frequency peaks that appear and disappear over time.
3. The relative magnitude of frequency peaks changes over time.
4. Sometimes one of the dominant frequency peaks decreases to the point where a different frequency dominates.

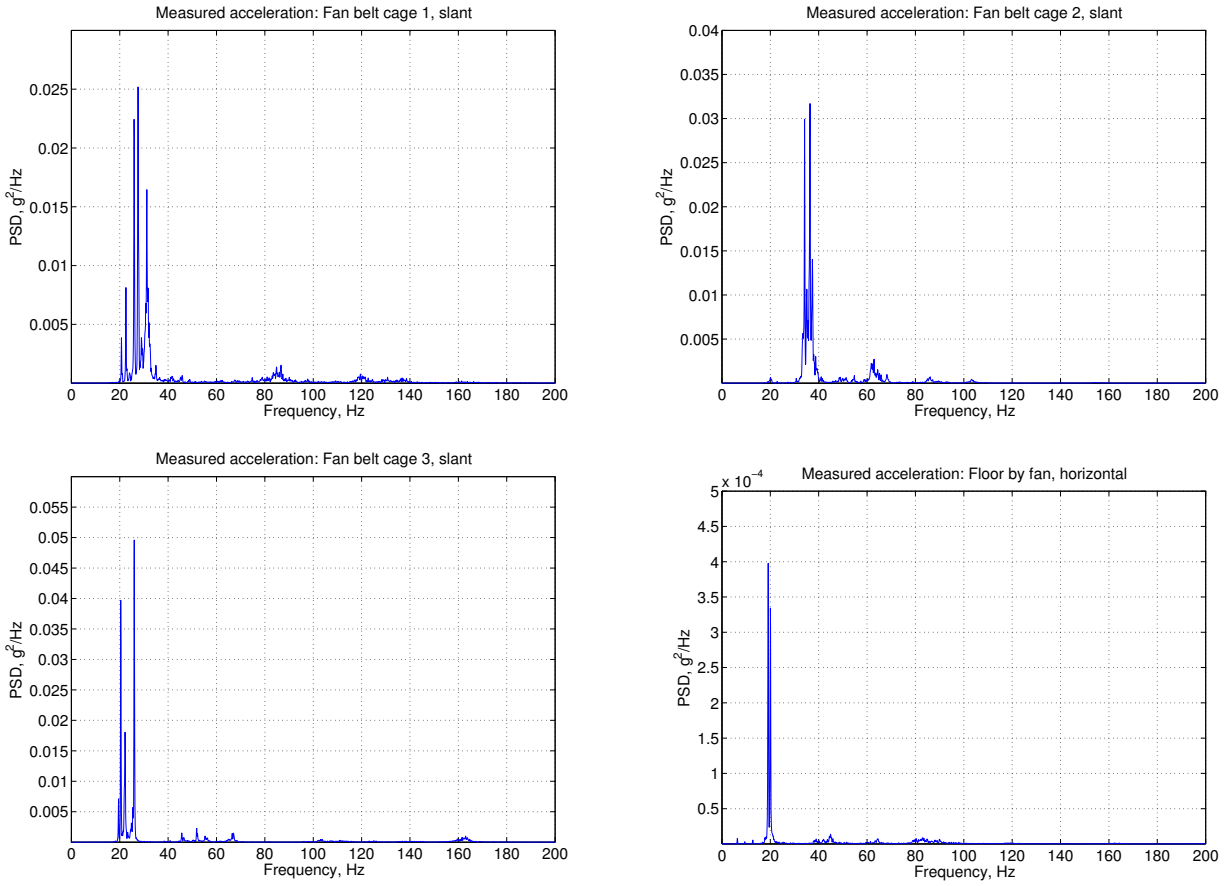

Figure A.2: Slanted and horizontal fan belt cage vibrations

Relating these conclusions back to energy harvesting, it becomes clear that an energy harvesting device tuned to a resonance frequency corresponding to one of the dominant frequency peaks will be able to harvest some energy some of the time. However, it may be essentially useless for unpredictable lengths of time if the vibration source cycles into a mode that causes a shift of frequencies. This is part of the motivation for seeking a passively self-tuning energy harvester design.

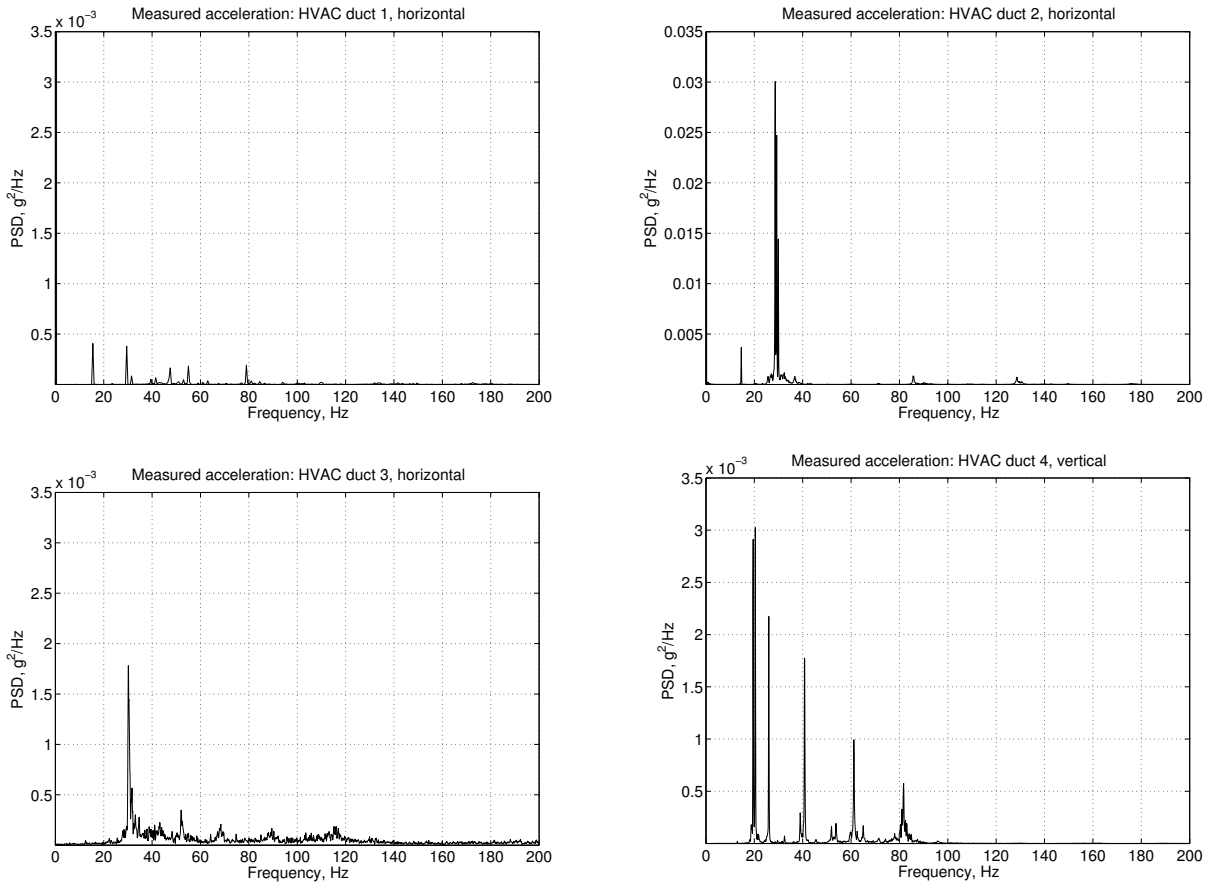

Figure A.3: HVAC duct vibrations 1-4

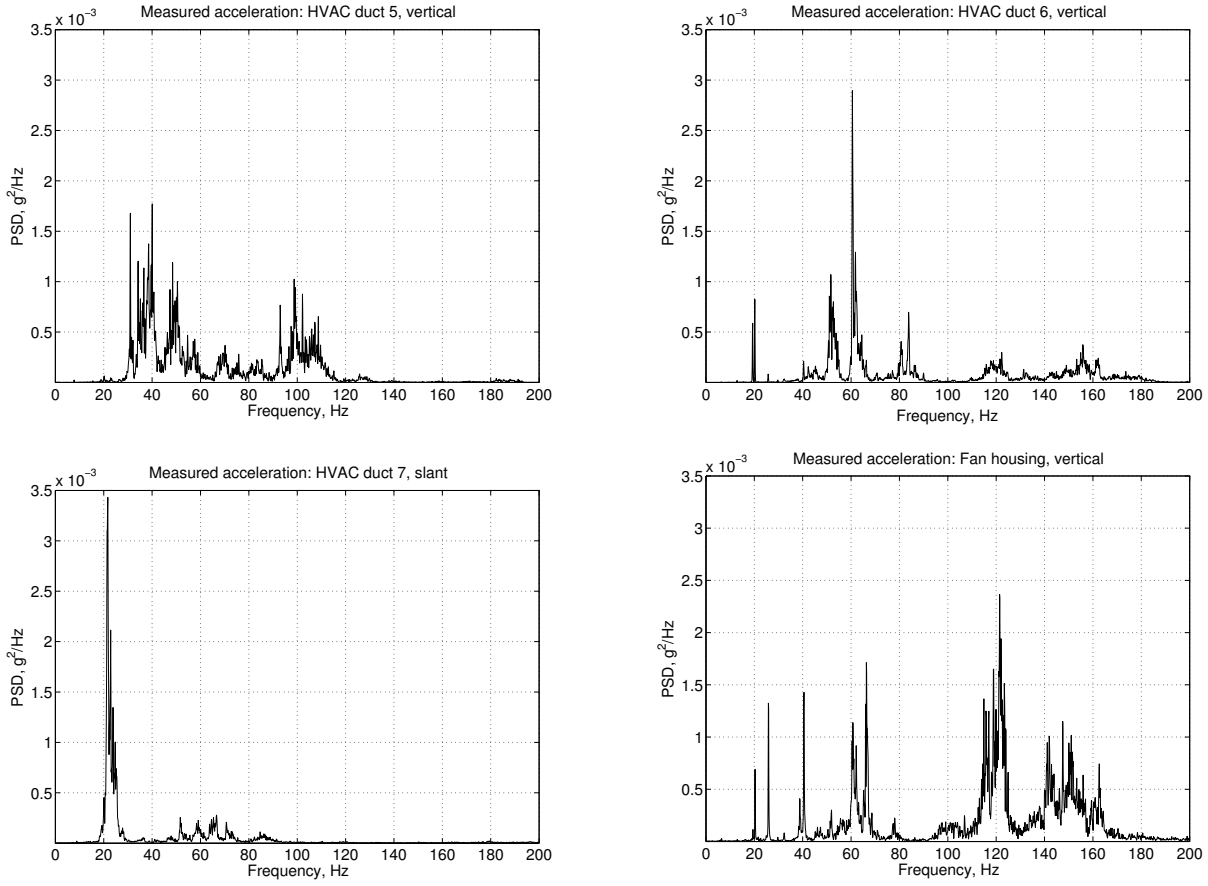

Figure A.4: HVAC duct vibrations 5-8

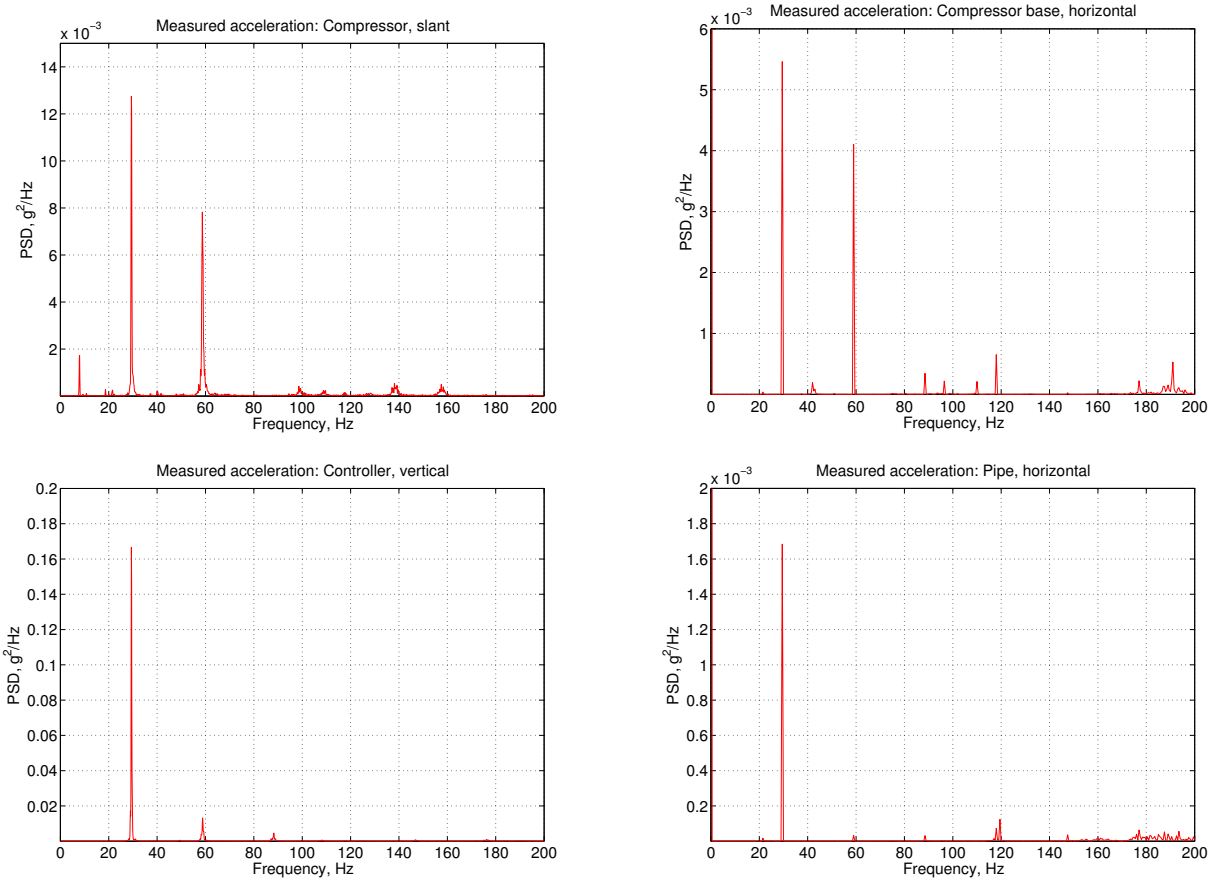

Figure A.5: Motor-induced vibrations 1-4

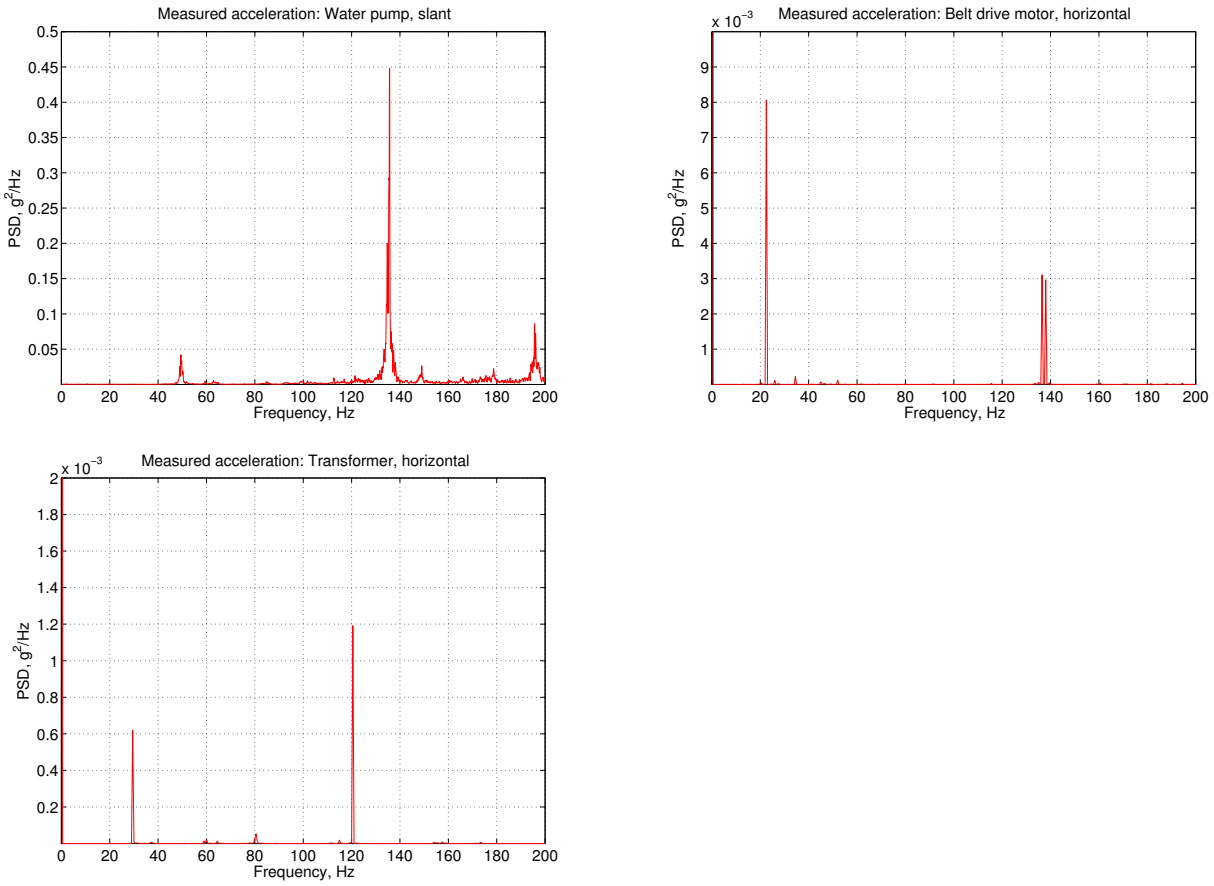

Figure A.6: Motor-induced vibrations 5-7

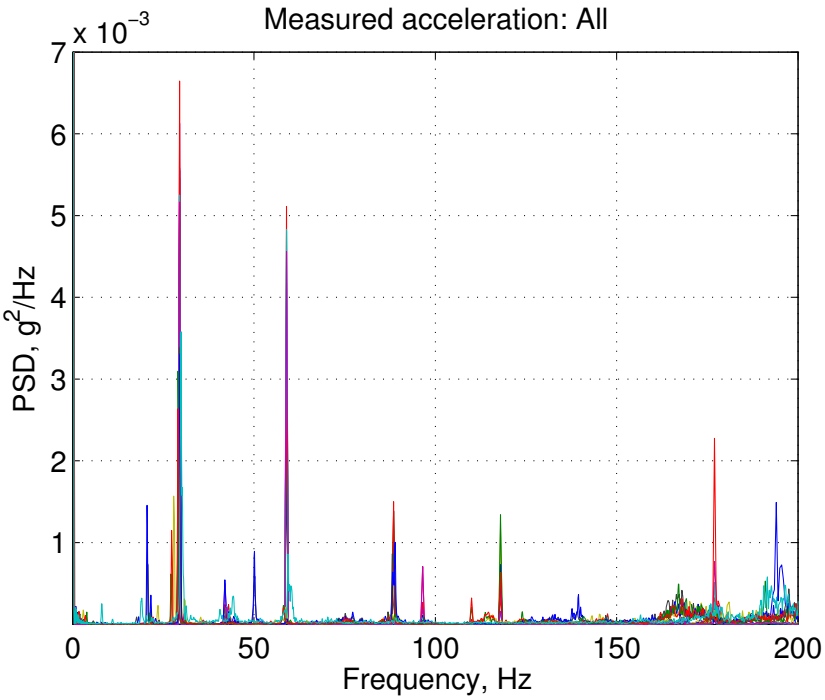

Figure A.7: All 18 measurements of compressor base at different points in time plotted on same graph.

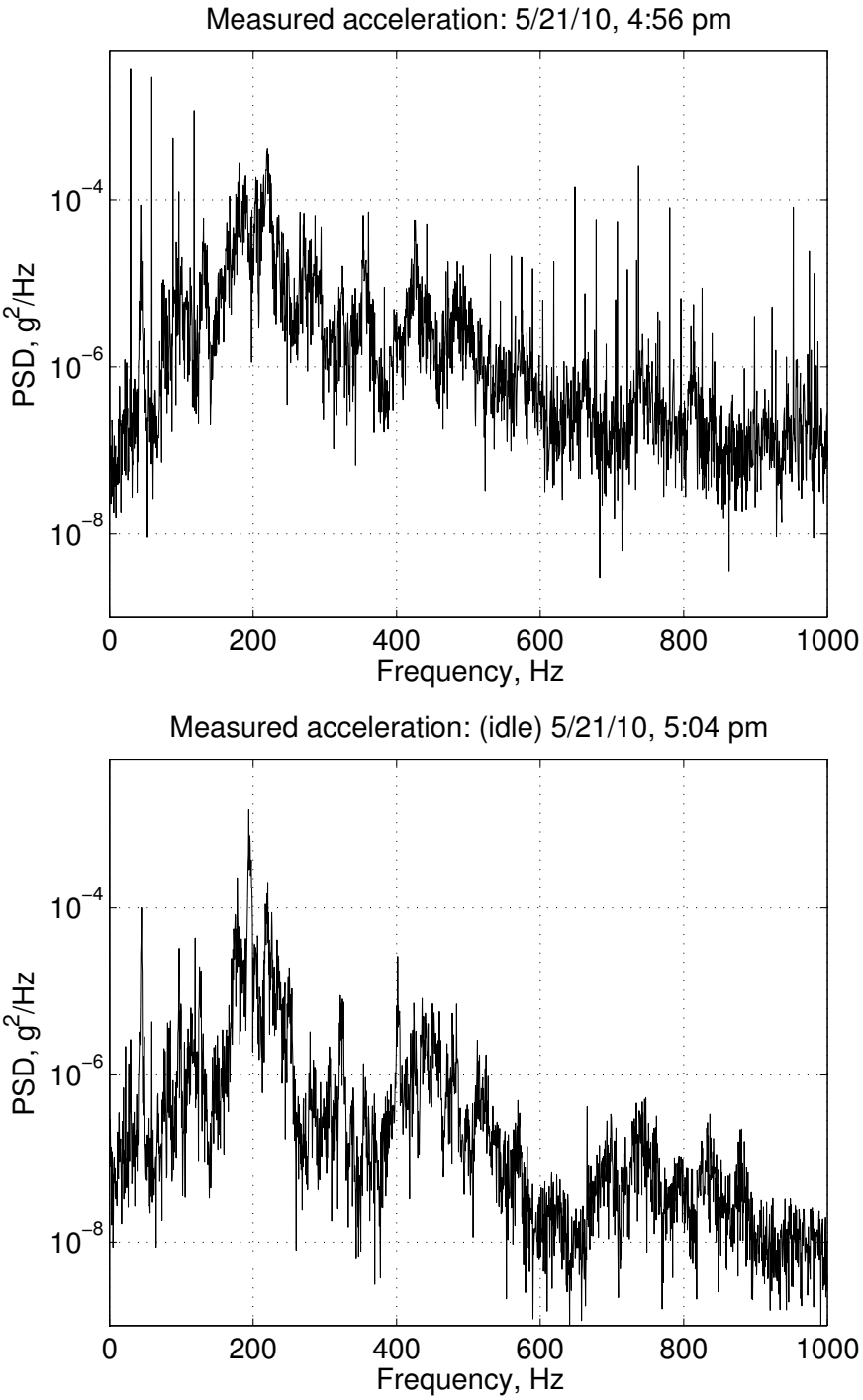

Figure A.8: These plots show the spectrum from 0 to 1000 Hz for the compressor base when the it is operating (top) and idling (bottom). Note the semi-log scale. These plots illustrate the variability of vibrations over time and that there are very few frequency peaks above 200 Hz, which is why the rest of the plots are on a scale of 0 to 200.

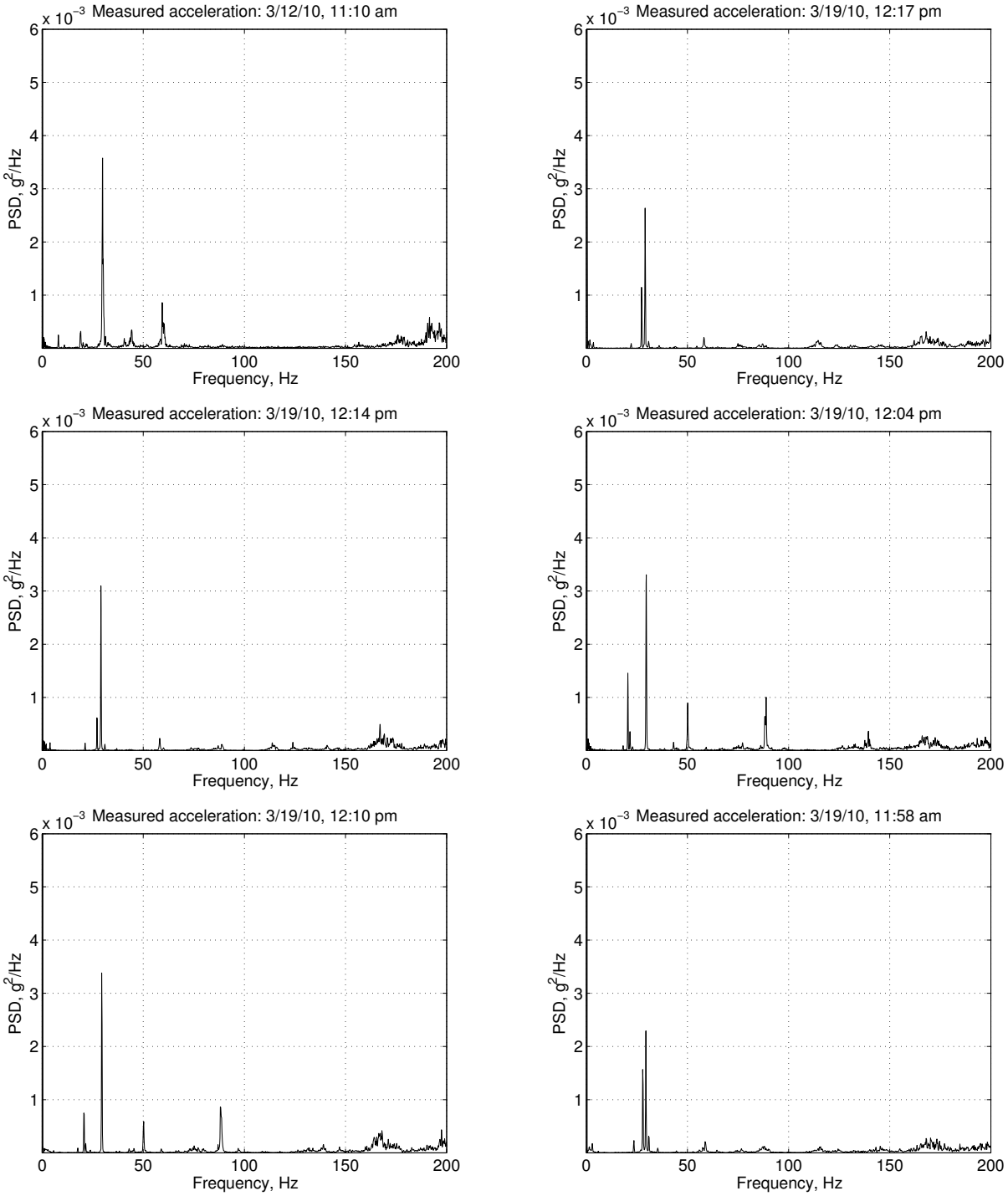

Figure A.9: Vibration spectra for the compressor base over time. Data for these figures was taken in March on two days one week apart. The exact date and time are given in the title. These plots are all on the same scale.

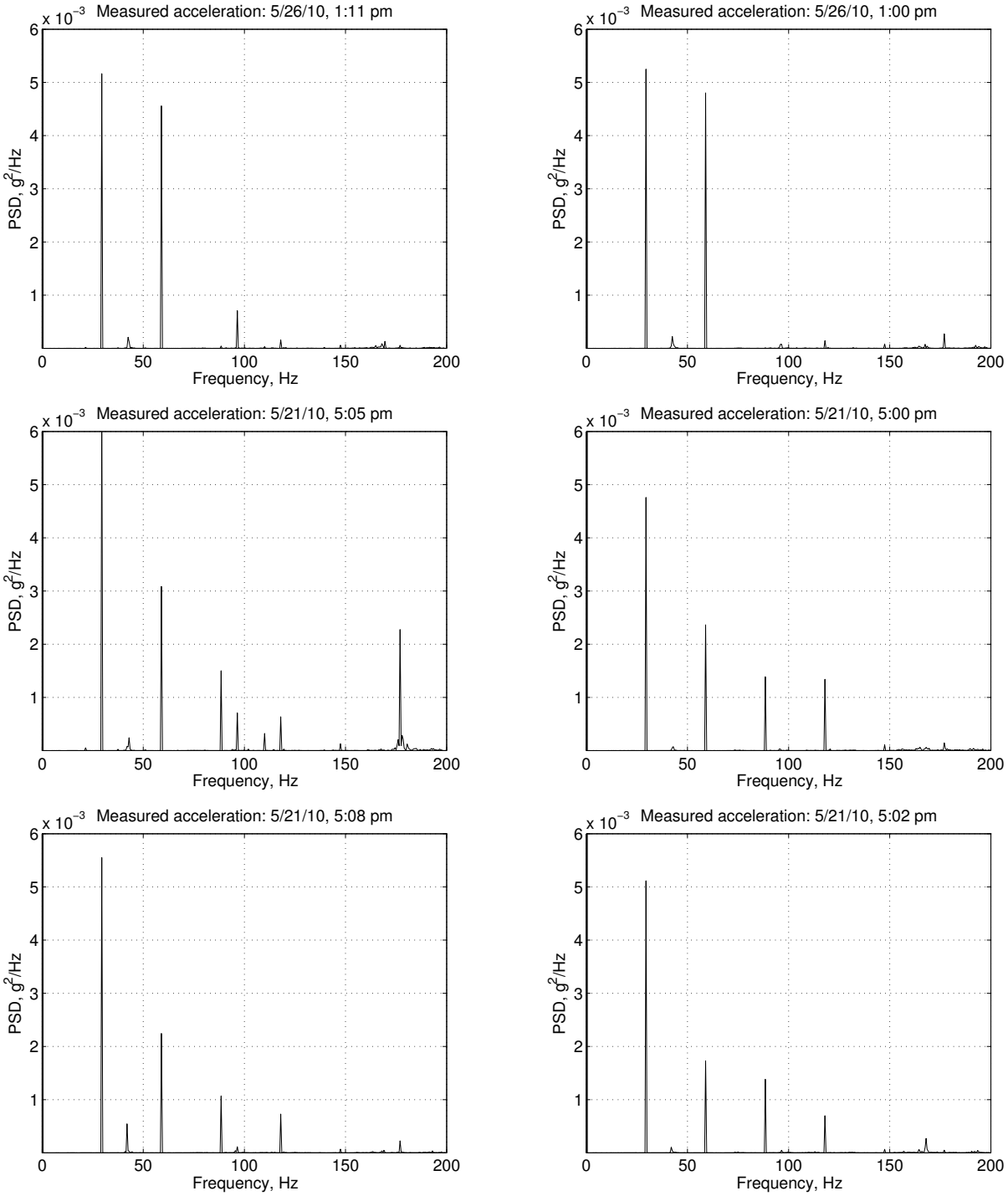

Figure A.10: Vibration spectra for the compressor base over time. Data for these figures was taken in May on two days several days apart. The exact date and time are given in the title. These plots are all on the same scale.

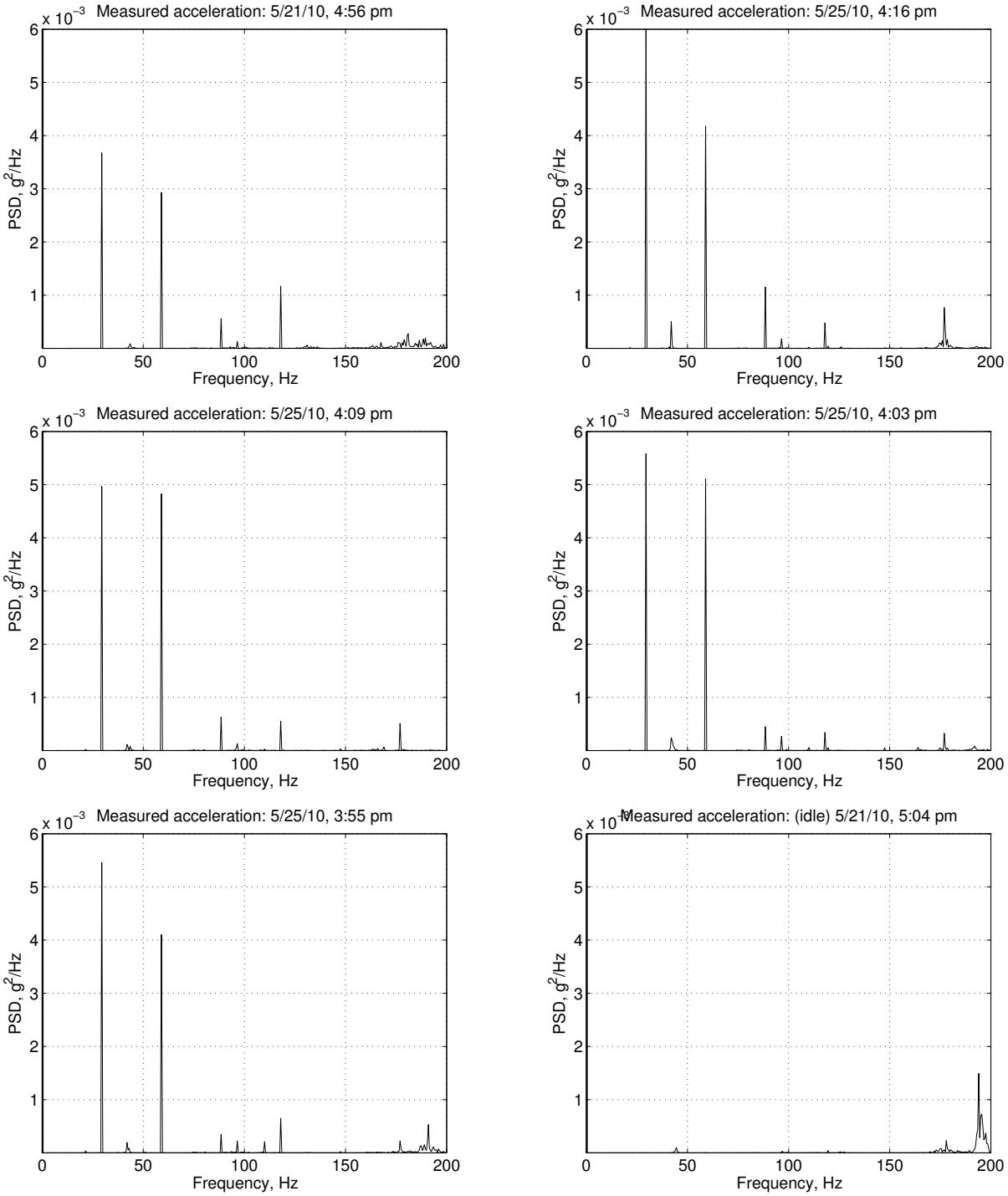

Figure A.11: Vibration spectra for the compressor base over time. Data for these figures was taken in May on two days several days apart. The exact date and time are given in the title. These plots are all on the same scale.

Appendix B

Modeling Details: Discretization Process

In chapters 2, 3, and 4, the goal was to measure real-world ambient vibrations, use that data to predict the behavior of an energy harvester, and finally compare the model's predicted behavior with the experimentally determined behavior of the harvester. In order to incorporate the ambient vibration data into the model, it was necessary to discretize the continuous differential equations of motion that describe beam behavior. The mathematical derivation for discretization of differential equations have been developed previously by other researchers. Although it is not the original work of this author, the derivation is presented in this appendix for the convenience of anyone in the energy harvesting field who may be interested in applying these methods to their models. The following closely follows the derivation given in [8].

Suppose there exists a linear time-invariant equation in the form of (B.1).

$$\dot{X}(t) = -AX(t) + B(t) \tag{B.1}$$

It is necessary to discretize this equation so that it can be used to model the behavior of a such a system subjected to a known initial state $X(t_0)$ and a known input excitation $B(t)$, where the input excitation is in the form of discrete data points. It is possible to use the property given in equation (B.2) to premultiply (B.1).

$$\frac{d}{dt}e^{At} = e^{At}A \tag{B.2}$$

Integrating and solving for $X(t_n)$ then yields equation (B.3). Equation (B.3) uses initial conditions to find the value of X at the first time step after $t = 0$. Equation (B.4) then uses that value of X to continue iterating until X has been computed for all data points.

$$X(t_n) = e^{-A(t_n - t_0)}X(t_0) + \int_{t_0}^{t_n} e^{-A(t_n - \tau)}B(\tau)d\tau \tag{B.3}$$

$$X(t_{n+1}) = e^{-A(t_{n+1}-t_n)}X(t_n) + \int_{t_n}^{t_{n+1}} e^{-A(t_{n+1}-\tau)}B(\tau)d\tau \tag{B.4}$$

It is reasonable to assume a constant time step, which will be called Δt, since the data is collected with a constant sampling frequency. Additionally, we can simplify the equations by defining U and B_n as in equations (B.5).

$$\Delta t = t_{n+1} - t_n, \qquad U = e^{-A\Delta \mathrm{t}}, \qquad B_n = B(\tau) \tag{B.5}$$

U is known since the elements of the matrix A are known and the time step Δt is known. Next, we approximate B_n linearly between data points, which is necessary because B_n is continuously integrated but the data is discrete. This can be expressed mathematically as in equation (B.7).

$$t \in [t_n, t_{n+1}] \tag{B.6}$$

$$B(t) = \frac{t_{n+1} - t}{\Delta t}B_n + \frac{t - t_n}{\Delta t}B_{n+1} \tag{B.7}$$

Substituting into equation (B.4) and expanding terms gives the following equation.

$$X_{n+1} = UX_n + \underbrace{\frac{B_n}{\Delta t}\int_{t_n}^{t_{n+1}} (t_{n+1} - \tau)\, e^{-A(t_{n+1}-\tau)}d\tau}_{M} + \underbrace{\frac{B_{n+1}}{\Delta t}\int_{t_n}^{t_{n+1}} (\tau - t_n)\, e^{-A(t_{n+1}-\tau)}d\tau}_{N} \tag{B.8}$$

Now it is necessary to evaluate the two integral terms in equation (B.8) so that values for X can be determined at the discrete steps dictated by the input data. The two integrals in question are defined as M and N and the integrals are simplified by redefining the time step as $\tau' = \Delta t - \tau$.

$$M = \frac{1}{\Delta t}\int_0^{\Delta t} \tau' e^{-A\tau'}d\tau', \qquad N = \frac{1}{\Delta t}\int_0^{\Delta t} \tau e^{-A(\Delta t-\tau)}d\tau \tag{B.9}$$

By substituting into equation (B.8), we can write X_{n+1} as

$$X_{n+1} = UX_n + MB_n + NB_{n+1} \tag{B.10}$$

However, M and N must still be evaluated. This can be achieved by first diagonalizing A and then solving for A so it is in terms of its eigenvector matrix, S, and eigenvalue matrix, Λ [61].

$$\Lambda = S^{-1}AS, \qquad A = S\Lambda S^{-1} \tag{B.11}$$

Similarly, if we diagonalize M, N, and A, we can write equations (B.9) as

$$S^{-1}MS = \frac{1}{\Delta t}\int_0^{\Delta t} \tau' e^{-\Lambda\tau'}d\tau', \quad S^{-1}NS = \frac{1}{\Delta t}\int_0^{\Delta t} \tau e^{-\Lambda(\Delta t-\tau)}d\tau \tag{B.12}$$

$$\mu_k = \frac{1}{\Delta t}\int_0^{\Delta t} \tau' e^{-\lambda_k \tau'} d\tau', \quad \eta_k = \frac{1}{\Delta t}\int_0^{\Delta t} \tau e^{-\lambda_k(\Delta t - \tau)} d\tau \tag{B.13}$$

Since A is a matrix with known values and λ_k are the eigenvalues of A, it is possible to integrate equation (B.13), resulting in

$$\mu_k = \frac{1}{\Delta t}\left[-\frac{e^{-\lambda_k \tau'}}{\lambda_k^2} - \frac{\tau' e^{-\lambda_k \tau'}}{\lambda_k}\right]_0^{\Delta t}, \qquad \eta_k = \frac{1}{\Delta t}\left[\frac{\tau e^{\lambda_k(\tau - \Delta t)}}{\lambda_k} - \frac{e^{\lambda_k(\tau - \Delta t)}}{\lambda_k^2}\right]_0^{\Delta t} \tag{B.14}$$

$$\mu_k = \frac{1}{\Delta t \lambda_k^2}\left(1 - e^{-\lambda_k \Delta t}\right) - \frac{1}{\lambda_k} e^{-\lambda_k \Delta k}, \qquad \eta_k = \frac{1}{\Delta t \lambda_k^2}\left(e^{-\lambda_k \Delta t} - 1\right) + \frac{1}{\lambda_k} \tag{B.15}$$

Finally, the three eigenvalues of A can be used to solve for the three μ components of the diagonalized M matrix.

$$M = S \begin{bmatrix} \mu_1 & 0 & 0 \\ 0 & \mu_2 & 0 \\ 0 & 0 & \mu_3 \end{bmatrix} S^{-1}, \qquad N = S \begin{bmatrix} \eta_1 & 0 & 0 \\ 0 & \eta_2 & 0 \\ 0 & 0 & \eta_3 \end{bmatrix} S^{-1} \tag{B.16}$$

Now, with expressions for M and N in terms of the eigenvector matrix, S, and μ_k and ν_k, which can all be calculated from the A matrix, it is possible to numerically solve equation (B.10). Employing MATLAB or another similar program, it is possible to numerically calculate X using, for example, the discrete experimentally determined acceleration data as the input excitation.

Appendix C

Modeling Details: Adaptable-Frequency Nonlinear Resonator

The derivation for the mathematical model of a sliding mass on a fixed-fixed beam was derived without much detail, for easier readability, in chapter 8. Here, a much more detailed derivation is shown. The same equations that appeared in chapter 8 are repeated here for convenience, but will be numbered differently. This derivation starts by presenting a brief summary of some background information that the reader may find useful for following the procedure.

C.1 Basics and background

Hamilton's principle:

$$S = \int_{t1}^{t2} dtL \tag{C.1}$$

where S is known as the action integral, and Hamilton's principle states that the physical solutions occur when

$$\delta S = \delta \int_{t1}^{t2} Ldt \equiv \delta \int_{t1}^{t2} (T - V)dt = 0 \tag{C.2}$$

is satisfied. The times, $t1$ and $t2$, are any arbitrary times as long as $t2$ is greater than $t1$. $\mathcal{L}$ is the Lagrangian, defined as kinetic energy minus potential energy, $T - V$.
Euler-Lagrange equation:

$$\frac{\partial \mathcal{L}}{\partial q_i} - \frac{d}{dt}\left(\frac{\partial \mathcal{L}}{\partial \dot{q}_i}\right) = 0 \tag{C.3}$$

where q_i is the function to be found. Properties of δ - variational operator:

$$\delta\phi = \bar{\phi}(x) - \phi(x) = \epsilon\eta(x), \qquad \epsilon \to 0 \tag{C.4}$$

where $\bar{\phi}(x)$ is infinitesimally different from $\phi(x)$.

1. The independent variable x does not participate in variation.

$$\delta x = 0 \tag{C.5}$$

2. Commutitive with respect to differentiation: the derivative of a variation and the variation of a derivative are the same thing:

$$\frac{d}{dx}\delta\phi = \frac{d}{dx}\epsilon\eta(x) = \epsilon\frac{d\eta(x)}{dx} \tag{C.6}$$

$$\delta\frac{d\phi}{dx} = \frac{d\bar{\phi}}{dx} - \frac{d\phi}{dx} = \frac{d}{dx}\left(\bar{\phi} - \phi\right) = \frac{d}{dx}\epsilon\eta(x) = \epsilon\frac{d\eta(x)}{dx} \tag{C.7}$$

3. Commutative with respect to integration: the integral of a variation and the variation of an integral are the same thing:

$$\delta\int_{x_1}^{x_2}\phi(x)dx = \int_{x_1}^{x_2}\bar{\phi}(x)dx - \int_{x_1}^{x_2}\phi(x)dx = \int_{x_1}^{x_2}[\bar{\phi}(x) - \phi(x)]dx = \int_{x_1}^{x_2}\delta\phi(x)dx$$

$$\int_{x_1}^{x_2}\delta\phi(x)dx = \delta\int_{x_1}^{x_2}\phi(x)dx \tag{C.8}$$

Useful general properties to recall:

1. Integration by parts:

$$\int_a^b f(x)g'(x)dx = f(x)g(x)|_a^b - \int_a^b f'(x)g(x)dx \tag{C.9}$$

2. Chain rule:

$$d(g(x)) = g'(x)dx \tag{C.10}$$

3. When $W = W(y(t), t)$ instead of $W = W(x, t)$:

$$\frac{d}{dt}\dot{W} = \ddot{W} + \dot{W}'\dot{Y} \tag{C.11}$$

$$\frac{d}{dt}W' = \dot{W}' + W''\dot{Y} \tag{C.12}$$

$$\frac{d}{dt}W'\dot{Y} = (\dot{W}' + W''\dot{Y})\dot{Y} + W'\ddot{Y} = \dot{W}'\dot{Y} + W''\dot{Y}^2 + W'\ddot{Y} \tag{C.13}$$

Remember that position can be a function of time, but time is not a function of position, so

$$\frac{d}{dY}\dot{W} = \dot{W}' \tag{C.14}$$

Properties related to Dirac delta:
Dirac delta is not the same as the derivative of the Dirac delta:

$$\begin{aligned} f(x)\delta(x-y) &= f(y)\delta(x-y) && \text{(C.15)}\\ f(x)\delta'(x-y) &\neq f(y)\delta'(x-y) && \text{(C.16)}\\ T(y)\delta'(x-y) &= \frac{d}{dx}[T(y)\delta(x-y)] && \text{(C.17)}\\ &= \frac{d}{dx}[T(x)\delta(x-y)] && \text{(C.18)}\\ &= T'(x)\delta(x-y) + T(x)\delta'(x-y) && \text{(C.19)}\\ &= T'(y)\delta(x-y) + T(x)\delta'(x-y) && \text{(C.20)} \end{aligned}$$

$$\frac{d}{dt}\delta(x-y(t)) = -\dot{y}(t)\delta'(x-y(t)) \tag{C.21}$$

The nondimensional form of $\delta(X-Y)$, assuming that $x = X/L$ and $y = Y/L$, is $L^{-1}\delta(x-y)$.
Useful matrix properties:
The singular value decomposition of a real matrix A is

$$A = U\Sigma V^T \tag{C.22}$$

where U and V are orthogonal matrices, meaning that $U^TU = I$ and $V^TV = I$, and Σ is a diagonal matrix with diagonal terms σ_1, σ_2, σ_n. We can rearrange to write

$$AV = U\Sigma \tag{C.23}$$

and if $V = [v_1 \quad v_2...v_n]$ and $U = [u_1 \quad u_2...u_n]$, we have

$$[Av_1 \quad Av_2...Av_n] = [\sigma_1 u_1 \quad \sigma_2 u_2...\sigma_n u_n] \tag{C.24}$$

Therefore, if $\sigma_k = 0$ for some k, then $Av_k = 0$. In MATLAB we can find the condition number of the matrix A (solved at various values of βL) to see where it goes to infinity. At those values of βL, which are the eigenfrequencies, we substitute into A. Then singular value decomposition can be used to get the coefficients of v_k.

C.2 Physical system definition

The system, shown in figure C.1, is defined as follows: input vibrations are described by $W_o(t)$. A point along the beam is denoted by the coordinate X, beam vertical position

is described by $W(X,t)$, mass horizontal position is $Y(t)$, and mass vertical position is $W(Y(t),t)$. Derivatives with respect to time are denoted with a dot and derivatives with respect to X are denoted with a prime. Derivatives with respect to $Y(t)$ are written out explicitly. The coordinate system is defined as x-axis along length of beam and z-axis in the direction of vertical displacement. The beam properties are defined by its bending stiffness,

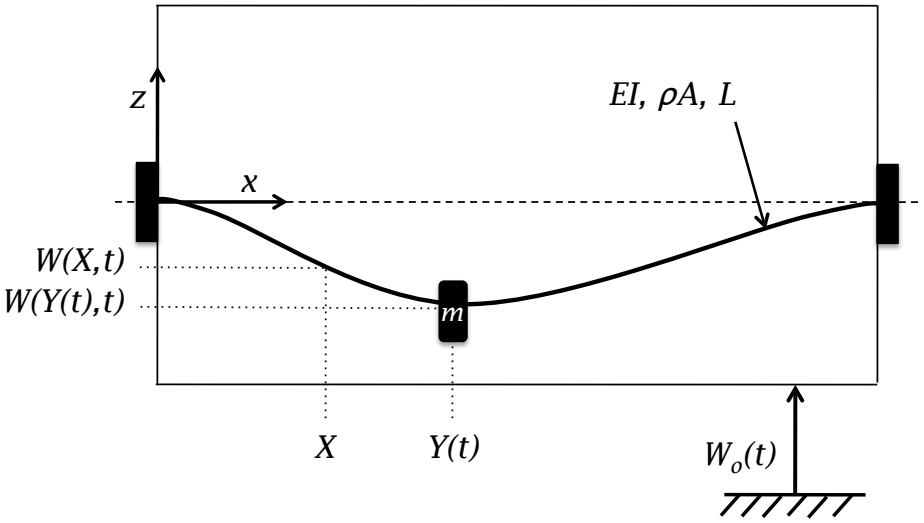

Figure C.1: Schematic of the spring-mass system. The fixed-fixed beam is secured to a reference frame which is subjected to input vibrations. Mass is free to slide along the beam.

EI, linear density, ρA, and length, L. Slope and angular rotation of the beam due to the mass are given, respectively, by

$$\theta = \left.\frac{\partial W}{\partial X}\right|_{X=Y(t)} = W'(Y(t),t) \tag{C.25}$$

$$\dot{\theta} = \frac{d}{dt}\left(\left.\frac{\partial W}{\partial X}\right|_{X=Y(t)}\right) = (W''\dot{Y} + \dot{W}')|_{X=Y(t)} \tag{C.26}$$

Similarly, the velocity of the mass due to constrained motion with the beam is found by taking the time derivative of the mass position, resulting in

$$\frac{d}{dt}\big(W_o(t) + W(Y(t),t)\big) = \dot{W}_o + \dot{W} + W'\dot{Y}. \tag{C.27}$$

C.3 Equations of motion

The kinetic energy of the beam and the sliding mass is

$$\begin{aligned} T &= \int_0^L \frac{1}{2}\rho A(\dot{W}_o + \dot{W})^2 dX \\ &\quad + \frac{1}{2}m\left[\dot{Y}^2 + (\dot{W}_o + \dot{W} + W'\dot{Y})^2\right]_{X=Y(t)} + \frac{1}{2}I_m\left[(W''\dot{Y} + \dot{W}')^2\right]_{X=Y(t)} \end{aligned} \quad \text{(C.28)}$$

where ρ is density of the beam, A is cross sectional area of the beam, L is length of the beam, m is the proof mass, and I_m is moment of inertia of the mass about the y-axis. The first term represents kinetic energy of the beam due to vertical motion, second term is kinetic energy of the mass due to horizontal motion along beam and kinetic energy of the mass due to vertical motion with beam, and the last term is kinetic energy of the mass due to rotation about the beam. Potential energy of the system is simply due to elastic deformation of the beam and is given by

$$V = \int_0^L \frac{1}{2}EI(W'')^2 dX \quad \text{(C.29)}$$

where E is the young's modulus of the beam and I is moment of inertia of the beam about the y-axis. The Lagrangian density $\mathcal{L}$ of the system, kinetic minus potential energy density, is

$$\begin{aligned} \mathcal{L} &= \frac{1}{2}\rho A(\dot{W}_o + \dot{W})^2 - \frac{1}{2}EI(W'')^2 \\ &\quad + \left\{\frac{1}{2}m\dot{Y}^2 + \frac{1}{2}m(\dot{W}_o + \dot{W} + W'\dot{Y})^2 + \frac{1}{2}I_m(W''\dot{Y} + \dot{W}')^2\right\}\delta(X - Y). \end{aligned} \quad \text{(C.30)}$$

The Euler-Lagrange equation for the beam can be derived from the variation of the action integral:

$$S = \int_{t1}^{t2} dtL = \int_{t1}^{t2} dt \int_0^l dX\mathcal{L}(\dot{W}, W', \dot{W}', W'') \quad \text{(C.31)}$$

$$\begin{aligned} \delta S &= \int_{t1}^{t2} dt \int_0^l dX\left(\frac{\partial\mathcal{L}}{\partial\dot{W}}\delta\dot{W} + \frac{\partial\mathcal{L}}{\partial W'}\delta W' + \frac{\partial\mathcal{L}}{\partial\dot{W}'}\delta\dot{W}' + \frac{\partial\mathcal{L}}{\partial W''}\delta W''\right) = 0 \\ &= \int_{t1}^{t2} dt \int_0^l dX\left(-\frac{d}{dt}\frac{\partial\mathcal{L}}{\partial\dot{W}}\delta W - \frac{d}{dX}\frac{\partial\mathcal{L}}{\partial W'}\delta W - \frac{d}{dt}\frac{\partial\mathcal{L}}{\partial\dot{W}'}\delta W' - \frac{d}{dX}\frac{\partial\mathcal{L}}{\partial W''}\delta W'\right) \\ &= \int_{t1}^{t2} dt \int_0^l dX\left(-\frac{d}{dt}\frac{\partial\mathcal{L}}{\partial\dot{W}} - \frac{d}{dX}\frac{\partial\mathcal{L}}{\partial W'} + \frac{d^2}{dtdX}\frac{\partial\mathcal{L}}{\partial\dot{W}'} + \frac{d^2}{dX^2}\frac{\partial\mathcal{L}}{\partial W''}\right)\delta W \end{aligned} \quad \text{(C.32)}$$

To satisfy the equation, the term in parentheses in equation (C.32) is set equal to zero, resulting in

$$-\frac{d}{dt}\frac{\partial\mathcal{L}}{\partial\dot{W}} - \frac{d}{dX}\frac{\partial\mathcal{L}}{\partial W'} + \frac{d^2}{dtdX}\frac{\partial\mathcal{L}}{\partial\dot{W}'} + \frac{d^2}{dX^2}\frac{\partial\mathcal{L}}{\partial W''} = 0 \quad \text{(C.33)}$$

which is the Euler-Lagrange equation for the beam, from which the beam equation of motion can be derived. The Euler-Lagrange equation for the mass is derived similarly, resulting in

$$\frac{\partial \mathcal{L}}{\partial Y} - \frac{d}{dt}\frac{\partial \mathcal{L}}{\partial \dot{Y}} = 0. \tag{C.34}$$

Starting with equation (C.30), we can take the following derivatives in order to write down the Euler-Lagrange equation for the mass.

$$\begin{aligned}
\frac{\partial \mathcal{L}}{\partial Y} &= m(\dot{W}_o + \dot{W} + W'\dot{Y})(\dot{W}' + W''\dot{Y}) \\
&+ I_m(\dot{W}' + W''\dot{Y})(\dot{W}'' + W'''\dot{Y}) && \text{(C.35)} \\
\frac{\partial \mathcal{L}}{\partial \dot{Y}} &= m\dot{Y} + m(\dot{W}_o + \dot{W} + W'\dot{Y})W' + I_m(\dot{W}' + W''\dot{Y})W'' && \text{(C.36)} \\
\frac{d}{dt}\frac{\partial \mathcal{L}}{\partial \dot{Y}} &= m\Big[\ddot{Y} + (\dot{W}_o + \dot{W} + W'\dot{Y})(\dot{W}' + W''\dot{Y}) \\
&+ (\ddot{W}_o + \ddot{W} + 2\dot{W}'\dot{Y} + W''\dot{Y}^2 + W'\ddot{Y})W'\Big] \\
&\quad + I_m\Big[(\dot{W}' + W''\dot{Y})(\dot{W}'' + W'''\dot{Y}) \\
&+ (\ddot{W}' + 2\dot{W}''\dot{Y} + W'''\dot{Y}^2 + W''\ddot{Y})W''\Big] && \text{(C.37)} \\
\frac{\partial \mathcal{L}}{\partial Y} - \frac{d}{dt}\frac{\partial \mathcal{L}}{\partial \dot{Y}} &= m\ddot{Y} + m(\ddot{W}_o + \ddot{W} + 2\dot{W}'\dot{Y} + W''\dot{Y}^2 + W'\ddot{Y})W' \\
&\quad + I_m(\ddot{W}' + 2\dot{W}''\dot{Y} + W'''\dot{Y}^2 + W''\ddot{Y})W'' = 0 && \text{(C.38)}
\end{aligned}$$

Again, starting with equation (C.30), we can take the following derivatives in order to

write down the Euler-Lagrange equation for the beam.

$$\frac{\partial \mathcal{L}}{\partial \dot{W}} = \rho A(\dot{W}_o + \dot{W}) + m(\dot{W}_o + \dot{W} + W'\dot{Y})\delta(X-Y) \tag{C.39}$$

$$\frac{\partial \mathcal{L}}{\partial W'} = m(\dot{W}_o + \dot{W} + W'\dot{Y})\dot{Y}\delta(X-Y) \tag{C.40}$$

$$\frac{\partial \mathcal{L}}{\partial \dot{W}'} = I_m(\dot{W}' + W''\dot{Y})\delta(X-Y) \tag{C.41}$$

$$\frac{\partial \mathcal{L}}{\partial W''} = I_m(\dot{W}' + W''\dot{Y})\dot{Y}\delta(X-Y) \tag{C.42}$$

$$\begin{aligned}\frac{d}{dt}\frac{\partial \mathcal{L}}{\partial \dot{W}} &= \rho A(\ddot{W}_o + \ddot{W}) + m(\ddot{W}_o + \ddot{W} + \dot{W}'\dot{Y} + W'\ddot{Y})\delta(X-Y) \\ &\quad -m(\dot{W}_o + \dot{W} + W'\dot{Y})\dot{Y}\delta'(X-Y)\end{aligned} \tag{C.43}$$

$$\frac{d}{dX}\frac{\partial \mathcal{L}}{\partial W'} = m(\dot{W}_o + \dot{W} + W'\dot{Y})\dot{Y}\delta'(X-Y) + m(\dot{W}' + W''\dot{Y})\dot{Y}\delta(X-Y) \tag{C.44}$$

$$\begin{aligned}\frac{d^2}{dXdt}\frac{\partial \mathcal{L}}{\partial \dot{W}'} &= \frac{d}{dX}\Big[- I_m(\dot{W}' + W''\dot{Y})\dot{Y}\delta'(X-Y) \\ &\quad +I_m(\ddot{W}' + \dot{W}''\dot{Y} + W''\ddot{Y})\delta(X-Y)\Big]\end{aligned} \tag{C.45}$$

$$\begin{aligned}\frac{d^2}{dX^2}\frac{\partial \mathcal{L}}{\partial W''} &= \frac{d}{dX}\Big[I_m(\dot{W}' + W''\dot{Y})\dot{Y}\delta'(X-Y) + I_m(\dot{W}'' + W'''\dot{Y})\dot{Y}\delta(X-Y) \\ &\quad -EIW'''\Big]\end{aligned} \tag{C.46}$$

Substituting into equations (C.33) and (C.34) results in the beam and mass equations of motion, respectively, as

$$\begin{aligned}0 &= \rho A(\ddot{W}_o + \ddot{W}) + m(\ddot{W}_o + \ddot{W} + 2\dot{W}'\dot{Y} + W''\dot{Y}^2 + W'\ddot{Y})\delta(X-Y) + EIW'''' \\ &- \frac{d}{dX}\Big[I_m(\ddot{W}' + 2\dot{W}''\dot{Y} + W'''\dot{Y}^2 + W''\ddot{Y})\delta(X-Y)\Big]\end{aligned} \tag{C.47}$$

$$\begin{aligned}0 &= m\ddot{Y} + m(\ddot{W}_o + \ddot{W} + 2\dot{W}'\dot{Y} + W''\dot{Y}^2 + W'\ddot{Y})W' \\ &\quad +I_m(\ddot{W}' + 2\dot{W}''\dot{Y} + W'''\dot{Y}^2 + W''\ddot{Y})W''.\end{aligned} \tag{C.48}$$

This result can be interpreted as a beam driven by a uniform load, a point force F and a point torque T, where F and T are defined as

$$F = -m(\ddot{W}_o + \ddot{W} + 2\dot{W}'\dot{Y} + W''\dot{Y}^2 + W'\ddot{Y}) \tag{C.49}$$

$$T = -I_m(\ddot{W}' + 2\dot{W}''\dot{Y} + W'''\dot{Y}^2 + W''\ddot{Y}) \tag{C.50}$$

so equations (C.48) and (C.47) can be rewritten as

$$\rho A(\ddot{W}_o + \ddot{W}) + EIW'''' = F\delta(X-Y) - T\delta'(X-Y) \tag{C.51}$$

$$m\ddot{Y} = FW'(Y,t) + TW''(Y,t) \tag{C.52}$$

The equations of motion are nondimensionalized by introducing the following nondimensional time, frequency, and displacements for the system, closely following the notation used by Miranda *et al* [45]:

$$\tau = \tilde{\omega}_1 t, \quad \Omega = \frac{\omega}{\tilde{\omega}_1}, \quad w_o = \frac{W_o}{L}, \quad w = \frac{W}{L}, \quad x = \frac{X}{L}, \quad y = \frac{Y}{L}, \tag{C.53}$$

where τ is nondimensional time, $\tilde{\omega}_1$ is the fundamental frequency of the beam with no mass present, Ω is nondimensional frequency, and for displacements the lowercase letters represent nondimensional versions of the uppercase letters. Derivatives that exist in the equations of motion are nondimensionalized as follows (these are written out for the variable, W, but the same form applies to nondimensionalizing the time and space derivatives of Y and W_o).

$$\frac{dW}{dt} = \frac{d(wL)}{d\tau}\frac{d\tau}{dt} = L\tilde{\omega}_1\frac{dw}{d\tau} \tag{C.54}$$

$$\frac{d^2W}{dt^2} = \frac{d^2(wL)}{d\tau^2}\frac{d^2\tau}{dt^2} = L\tilde{\omega}_1^2\frac{d^2w}{d\tau^2} \tag{C.55}$$

$$\frac{dW}{dX} = \frac{d(wL)}{dx}\frac{dx}{dX} = L\frac{1}{L}\frac{dw}{dx} = \frac{dw}{dx} \tag{C.56}$$

$$\frac{d^2W}{dX^2} = \frac{d^2(wL)}{dx^2}\frac{d^2x}{dX^2} = L\frac{1}{L^2}\frac{d^2w}{dx^2} = \frac{1}{L}\frac{d^2w}{dx^2} \tag{C.57}$$

$$\frac{d^2W}{dtdX} = \frac{d^2(wL)}{d\tau dx}\frac{d\tau}{dt}\frac{dx}{dX} = \tilde{\omega}_1\frac{d^2w}{d\tau dx} \tag{C.58}$$

$$\frac{d^3W}{dXdt^2} = \frac{d^3(wL)}{dxd\tau^2}\frac{d^2\tau}{dt^2}\frac{dx}{dX} = \tilde{\omega}_1^2\frac{d^3w}{dxd\tau^2} \tag{C.59}$$

$$\frac{d^3W}{dX^2dt} = \frac{d^3(wL)}{dx^2d\tau}\frac{d\tau}{dt}\frac{d^2x}{dX^2} = \frac{\tilde{\omega}_1}{L}\frac{d^3w}{dx^2d\tau} \tag{C.60}$$

$$\frac{d^3W}{dX^3} = \frac{d^3(wL)}{dx^3}\frac{d^3x}{dX^3} = \frac{1}{L^2}\frac{d^3w}{dx^3} \tag{C.61}$$

$$\frac{d^4W}{dX^4} = \frac{d^4(wL)}{dx^4}\frac{d^4x}{dX^4} = \frac{1}{L^3}\frac{d^4w}{dx^4} \tag{C.62}$$

Substituting the nondimensional terms into equations (C.47) and (C.48), dividing the mass equation by $mL\tilde{\omega}_1^2$ and the beam equation by $\rho AL\tilde{\omega}_1^2$, and then adding terms for damping and friction results in the nondimensional equations of motion,

$$\begin{aligned} 0 = {} & \ddot{y} + c_m\dot{y} + (\ddot{w}_o + \ddot{w} + 2\dot{w}'\dot{y} + w''\dot{y}^2 + w'\ddot{y})w' \\ & + \chi(\ddot{w}' + 2\dot{w}''\dot{y} + w'''\dot{y}^2 + w''\ddot{y})w'' \\ & + \mu\Big[(\ddot{w}_o + \ddot{w} + 2\dot{w}'\dot{y} + w''\dot{y}^2 + w'\ddot{y} + \bar{g})\text{sgn}\ (\dot{y} + w'(\dot{w}_o + \dot{w} + w'\dot{y}))\Big] \end{aligned} \tag{C.63}$$

$$\begin{aligned} 0 = {} & (\ddot{w}_o + \ddot{w}) + c_b(\dot{w}_o + \dot{w}) + \alpha(\ddot{w}_o + \ddot{w} + 2\dot{w}'\dot{y} + w''\dot{y}^2 + w'\ddot{y})\delta(x-y) \\ & + \nu w'''' - \gamma\frac{d}{dx}\Big[(\ddot{w}' + 2\dot{w}''\dot{y} + w'''\dot{y}^2 + w''\ddot{y})\delta(x-y)\Big] \end{aligned} \tag{C.64}$$

with dimensionless parameters defined as

$$\alpha = \frac{m}{\rho AL}, \quad \nu = \frac{EI}{\rho AL^4\tilde{\omega}_1^2}, \quad \gamma = \frac{I_m}{\rho AL^2}, \quad \chi = \frac{I_m}{mL^2} \tag{C.65}$$

$$c_m = \frac{C_m}{m\tilde{\omega}_1}, \quad c_b = \frac{C_b}{\rho AL\tilde{\omega}_1}, \quad \bar{g} = \frac{g}{L\tilde{\omega}_1^2} \tag{C.66}$$

where α is a nondimensional mass, ν is nondimensional stiffness, γ and χ are nondimensional rotational moment of inertia of the proof mass relative to the beam inertia and the mass inertia respectively, c_m and c_b are linear viscous damping of the mass motion and beam motion respectively, $\bar{g}$ is nondimensional gravity, and μ is dry friction of mass sliding.

C.4 Eigenfunctions and boundary conditions

To obtain the expression for the beam shape as a function of time, we start with the homogenous case of equation (C.64), where $w_o = 0$. Neglecting damping but including rotational inertia of the mass, as well as assuming that mass is considered fixed because it moves on a much slower timescale than the beam, we have

$$0 = \ddot{w} + \alpha\ddot{w}\delta(x-y) + \nu w'''' - \gamma\ddot{w}'(y,\tau)\delta'(x-y) \tag{C.67}$$

which can also be written, with a different representation of the last term, as

$$0 = \ddot{w} + \alpha\ddot{w}\delta(x-y) + \nu w'''' - \gamma\frac{d}{dx}\Big[\delta(x-y)\ddot{w}'(x,\tau)\Big]. \tag{C.68}$$

Using separation of variables, we introduce

$$w(x,\tau) = u(x)T(\tau). \tag{C.69}$$

If we substitute this into equation (C.68), rearrange, divide through by ν, and substitute $\ddot{T}(\tau)/T(\tau) = -\Omega^2$, we arrive at

$$u''''(x) - \frac{1+\alpha\delta(x-y)}{\nu}u(x)\Omega^2 + \frac{\gamma}{\nu}\frac{d}{dx}\Big[\delta(x-y)u'(x)\Big]\Omega^2 = 0. \tag{C.70}$$

We can rearrange equation (C.70) to give

$$u''''(x) = \frac{\Omega^2}{\nu}\left\{[1+\alpha\delta(x-y)]u(x) - \gamma\frac{d}{dx}\big[\delta(x-y)u'(x)\big]\right\} \tag{C.71}$$

where we can now define two linear operators

$$\hat{K} = \frac{d^4}{dx^4}, \quad \hat{M} = 1 + \alpha\delta(x-y) - \gamma\frac{d}{dx}\delta(x-y)\frac{d}{dx}. \tag{C.72}$$

Note that the operations in the last term of M should be done in order from right to left. Substituting into equation (C.71) gives

$$\hat{K}u_n(x) = \beta_n^4 \hat{M}u_n(x), \quad \text{where} \quad \beta_n^4 = \frac{\Omega_n^2}{\nu}. \tag{C.73}$$

The solution to equation (C.73) is of the form

$$\begin{aligned} u_{L,n}(x) &= A_{L,n}\cos\beta_n x + B_{L,n}\sin\beta_n x + C_{L,n}\cosh\beta_n x + D_{L,n}\sinh\beta_n x, \quad x < y \\ u_{R,n}(x) &= A_{R,n}\cos\beta_n(1-x) + B_{R,n}\sin\beta_n(1-x) \\ &\quad + C_{R,n}\cosh\beta_n(1-x) + D_{R,n}\sinh\beta_n(1-x), \quad x > y. \end{aligned} \tag{C.74}$$

The eight unknown coefficients in these equations must be found using eight boundary conditions. The first four boundary conditions are given by the fact that the beam has fixed-fixed end conditions, so the deflection and slope at both ends of the beam, $x = 0$ and $x = 1$, must be zero. This is written as

$$u(0) = u(1) = 0, \quad u'(0) = u'(1) = 0. \tag{C.75}$$

Additionally, there are four boundary conditions that come from continuity requirements. Those are found by the following procedure, recalling that θ is the Heaviside function, where $\theta(x-y) = 0$ if $x < y$ but $\theta(x-y) = 1$ if $x > y$. Also, the derivative of the Heaviside function is the Dirac delta.

$$u_n(x) = \theta(x-y)u_{R,n}(x) + \theta(y-x)u_{L,n}(x) \tag{C.76}$$

$$u_n'(x) = \delta(x-y)\big[u_{R,n}(y) - u_{L,n}(y)\big] + \theta(x-y)u_{R,n}'(x) + \theta(y-x)u_{L,n}'(x) \tag{C.77}$$

Equation (C.70) has no δ''' terms, so the δ term must drop out of equation (C.77). To ensure this, the expression in brackets must equal zero, giving the fifth boundary condition. Taking the second and third derivatives of $u_n(x)$ leads to

$$u_n''(x) = \delta(x-y)\big[u_{R,n}'(y) - u_{L,n}'(y)\big] + \theta(x-y)u_{R,n}''(x) + \theta(y-x)u_{L,n}''(x) \tag{C.78}$$

$$u_n'''(x) = \delta(x-y)\big[u_{R,n}''(y) - u_{L,n}''(y)\big] + \theta(x-y)u_{R,n}'''(x) + \theta(y-x)u_{L,n}'''(x) \tag{C.79}$$

where the terms inside the brackets in equation (C.78) also must equal zero since there are no δ'' terms in equation (C.70), thus giving a sixth boundary condition. However, the term inside the brackets in equation (C.79) must not equal zero since there is a δ' in the equation (C.70). Therefore, the fourth derivative of $u_n(x)$ is

$$u_n''''(x) = \delta(x-y)\big[u_{R,n}'''(y) - u_{L,n}'''(y)\big] \tag{C.80}$$

$$+ \quad \delta'(x-y)\big[u_{R,n}''(y) - u_{L,n}''(y)\big]$$

$$+ \quad \theta(x-y)u_{R,n}''''(x) + \theta(y-x)u_{L,n}''''(x). \tag{C.81}$$

The final two boundary conditions are found by equating the coefficients of the various derivatives of δ. Recalling the original beam equation, (C.70), and multiplying (C.81) by ν gives

$$\begin{aligned}
\nu u''''(x) = &\quad \nu\delta(x-y)\big[u'''_{R,n}(y) - u'''_{L,n}(y)\big] \\
+ &\quad \nu\delta'(x-y)\big[u''_{R,n}(y) - u''_{L,n}(y)\big] \\
+ &\quad \nu\theta(x-y)u''''_{R,n}(x) + \nu\theta(y-x)u''''_{L,n}(x) \qquad \text{(C.82)} \\
\nu u''''(x) = &\quad \Omega^2(1+\alpha\delta(x-y))u_n(x) - \Omega^2\gamma\delta'(x-y)u'_n(y) \qquad \text{(C.83)}
\end{aligned}$$

from which boundary conditions 7 and 8 are found to be, respectively,

$$\begin{aligned}
\nu\big[u''_{R,n}(y) - u''_{L,n}(y)\big] &= -\Omega^2\gamma u'_n(y) \qquad \text{(C.84)} \\
\nu\big[u'''_{R,n}(y) - u'''_{L,n}(y)\big] &= \Omega^2\alpha u_n(x) \qquad \text{(C.85)}
\end{aligned}$$

To summarize, the eight boundary conditions are

$$\begin{aligned}
&1) \quad u(0) = 0 \\
&2) \quad u(1) = 0 \\
&3) \quad u'(0) = 0 \\
&4) \quad u'(1) = 0 \\
&5) \quad u_{R,n}(y) - u_{L,n}(y) = 0 \\
&6) \quad u'_{R,n}(y) - u'_{L,n}(y) = 0 \\
&7) \quad u''_{R,n}(y) - u''_{L,n}(y) = -\frac{\Omega_n^2\gamma}{\nu}u'_n(y) \\
&8) \quad u'''_{R,n}(y) - u'''_{L,n}(y) = \frac{\Omega_n^2\alpha}{\nu}u_n(y). \qquad \text{(C.86)}
\end{aligned}$$

Applying boundary conditions 1-4 to equation (C.70) shows that $A_{L,n} = -C_{L,n}$, $B_{L,n} = -D_{L,n}$, $A_{R,n} = -C_{R,n}$ and $B_{R,n} = -D_{R,n}$, leaving

$$\begin{aligned}
u_{L,n}(x) &= A_{L,n}(\cos\beta_n x - \cosh\beta_n x) + D_{L,n}(\sin\beta_n x - \sinh\beta_n x) \qquad \text{(C.87)} \\
u_{R,n}(x) &= A_{R,n}(\cos\beta_n(1-x) - \cosh\beta_n(1-x)) \\
&+ D_{R,n}(\sin\beta_n(1-x) - \sinh\beta_n(1-x)) \qquad \text{(C.88)}
\end{aligned}$$

The first, second, and third derivatives of $u_n(x)$ can then be computed and substituted into boundary conditions 5-8, yielding four expressions with four unknowns for each mode ($A_{L,n}$, $D_{L,n}$, $A_{R,n}$, and $D_{R,n}$), so the beam shape can be determined when the mass is fixed in a given position. These last four boundary conditions produce, respectively, the following

equations:

$$\begin{aligned}
0 &= A_{R,n}(\cos\beta_n(1-y)-\cosh\beta_n(1-y))+D_{R,n}(\sin\beta_n(1-y)-\sinh\beta_n(1-y)) \\
&\quad -A_{L,n}(\cos\beta_n y-\cosh\beta_n y)-D_{L,n}(\sin\beta_n y-\sinh\beta_n y) \qquad \text{(C.89)} \\
0 &= A_{R,n}(-\sin\beta_n(1-y)-\sinh\beta_n(1-y))+D_{R,n}(\cos\beta_n(1-y)-\cosh\beta_n(1-y)) \\
&\quad +A_{L,n}(-\sin\beta_n y-\sinh\beta_n y)+D_{L,n}(\cos\beta_n y-\cosh\beta_n y) \qquad \text{(C.90)} \\
0 &= A_{R,n}(-\cos\beta_n(1-y)-\cosh\beta_n(1-y))+D_{R,n}(-\sin\beta_n(1-y)-\sinh\beta_n(1-y)) \\
&\quad +A_{L,n}\Big[-\beta_n^3\gamma(\sin\beta_n y+\sinh\beta_n y)+(\cos\beta_n y+\cosh\beta_n y)\Big] \\
&\quad +D_{L,n}\Big[-\beta_n^3\gamma(-\cos\beta_n y+\cosh\beta_n y)+(\sin\beta_n y+\sinh\beta_n y)\Big] \qquad \text{(C.91)} \\
0 &= A_{R,n}(\sin\beta_n(1-y)-\sinh\beta_n(1-y))+D_{R,n}(-\cos\beta_n(1-y)-\cosh\beta_n(1-y)) \\
&\quad -A_{L,n}\Big[-\beta_n\alpha(\cos\beta_n y-\cosh\beta_n y)-(\sin\beta_n y-\sinh\beta_n y)\Big] \\
&\quad -D_{L,n}\Big[-\beta_n\alpha(\sin\beta_n y-\sinh\beta_n y)-(-\cos\beta_n y-\cosh\beta_n y)\Big] \qquad \text{(C.92)}
\end{aligned}$$

The first, second, and third derivatives of $u_n(x)$ can now be computed and substituted into boundary conditions 5-8. This yields four expressions with five unknowns for each mode (β_n, $A_{L,n}$, $D_{L,n}$, $A_{R,n}$, and $D_{R,n}$). This system is solved numerically in MATLAB by assuming one mass position at a time, assuming a vector of input "guesses" for the value of β_n, and then solving the system of four equations and four unknowns for each value of β_n guess. The condition number of the matrix of coefficients ($A_{L,n}$, $D_{L,n}$, $A_{R,n}$, and $D_{R,n}$ for each boundary condition) is then plotted as a function of β_n. The values of β_n that result in the condition number spiking to a very large value (meaning that the coefficient matrix is singular) indicate nontrivial solutions. These β_n solutions are then inserted into the four equations and four unknowns to find the values for $A_{L,n}$, $D_{L,n}$, $A_{R,n}$, and $D_{R,n}$ for the desired number of modes. Two modes were calculated in this study, and singular value decomposition method was used to solve the system.

With all coefficients now known, the beam shape can be calculated for the mass fixed in a given position. Before using the beam shape expressions in computation they need to be normalized, as will be described in the next section. Going forward, w_n refers to the full beam shape solution including segments of the beam both left and right, $u_{L,n}$ and $u_{R,n}$, of the position of the proof mass. Finally, the fundamental frequency of the beam with no mass present, $\tilde{\omega}_1$, is needed in order to nondimensionalize the system of equations according to the parameters defined in equations (C.53), (C.65), and (C.66). To find this frequency, the characteristic equation of the fixed-fixed beam with no mass,

$$\cos\lambda_n\cosh\lambda_n = 1, \qquad \text{(C.93)}$$

is solved numerically for the eigenvalues, λ_n, from which frequency can be calculated using $\tilde{\omega}_1^2 = EI\lambda_1^4/\rho AL^4$.

C.5 Normalization

We need to normalize $w_n(x, y(\tau))$. The procedure given here to find the expression for the normalization coefficients follows [49], but this material is in nearly any vibrations book. Recall that $w_n(x, y(\tau)) = C_n[u_{Ln}(x) \quad u_{Rn}(x)]$ and

$$\begin{aligned} u_{L,n}(x) &= A_{L,n}(\cos\beta_n x - \cosh\beta_n x) + D_{L,n}(\sin\beta_n x - \sinh\beta_n x) \qquad \text{(C.94)} \\ u_{R,n}(x) &= A_{R,n}(\cos\beta_n(1-x) - \cosh\beta_n(1-x)) + D_{R,n}(\sin\beta_n(1-x) - \sinh\beta_n(1-x)). \end{aligned}$$

The generalized eigenvalue problem for two modes, i and j, is

$$\begin{aligned} \hat{K}u_n &= \lambda_n\hat{M}u_n \qquad \text{(C.95)} \\ \hat{K}u_m &= \lambda_m\hat{M}u_m, \qquad \text{(C.96)} \end{aligned}$$

as was shown in equation (C.73). Multiplying (C.95) from the left by u_m and (C.96) from the left by u_n, then subtracting the two equations and integrating over the length of the beam gives

$$\int_0^1 (u_m\hat{K}u_n - u_n\hat{K}u_m)dx = \int_0^1 (\lambda_n u_m\hat{M}u_n - \lambda_m u_n\hat{M}u_m)dx. \qquad \text{(C.97)}$$

Assuming the eigenvalue problem is self adjoint, which will not be proven here but can be found in, for example, [49], the following equalities can be stated.

$$\int_0^1 u_m\hat{K}u_n dx = \int_0^1 u_n\hat{K}u_m dx \qquad \text{(C.98)}$$

$$\int_0^1 u_m\hat{M}u_n dx = \int_0^1 u_n\hat{M}u_m dx \qquad \text{(C.99)}$$

Substituting equations (C.98) and (C.99) into (C.97) results in

$$(\lambda_n - \lambda_m)\int_0^1 u_m\hat{M}u_n dx = 0. \qquad \text{(C.100)}$$

From equation (C.100) it is clear that if m and n are not equal,

$$\int_0^1 u_m\hat{M}u_n dx = 0 \quad \text{and} \quad \int_0^1 u_m\hat{K}u_n dx = 0. \qquad \text{(C.101)}$$

Equations (C.101) are the generalized orthogonality conditions. Following from equation (C.100), if m and n are equal the equation is satisfied by the fact that $\lambda_n - \lambda_m = 0$. Then the u_n's can be normalized with respect to $\hat{M}u_n$ by setting

$$\int_0^1 (C_n u_n)\hat{M}(C_n u_n)dx = C_n^2 \int_0^1 u_n \hat{M} u_n dx = 1, \quad n = 1, 2, ... \tag{C.102}$$

where C_n is the normalization coefficient. This can be summarized as

$$C_n^2 \int_0^1 u_m \hat{M} u_n dx = \delta_{mn} \tag{C.103}$$

where $\delta_{mn} = 1$ if $m = n$, but $\delta_{mn} = 0$ if $m \neq n$. Therefore, after writing out the actions of the $\hat{M}$ operator on u_n when $m = n$, normalizing with respect to 1, and solving for C_n, the normalization coefficient for the problem at hand is

$$C_n = \left(\left[\int_0^y u_{Ln}^2(x,y)dx + \int_y^1 u_{Rn}^2(x,y)dx \right] + \alpha(u_{L,n}(y))^2 + \gamma(u'_{L,n}(y))^2 \right)^{-\frac{1}{2}}. \tag{C.104}$$

Going through the algebra to obtain the expression for the integrand in the denominator of equation (C.104) gives

$$\begin{aligned}
u_{Ln}^2(x) &= A_{Ln}^2 \cos^2\beta_n x + A_{Ln}^2 \cosh^2\beta_n x + D_{Ln}^2 \sin^2\beta_n x + D_{Ln}^2 \sinh^2\beta_n x \\
&- 2A_{Ln}^2 \cos\beta_n x \cosh\beta_n x - 2D_{Ln}^2 \sin\beta_n x \sinh\beta_n x \\
&- 2A_{Ln}D_{Ln} \cos\beta_n x \sinh\beta_n x - 2A_{Ln}D_{Ln} \cosh\beta_n x \sin\beta_n x \\
&+ 2A_{Ln}D_{Ln} \cosh\beta_n x \sinh\beta_n x + 2A_{Ln}D_{Ln} \cos\beta_n x \sin\beta_n x
\end{aligned} \tag{C.105}$$

$$\begin{aligned}
u_{Rn}^2(x) &= A_{Rn}^2 \cos^2\beta_n(1-x) + A_{Rn}^2 \cosh^2\beta_n(1-x) \\
&+ D_{Rn}^2 \sin^2\beta_n(1-x) + D_{Rn}^2 \sinh^2\beta_n(1-x) \\
&- 2A_{Rn}^2 \cos\beta_n(1-x) \cosh\beta_n(1-x) - 2D_{Rn}^2 \sin\beta_n(1-x) \sinh\beta_n(1-x) \\
&- 2A_{Rn}D_{Rn} \cos\beta_n(1-x) \sinh\beta_n(1-x) - 2A_{Rn}D_{Rn} \cosh\beta_n(1-x) \sin\beta_n(1-x) \\
&+ 2A_{Rn}D_{Rn} \cosh\beta_n(1-x) \sinh\beta_n(1-x) + 2A_{Rn}D_{Rn} \cos\beta_n(1-x) \sin\beta_n(1-x).
\end{aligned} \tag{C.106}$$

u_{Ln}^2 and u_{Rn}^2 are then integrated from 0 to y and y to 1, respectively, and the integral term in equation (C.104) is

$$\begin{aligned}
&\left[\int_0^y u_{Ln}^2(x,y)dx + \int_y^1 u_{Rn}^2(x,y)dx \right] = \\
&A_{Ln}^2 T11_n + D_{Ln}^2 T22_n + A_{Ln}D_{Ln} T12_n + A_{Rn}^2 T33_n + D_{Rn}^2 T44_n + A_{Rn}D_{Rn} T34_n
\end{aligned} \tag{C.107}$$

where the T_n terms are defined as

$$\begin{aligned}
T11_n &= \frac{1}{\beta_n}\left(\beta_n y + \frac{1}{4}\sin 2\beta_n y + \frac{1}{4}\sinh 2\beta_n y - \cos\beta_n y \sinh\beta_n y - \sin\beta_n y\cosh\beta_n y\right)\\
T12_n &= T21_n = \frac{1}{\beta_n}\left(\sinh^2\beta_n y + \sin^2\beta_n y - 2\sin\beta_n y\sinh\beta_n y\right)\\
T22_n &= \frac{1}{\beta_n}\left(\frac{1}{4}\sinh 2\beta_n y - \frac{1}{4}\sin 2\beta_n y - \sin\beta_n y\cosh\beta_n y + \cos\beta_n y\sinh\beta_n y\right)\\
T33_n &= \frac{1}{\beta_n}\Big(\beta_n(1-y) + \frac{1}{4}\sin 2\beta_n(1-y) + \frac{1}{4}\sinh 2\beta_n(1-y)\\
&\quad - \cos\beta_n(1-y)\sinh\beta_n(1-y) - \sin\beta_n(1-y)\cosh\beta_n(1-y)\Big)\\
T34_n &= T43_n = \frac{1}{\beta_n}\left(\sinh^2\beta_n(y-1) + \sin^2\beta_n(y-1) - 2\sin\beta_n(1-y)\sinh\beta_n(1-y)\right)\\
T44_n &= \frac{1}{\beta_n}\Big(\frac{1}{4}\sinh 2\beta_n(1-y) - \frac{1}{4}\sin 2\beta_n(1-y) - \sin\beta_n(1-y)\cosh\beta_n(1-y)\\
&\quad + \cos\beta_n(1-y)\sinh\beta_n(1-y)\Big).
\end{aligned} \tag{C.108}$$

The C_n values for a given value of mass position y can now be calculated, since u_n and u_n' are already known, and the beam shape, $w_n(x, y(\tau))$, can be normalized. When $w_n'(x, y(\tau))$, $w_n''(x, y(\tau))$, or $w_n'''(x, y(\tau))$ need to be computed, the normalization coefficient found here is used to compute the derivatives. Note that C_n is regarded as a constant if taking the derivative of w with respect to x, but is not a constant if taking derivative with respect to y.

C.6 Fixed-mass eigenmode expansion

We now solve the equations of motion that were derived in the previous sections using eigenmode expansion. If $w_n(x, y, \tau)$ is the solution of (C.68) corresponding to the natural frequency ω_n, we write

$$w(x, \tau) = \sum_{n=0}^{\infty} \eta_n(\tau) w_n(x, y, \tau) \tag{C.109}$$

and insert into equations (C.63) and (C.64), multiply from the left by $w_m(x, y)$ and integrate over x. In these w_n terms, $y = y(\tau)$, but will be written at simply y for ease. Similarly, all integrals are evaluated from 0 to 1 (the nondimensional length of the beam). Also, note that w, w_n, w_m, and ω_n are all distinct variables. This leads to the beam equation expressed as

$$
\begin{aligned}
0 \;=\; & \int w_m(x,y)\ddot{w}_o dx + \int w_m(x,y)\alpha\ddot{w}_o\delta(x-y)dx + \int w_m(x,y)c_b\dot{w}_o dx \qquad \text{(C.110)} \\
& + \int w_m(x,y)\Bigg[\sum_{n=0}^{\infty}\ddot{\eta}_n(\tau)w_n(x,y) + 2\sum_{n=0}^{\infty}\dot{\eta}_n(\tau)\dot{y}\frac{\partial w_n(x,y)}{\partial y} \\
& \qquad + \sum_{n=0}^{\infty}\eta_n(\tau)\ddot{y}\frac{\partial w_n(x,y)}{\partial y} + \sum_{n=0}^{\infty}\eta_n(\tau)\dot{y}^2\frac{\partial^2 w_n(x,y)}{\partial y^2}\Bigg]dx \\
& + \int w_m(x,y)c_b\Bigg[\sum_{n=0}^{\infty}\dot{\eta}_n(\tau)w_n(x,y) + \sum_{n=0}^{\infty}\eta_n(\tau)\dot{y}\frac{\partial w_n(x,y)}{\partial y}\Bigg]dx \\
& + \int w_m(x,y)\alpha\Bigg[\sum_{n=0}^{\infty}\ddot{\eta}_n(\tau)w_n(x,y) + 2\sum_{n=0}^{\infty}\dot{\eta}_n(\tau)\dot{y}\frac{\partial w_n(x,y)}{\partial y} \\
& \qquad + \sum_{n=0}^{\infty}\eta_n(\tau)\ddot{y}\frac{\partial w_n(x,y)}{\partial y} + \sum_{n=0}^{\infty}\eta_n(\tau)\dot{y}^2\frac{\partial^2 w_n(x,y)}{\partial y^2}\Bigg]\delta(x-y)dx \quad ...
\end{aligned}
$$

$$
\begin{aligned}
\ldots \quad & + \int w_m(x,y) 2\alpha \left[\sum_{n=0}^{\infty} \dot{\eta}_n(\tau) \dot{y} w_n'(x,y) + \sum_{n=0}^{\infty} \eta_n(\tau) \dot{y}^2 \frac{\partial w_n'(x,y)}{\partial y} \right] \delta(x-y) dx \\
& + \int w_m(x,y) \nu \sum_{n=0}^{\infty} \eta_n(\tau) w_n''''(x,y) dx \\
& - \int w_m(x,y) \gamma \left[\sum_{n=0}^{\infty} \ddot{\eta}_n(\tau) w_n''(x,y) + 2 \sum_{n=0}^{\infty} \dot{\eta}_n(\tau) \dot{y} \frac{\partial w_n''(x,y)}{\partial y} \right. \\
& \qquad \left. + \sum_{n=0}^{\infty} \eta_n(\tau) \ddot{y} \frac{\partial w_n''(x,y)}{\partial y} + \sum_{n=0}^{\infty} \eta_n(\tau) \dot{y}^2 \frac{\partial^2 w_n''(x,y)}{\partial y^2} \right] \delta(x-y) dx \\
& - \int w_m(x,y) \gamma \left[\sum_{n=0}^{\infty} \ddot{\eta}_n(\tau) w_n'(x,y) + 2 \sum_{n=0}^{\infty} \dot{\eta}_n(\tau) \dot{y} \frac{\partial w_n'(x,y)}{\partial y} \right. \\
& \qquad \left. + \sum_{n=0}^{\infty} \eta_n(\tau) \ddot{y} \frac{\partial w_n'(x,y)}{\partial y} + \sum_{n=0}^{\infty} \eta_n(\tau) \dot{y}^2 \frac{\partial^2 w_n'(x,y)}{\partial y^2} \right] \delta'(x-y) dx \\
& - \int w_m(x,y) 2\gamma \left[\sum_{n=0}^{\infty} \dot{\eta}_n(\tau) \dot{y} w_n'''(x,y) + \sum_{n=0}^{\infty} \eta_n(\tau) \dot{y}^2 \frac{\partial w_n'''(x,y)}{\partial y} \right] \delta(x-y) dx \\
& - \int w_m(x,y) 2\gamma \left[\sum_{n=0}^{\infty} \dot{\eta}_n(\tau) \dot{y} w_n''(x,y) + \sum_{n=0}^{\infty} \eta_n(\tau) \dot{y}^2 \frac{\partial w_n''(x,y)}{\partial y} \right] \delta'(x-y) dx \\
& + \int w_m(x,y) \alpha \dot{y}^2 \sum_{n=0}^{\infty} \eta_n(\tau) w_n''(x,y) \delta(x-y) dx \\
& + \int w_m(x,y) \alpha \ddot{y} \sum_{n=0}^{\infty} \eta_n(\tau) w_n'(x,y) \delta(x-y) dx \\
& - \int w_m(x,y) \gamma \dot{y}^2 \sum_{n=0}^{\infty} \eta_n(\tau) w_n''''(x,y) \delta(x-y) dx \\
& - \int w_m(x,y) \gamma \dot{y}^2 \sum_{n=0}^{\infty} \eta_n(\tau) w_n'''(x,y) \delta'(x-y) dx \\
& - \int w_m(x,y) \gamma \ddot{y} \sum_{n=0}^{\infty} \eta_n(\tau) w_n'''(x,y) \delta(x-y) dx \\
& - \int w_m(x,y) \gamma \ddot{y} \sum_{n=0}^{\infty} \eta_n(\tau) w_n''(x,y) \delta'(x-y) dx.
\end{aligned}
$$

The beam equation simplifies to

$$
\begin{aligned}
0 \;=\;& \ddot{w}_o \int w_m(x,y)dx + \alpha\ddot{w}_o w_m(y,y) + c_b\dot{w}_o \int w_m(x,y)dx \qquad \text{(C.111)}\\
&+\sum_{n=0}^{\infty}\delta_{mn}\ddot{\eta}_n(\tau) + 2\dot{y}\int w_m(x,y)\sum_{n=0}^{\infty}\dot{\eta}_n(\tau)\frac{\partial w_n(x,y)}{\partial y}dx\\
&\quad +\ddot{y}\int w_m(x,y)\sum_{n=0}^{\infty}\eta_n(\tau)\frac{\partial w_n(x,y)}{\partial y}dx + \dot{y}^2\int w_m(x,y)\sum_{n=0}^{\infty}\eta_n(\tau)\frac{\partial^2 w_n(x,y)}{\partial y^2}dx\\
&+\sum_{n=0}^{\infty}c_b\delta_{mn}\dot{\eta}_n(\tau) + \int w_m(x,y)c_b\sum_{n=0}^{\infty}\eta_n(\tau)\dot{y}\frac{\partial w_n(x,y)}{\partial y}dx\\
&+\alpha\Bigg[\sum_{n=0}^{\infty}\ddot{\eta}_n(\tau)w_m(y,y)w_n(y,y) + 2\dot{y}\sum_{n=0}^{\infty}\dot{\eta}_n(\tau)w_m(y,y)\frac{\partial w_n(x,y)}{\partial y}\Bigg|_y\\
&\quad +\ddot{y}\sum_{n=0}^{\infty}\eta_n(\tau)w_m(y,y)\frac{\partial w_n(x,y)}{\partial y}\Bigg|_y + \dot{y}^2\sum_{n=0}^{\infty}\eta_n(\tau)w_m(y,y)\frac{\partial^2 w_n(x,y)}{\partial y^2}\Bigg|_y\Bigg]\\
&+2\alpha\Bigg[\sum_{n=0}^{\infty}\dot{\eta}_n(\tau)\dot{y}w_m(y,y)w_n'(y,y) + \sum_{n=0}^{\infty}\eta_n(\tau)\dot{y}^2 w_m(y,y)\frac{\partial w_n'(x,y)}{\partial y}\Bigg|_y\Bigg]\\
&+\nu\sum_{n=0}^{\infty}\beta_n^4\delta_{mn}\eta_n(\tau) - \gamma\Bigg[\sum_{n=0}^{\infty}\ddot{\eta}_n(\tau)w_m(y,y)w_n''(y,y) + 2\dot{y}\sum_{n=0}^{\infty}\dot{\eta}_n(\tau)w_m(y,y)\frac{\partial w_n''(x,y)}{\partial y}\Bigg|_y\\
&\quad +\ddot{y}\sum_{n=0}^{\infty}\eta_n(\tau)w_m(y,y)\frac{\partial w_n''(x,y)}{\partial y}\Bigg|_y + \dot{y}^2\sum_{n=0}^{\infty}\eta_n(\tau)w_m(y,y)\frac{\partial^2 w_n''(x,y)}{\partial y^2}\Bigg|_y\Bigg]\\
&+\gamma\Bigg[\sum_{n=0}^{\infty}\ddot{\eta}_n(\tau)w_m'(y,y)w_n''(y,y) + 2\dot{y}\sum_{n=0}^{\infty}\dot{\eta}_n(\tau)w_m'(y,y)\frac{\partial w_n''(x,y)}{\partial y}\Bigg|_y\\
&\quad +\ddot{y}\sum_{n=0}^{\infty}\eta_n(\tau)w_m'(y,y)\frac{\partial w_n''(x,y)}{\partial y}\Bigg|_y + \dot{y}^2\sum_{n=0}^{\infty}\eta_n(\tau)w_m'(y,y)\frac{\partial^2 w_n''(x,y)}{\partial y^2}\Bigg|_y\Bigg]\\
&-2\gamma\Bigg[\sum_{n=0}^{\infty}\dot{\eta}_n(\tau)\dot{y}w_m(y,y)w_n'''(y,y) + \sum_{n=0}^{\infty}\eta_n(\tau)\dot{y}^2 w_m(y,y)\frac{\partial w_n'''(x,y)}{\partial y}\Bigg|_y\Bigg]\\
&+2\gamma\Bigg[\sum_{n=0}^{\infty}\dot{\eta}_n(\tau)\dot{y}w_m'(y,y)w_n'''(y,y) + \sum_{n=0}^{\infty}\eta_n(\tau)\dot{y}^2 w_m'(y,y)\frac{\partial w_n'''(x,y)}{\partial y}\Bigg|_y\Bigg]\\
&+w_m(y,y)\alpha\dot{y}^2\sum_{n=0}^{\infty}\eta_n(\tau)w_n''(y,y) + w_m(y,y)\alpha\ddot{y}\sum_{n=0}^{\infty}\eta_n(\tau)w_n'(y,y)\\
&-w_m(y,y)\gamma\dot{y}^2\sum_{n=0}^{\infty}\eta_n(\tau)w_n''''(y,y) + w_m'(y,y)\gamma\dot{y}^2\sum_{n=0}^{\infty}\eta_n(\tau)w_n''''(y,y)\\
&-w_m(y,y)\gamma\ddot{y}\sum_{n=0}^{\infty}\eta_n(\tau)w_n'''(y,y) + w_m'(y,y)\gamma\ddot{y}\sum_{n=0}^{\infty}\eta_n(\tau)w_n'''(y,y).
\end{aligned}
$$

Similarly, the unsimplified mass expression is as follows.

$$
\begin{aligned}
0 \;=\;& \ddot{w}_o \sum_{n=0}^{\infty} \eta_n(\tau) w_n'(y,y) + \mu(\ddot{w}_o + \bar{g})\mathrm{sgn}\big(\,*\,\big) + \dot{y}c_m + \ddot{y} \\
&+ \Bigg[\sum_{n=0}^{\infty} \ddot{\eta}_n(\tau) w_n(y,y) + 2\sum_{n=0}^{\infty} \dot{\eta}_n(\tau)\dot{y}\frac{\partial w_n(y,y)}{\partial y} \\
&\quad + \sum_{n=0}^{\infty} \eta_n(\tau)\ddot{y}\frac{\partial w_n(y,y)}{\partial y} + \sum_{n=0}^{\infty} \eta_n(\tau)\dot{y}^2\frac{\partial^2 w_n(y,y)}{\partial y^2} \Bigg] \sum_{n=0}^{\infty} \eta_n(\tau) w_n'(y,y) \\
&+ \chi \Bigg[\sum_{n=0}^{\infty} \ddot{\eta}_n(\tau) w_n'(y,y) + 2\sum_{n=0}^{\infty} \dot{\eta}_n(\tau)\dot{y}\frac{\partial w_n'(y,y)}{\partial y} \\
&\quad + \sum_{n=0}^{\infty} \eta_n(\tau)\ddot{y}\frac{\partial w_n'(y,y)}{\partial y} + \sum_{n=0}^{\infty} \eta_n(\tau)\dot{y}^2\frac{\partial^2 w_n'(y,y)}{\partial y^2} \Bigg] \sum_{n=0}^{\infty} \eta_n(\tau) w_n''(y,y) \\
&+ \mu \Bigg[\sum_{n=0}^{\infty} \ddot{\eta}_n(\tau) w_n(y,y) + 2\sum_{n=0}^{\infty} \dot{\eta}_n(\tau)\dot{y}\frac{\partial w_n(y,y)}{\partial y} \\
&\quad + \sum_{n=0}^{\infty} \eta_n(\tau)\ddot{y}\frac{\partial w_n(y,y)}{\partial y} + \sum_{n=0}^{\infty} \eta_n(\tau)\dot{y}^2\frac{\partial^2 w_n(y,y)}{\partial y^2} \Bigg] \mathrm{sgn}\big(\,*\,\big) \Bigg] \\
&+ 2\dot{y} \Bigg[\sum_{n=0}^{\infty} \dot{\eta}_n(\tau) w_n'(x,y) + \sum_{n=0}^{\infty} \eta_n(\tau)\dot{y}\frac{\partial w_n'(x,y)}{\partial y} \Bigg] \sum_{n=0}^{\infty} \eta_n(\tau) w_n'(x,y) \\
&+ \dot{y}^2 \sum_{n=0}^{\infty} \eta_n(\tau) w_n''(x,y) \sum_{n=0}^{\infty} \eta_n(\tau) w_n'(x,y) + \ddot{y} \sum_{n=0}^{\infty} \eta_n(\tau) w_n'(x,y) \sum_{n=0}^{\infty} \eta_n(\tau) w_n'(x,y) \\
&+ 2\chi\dot{y} \Bigg[\sum_{n=0}^{\infty} \dot{\eta}_n(\tau) w_n''(x,y) + \sum_{n=0}^{\infty} \eta_n(\tau)\dot{y}\frac{\partial w_n''(x,y)}{\partial y} \Bigg] \sum_{n=0}^{\infty} \eta_n(\tau) w_n''(x,y) \\
&+ \chi\dot{y}^2 \sum_{n=0}^{\infty} \eta_n(\tau) w_n'''(x,y) \sum_{n=0}^{\infty} \eta_n(\tau) w_n''(x,y) + \chi\ddot{y} \sum_{n=0}^{\infty} \eta_n(\tau) w_n''(x,y) \sum_{n=0}^{\infty} \eta_n(\tau) w_n''(x,y) \\
&+ 2\mu\dot{y} \Bigg[\sum_{n=0}^{\infty} \dot{\eta}_n(\tau) w_n'(x,y) + \sum_{n=0}^{\infty} \eta_n(\tau)\dot{y}\frac{\partial w_n'(x,y)}{\partial y} \Bigg] \mathrm{sgn}\big(\,*\,\big) \\
&+ \mu\dot{y}^2 \sum_{n=0}^{\infty} \eta_n(\tau) w_n''(x,y)\mathrm{sgn}\big(\,*\,\big) + \mu\ddot{y} \sum_{n=0}^{\infty} \eta_n(\tau) w_n'(x,y)\mathrm{sgn}\big(\,*\,\big).
\end{aligned}
\tag{C.112}
$$

where,

$$
* = \dot{y} + \Bigg[\dot{w}_o + \sum_{n=0}^{\infty} \dot{\eta}_n(\tau) w_n(y,y) + \sum_{n=0}^{\infty} \eta_n(\tau)\dot{y}\frac{\partial w_n(y,y)}{\partial y} + \sum_{n=0}^{\infty} \eta_n(\tau)\dot{y} w_n'(y,y) \Bigg] \sum_{n=0}^{\infty} \eta_n(\tau) w_n'(y,y)
\tag{C.113}
$$

Performing these operations for the beam equation and expanding for $n = 0, 1$ and $m = 0, 1$ yields a set of equations which can be expressed in matrix form as

$$\begin{bmatrix} A_0 & B_0 \\ A_1 & B_1 \end{bmatrix} \begin{bmatrix} \ddot{\eta}_0 \\ \ddot{\eta}_1 \end{bmatrix} + \begin{bmatrix} C_0 & D_0 \\ C_1 & D_1 \end{bmatrix} \begin{bmatrix} \dot{\eta}_0 \\ \dot{\eta}_1 \end{bmatrix} + \begin{bmatrix} E_0 & F_0 \\ E_1 & F_1 \end{bmatrix} \begin{bmatrix} \eta_0 \\ \eta_1 \end{bmatrix} = \begin{bmatrix} Q_0 \\ Q_1 \end{bmatrix} \tag{C.114}$$

where, for $m = 0$,

$$\begin{aligned}
Q_0 &= -\ddot{w}_o \int_0^1 w_0(x,y)dx - \alpha \ddot{w}_o w_0(y,y) - c_b \dot{w}_o \int_0^1 w_0(x,y)dx \qquad \text{(C.115)} \\
A_0 &= 1 \\
B_0 &= 0 \\
C_0 &= c_b + 2\dot{y}\Bigg(\alpha w_0(y,y) w_0'(y,y) - \gamma w_0(y,y) w_0'''(y,y) + \gamma w_0'(y,y) w_0'''(y,y) \\
&\quad + \alpha w_0(y,y) \frac{\partial w_0(y,y)}{\partial y} - \gamma w_0(y,y) \frac{\partial w_0''(y,y)}{\partial y} + \gamma w_0'(y,y) \frac{\partial w_0''(y,y)}{\partial y} \\
&\quad + \int_0^1 w_0(x,y) \frac{\partial w_0(x,y)}{\partial y} dx \Bigg) \\
D_0 &= 2\dot{y}\Bigg(\alpha w_0(y,y) w_1'(y,y) - \gamma w_0(y,y) w_1'''(y,y) + \gamma w_0'(y,y) w_1'''(y,y) \\
&\quad + \alpha w_0(y,y) \frac{\partial w_1(y,y)}{\partial y} - \gamma w_0(y,y) \frac{\partial w_1''(y,y)}{\partial y} + \gamma w_0'(y,y) \frac{\partial w_1''(y,y)}{\partial y} \\
&\quad + \int_0^1 w_0(x,y) \frac{\partial w_1(x,y)}{\partial y} dx \Bigg)
\end{aligned}$$

$$
\begin{aligned}
E_0 \;=\;& \nu\beta_0^4 + \ddot{y}\alpha w_0(y,y)\frac{\partial w_0(y,y)}{\partial y} + \dot{y}^2 2\alpha w_0(y,y)\frac{\partial w_0'(y,y)}{\partial y} - \ddot{y}\gamma w_0(y,y)\frac{\partial w_0''(y,y)}{\partial y} \\
&+\ddot{y}\gamma w_0'(y,y)\frac{\partial w_0''(y,y)}{\partial y} - \dot{y}^2 2\gamma w_0(y,y)\frac{\partial w_0'''(y,y)}{\partial y} + \dot{y}^2 2\gamma w_0'(y,y)\frac{\partial w_0'''(y,y)}{\partial y} \\
&+\ddot{y}\int_0^1 w_0(x,y)\frac{\partial w_0(x,y)}{\partial y}dx + c_b\dot{y}\int_0^1 w_0(x,y)\frac{\partial w_0(x,y)}{\partial y}dx \\
&+\dot{y}^2\Bigg(\alpha w_0(y,y)\frac{\partial^2 w_0(y,y)}{\partial y^2} - \gamma w_0(y,y)\frac{\partial^2 w_0''(y,y)}{\partial y^2} + \gamma w_0'(y,y)\frac{\partial^2 w_0''(y,y)}{\partial y^2} \\
&+\int_0^1 w_0(x,y)\frac{\partial^2 w_0(x,y)}{\partial y^2}dx\Bigg) \\
&+\dot{y}^2\Big(\alpha w_0(y,y)w_0''(y,y) - \gamma w_0(y,y)w_0''''(y,y) + \gamma w_0'(y,y)w_0''''(y,y)\Big) \\
&+\ddot{y}\Big(\alpha w_0(y,y)w_0'(y,y) - \gamma w_0(y,y)w_0'''(y,y) + \gamma w_0'(y,y)w_0'''(y,y)\Big) \\
F_0 \;=\;& \ddot{y}\alpha w_0(y,y)\frac{\partial w_1(y,y)}{\partial y} + \dot{y}^2 2\alpha w_0(y,y)\frac{\partial w_1'(y,y)}{\partial y} - \ddot{y}\gamma w_0(y,y)\frac{\partial w_1''(y,y)}{\partial y} \\
&+\ddot{y}\gamma w_0'(y,y)\frac{\partial w_1''(y,y)}{\partial y} - \dot{y}^2 2\gamma w_0(y,y)\frac{\partial w_1'''(y,y)}{\partial y} + \dot{y}^2 2\gamma w_0'(y,y)\frac{\partial w_1'''(y,y)}{\partial y} \\
&+\ddot{y}\int_0^1 w_0(x,y)\frac{\partial w_1(x,y)}{\partial y}dx + c_b\dot{y}\int_0^1 w_0(x,y)\frac{\partial w_1(x,y)}{\partial y}dx \\
&+\dot{y}^2\Bigg(\alpha w_0(y,y)\frac{\partial^2 w_1(y,y)}{\partial y^2} - \gamma w_0(y,y)\frac{\partial^2 w_1''(y,y)}{\partial y^2} + \gamma w_0'(y,y)\frac{\partial^2 w_1''(y,y)}{\partial y^2} \\
&+\int_0^1 w_0(x,y)\frac{\partial^2 w_1(x,y)}{\partial y^2}dx\Bigg) \\
&+\dot{y}^2\Big(\alpha w_0(y,y)w_1''(y,y) - \gamma w_0(y,y)w_1''''(y,y) + \gamma w_0'(y,y)w_1''''(y,y)\Big) \\
&+\ddot{y}\Big(\alpha w_0(y,y)w_1'(y,y) - \gamma w_0(y,y)w_1'''(y,y) + \gamma w_0'(y,y)w_1'''(y,y)\Big)
\end{aligned}
$$

The terms for $m = 1$ follow the same form as for $m = 0$ and are and the terms for m = 1 in the beam equation are

$$
\begin{aligned}
Q_1 &= -\ddot{w}_o \int_0^1 w_1(x,y)dx - \alpha\ddot{w}_o w_1(y,y) - c_b\dot{w}_o \int_0^1 w_1(x,y)dx \qquad \text{(C.116)}\\
A_1 &= 0\\
B_1 &= 1\\
C_1 &= 2\dot{y}\Bigg(\alpha w_1(y,y)w_0'(y,y) - \gamma w_1(y,y)w_0'''(y,y) + \gamma w_1'(y,y)w_0'''(y,y)\\
&\quad +\alpha w_1(y,y)\frac{\partial w_0(y,y)}{\partial y} - \gamma w_1(y,y)\frac{\partial w_0''(y,y)}{\partial y} + \gamma w_1'(y,y)\frac{\partial w_0''(y,y)}{\partial y}\\
&\quad + \int_0^1 w_1(x,y)\frac{\partial w_0(x,y)}{\partial y}dx\Bigg)\\
D_1 &= c_b + 2\dot{y}\Bigg(\alpha w_1(y,y)w_1'(y,y) - \gamma w_1(y,y)w_1'''(y,y) + \gamma w_1'(y,y)w_1'''(y,y)\\
&\quad +\alpha w_1(y,y)\frac{\partial w_1(y,y)}{\partial y} - \gamma w_1(y,y)\frac{\partial w_1''(y,y)}{\partial y} + \gamma w_1'(y,y)\frac{\partial w_1''(y,y)}{\partial y}\\
&\quad + \int_0^1 w_1(x,y)\frac{\partial w_1(x,y)}{\partial y}dx\Bigg)
\end{aligned}
$$

$$
\begin{aligned}
E_1 &= \ddot{y}\alpha w_1(y,y)\frac{\partial w_0(y,y)}{\partial y} + \dot{y}^2 2\alpha w_1(y,y)\frac{\partial w_0'(y,y)}{\partial y} - \ddot{y}\gamma w_1(y,y)\frac{\partial w_0''(y,y)}{\partial y} \\
&\quad + \ddot{y}\gamma w_1'(y,y)\frac{\partial w_0''(y,y)}{\partial y} - \dot{y}^2 2\gamma w_1(y,y)\frac{\partial w_0'''(y,y)}{\partial y} + \dot{y}^2 2\gamma w_1'(y,y)\frac{\partial w_0'''(y,y)}{\partial y} \\
&\quad + \ddot{y}\int_0^1 w_1(x,y)\frac{\partial w_0(x,y)}{\partial y}dx + c_b\dot{y}\int_0^1 w_1(x,y)\frac{\partial w_0(x,y)}{\partial y}dx \\
&\quad + \dot{y}^2\Bigg(\alpha w_1(y,y)\frac{\partial^2 w_0(y,y)}{\partial y^2} - \gamma w_1(y,y)\frac{\partial^2 w_0''(y,y)}{\partial y^2} + \gamma w_1'(y,y)\frac{\partial^2 w_0''(y,y)}{\partial y^2} \\
&\quad + \int_0^1 w_1(x,y)\frac{\partial^2 w_0(x,y)}{\partial y^2}dx\Bigg) \\
&\quad + \dot{y}^2\Big(\alpha w_1(y,y)w_0''(y,y) - \gamma w_1(y,y)w_0''''(y,y) + \gamma w_1'(y,y)w_0''''(y,y)\Big) \\
&\quad + \ddot{y}\Big(\alpha w_1(y,y)w_0'(y,y) - \gamma w_1(y,y)w_0'''(y,y) + \gamma w_1'(y,y)w_0'''(y,y)\Big) \\
F_1 &= \nu\beta_1^4 + \ddot{y}\alpha w_1(y,y)\frac{\partial w_1(y,y)}{\partial y} + \dot{y}^2 2\alpha w_1(y,y)\frac{\partial w_1'(y,y)}{\partial y} - \ddot{y}\gamma w_1(y,y)\frac{\partial w_1''(y,y)}{\partial y} \\
&\quad + \ddot{y}\gamma w_1'(y,y)\frac{\partial w_1''(y,y)}{\partial y} - \dot{y}^2 2\gamma w_1(y,y)\frac{\partial w_1'''(y,y)}{\partial y} + \dot{y}^2 2\gamma w_1'(y,y)\frac{\partial w_1'''(y,y)}{\partial y} \\
&\quad + \ddot{y}\int_0^1 w_1(x,y)\frac{\partial w_1(x,y)}{\partial y}dx + c_b\dot{y}\int_0^1 w_1(x,y)\frac{\partial w_1(x,y)}{\partial y}dx \\
&\quad + \dot{y}^2\Bigg(\alpha w_1(y,y)\frac{\partial^2 w_1(y,y)}{\partial y^2} - \gamma w_1(y,y)\frac{\partial^2 w_1''(y,y)}{\partial y^2} + \gamma w_1'(y,y)\frac{\partial^2 w_1''(y,y)}{\partial y^2} \\
&\quad + \int_0^1 w_1(x,y)\frac{\partial^2 w_1(x,y)}{\partial y^2}dx\Bigg) \\
&\quad + \dot{y}^2\Big(\alpha w_1(y,y)w_1''(y,y) - \gamma w_1(y,y)w_1''''(y,y) + \gamma w_1'(y,y)w_1''''(y,y)\Big) \\
&\quad + \ddot{y}\Big(\alpha w_1(y,y)w_1'(y,y) - \gamma w_1(y,y)w_1'''(y,y) + \gamma w_1'(y,y)w_1'''(y,y)\Big)
\end{aligned}
$$

The mass equation expressed in matrix form after performing eigenmode expansion operations and expanding for $n = 0, 1$ (the mass equation is independent of m) is

$$G\ddot{y} + H\dot{y} + (HH)\dot{y}^2 = K - J, \tag{C.117}$$

where

$$
\begin{aligned}
G &= 1+\left[\eta_0\frac{\partial w_0(y,y)}{\partial y}+\eta_1\frac{\partial w_1(y,y)}{\partial y}\right]\left[\eta_0 w_0'(y,y)+\eta_1 w_1'(y,y)\right] \\
&\quad +\chi\left[\eta_0\frac{\partial w_0'(y,y)}{\partial y}+\eta_1\frac{\partial w_1'(y,y)}{\partial y}\right]\left[\eta_0 w_0''(y,y)+\eta_1 w_1''(y,y)\right] \\
&\quad +\mu\left[\eta_0\frac{\partial w_0(y,y)}{\partial y}+\eta_1\frac{\partial w_1(y,y)}{\partial y}\right]\mathrm{sgn}\big(\,*\,\big) \\
&\quad +\left[\eta_1 w_0'(y,y)+\eta_1 w_1'(y,y)\right]^2+\chi\left[\eta_0 w_0''(y,y)+\eta_1 w_1''(y,y)\right]^2 \\
&\quad +\mu\left[\eta_0 w_0'(y,y)+\eta_1 w_1'(y,y)\right]\mathrm{sgn}\big(\,*\,\big) \\
H &= c_m+2\left[\dot\eta_0\frac{\partial w_0(y,y)}{\partial y}+\dot\eta_1\frac{\partial w_1(y,y)}{\partial y}\right]\left[\eta_0 w_0'(y,y)+\eta_1 w_1'(y,y)\right] \\
&\quad +2\chi\left[\dot\eta_0\frac{\partial w_0'(y,y)}{\partial y}+\dot\eta_1\frac{\partial w_1'(y,y)}{\partial y}\right]\left[\eta_0 w_0''(y,y)+\eta_1 w_1''(y,y)\right] \\
&\quad +2\mu\left[\dot\eta_0\frac{\partial w_0(y,y)}{\partial y}+\dot\eta_1\frac{\partial w_1(y,y)}{\partial y}\right]\mathrm{sgn}\big(\,*\,\big) \\
&\quad +2\left[\dot\eta_0 w_0'(y,y)+\dot\eta_1 w_1'(y,y)\right]\left[\eta_0 w_0'(y,y)+\eta_1 w_1'(y,y)\right] \\
&\quad +2\chi\left[\dot\eta_0 w_0''(y,y)+\dot\eta_1 w_1''(y,y)\right]\left[\eta_0 w_0''(y,y)+\eta_1 w_1''(y,y)\right] \\
&\quad +2\mu\left[\dot\eta_0 w_0'(y,y)+\dot\eta_1 w_1'(y,y)\right]\mathrm{sgn}\big(\,*\,\big)
\end{aligned}
$$

$$
\begin{aligned}
HH &= \left[\eta_0\frac{\partial^2 w_0(y,y)}{\partial y^2}+\eta_1\frac{\partial^2 w_1(y,y)}{\partial y^2}\right]\left[\eta_0 w_0'(y,y)+\eta_1 w_1'(y,y)\right] \\
&\quad +\chi\left[\eta_0\frac{\partial^2 w_0'(y,y)}{\partial y^2}+\eta_1\frac{\partial^2 w_1'(y,y)}{\partial y^2}\right]\left[\eta_0 w_0''(y,y)+\eta_1 w_1''(y,y)\right] \\
&\quad +\mu\left[\eta_0\frac{\partial^2 w_0(y,y)}{\partial y^2}+\eta_1\frac{\partial^2 w_1(y,y)}{\partial y^2}\right]\mathrm{sgn}(*) \\
&\quad +2\left[\eta_0\frac{\partial w_0'(y,y)}{\partial y}+\eta_1\frac{\partial w_1'(y,y)}{\partial y}\right]\left[\eta_0 w_0'(y,y)+\eta_1 w_1'(y,y)\right] \\
&\quad +\left[\eta_0 w_0''(y,y)+\eta_1 w_1''(y,y)\right]\left[\eta_0 w_1'(y,y)+\eta_1 w_1'(y,y)\right] \\
&\quad +2\chi\left[\eta_0\frac{\partial w_0''(y,y)}{\partial y}+\eta_1\frac{\partial w_1''(y,y)}{\partial y}\right]\left[\eta_0 w_0''(y,y)+\eta_1 w_1''(y,y)\right] \\
&\quad +\chi\left[\eta_0 w_0'''(y,y)+\eta_1 w_1'''(y,y)\right]\left[\eta_0 w_0''(y,y)+\eta_1 w_1''(y,y)\right] \\
&\quad +2\mu\left[\eta_0\frac{\partial w_0'(y,y)}{\partial y}+\eta_1\frac{\partial w_1'(y,y)}{\partial y}\right]\mathrm{sgn}(*)+\mu\left[\eta_0 w_0''(y,y)+\eta_1 w_1''(y,y)\right]\mathrm{sgn}(*) \\
J &= \left[\ddot{\eta}_0 w_0(y,y)+\ddot{\eta}_1 w_1(y,y)\right]\left[\eta_0 w_0'(y,y)+\eta_1 w_1'(y,y)\right] \\
&\quad +\chi\left[\ddot{\eta}_0 w_0'(y,y)+\ddot{\eta}_1 w_1'(y,y)\right]\left[\eta_0 w_0''(y,y)+\eta_1 w_1''(y,y)\right] \\
&\quad +\mu\left[\ddot{\eta}_0 w_0(y,y)+\ddot{\eta}_1 w_1(y,y)\right]\mathrm{sgn}(*) \\
K &= \ddot{w}_o\left[\eta_0 w_0'(y,y)+\eta_1 w_1'(y,y)\right]+\mu(\ddot{w}_o+\bar{g})\mathrm{sgn}(*)
\end{aligned}
\tag{C.118}
$$

where

$$
\begin{aligned}
* &= \dot{y}+\left(\dot{w}_o+\left[\dot{\eta}_0 w_0(y,y)+\dot{\eta}_1 w_1(y,y)\right]+\dot{y}\left[\eta_0\frac{\partial w_0(y,y)}{\partial y}+\eta_1\frac{\partial w_1(y,y)}{\partial y}\right]\right. \\
&\quad \left.+\dot{y}\left[\eta_0 w_0'(y,y)+\eta_1 w_1'(y,y)\right]\right)\left[\eta_0 w_0'(y,y)+\eta_1 w_1'(y,y)\right]
\end{aligned}
\tag{C.119}
$$

These expressions can be solved numerically. Many of the terms used in the above equations depend on mass position, y, including $A_{L,n}$, $D_{L,n}$, $A_{R,n}$, $D_{R,n}$, β_n, ω_n, and the normalization coefficient. Using a computer program, the value of each of those terms for each discrete mass position along the length of the beam was calculated and a curve fit was done for each term's dependence on y. Then, partial derivatives of the beam deflection, w_n, with respect to y were computed using the curve fits before evaluating those partial derivatives at $x = y$ to get the value needed for the above equations. Similarly, integrals were evaluated numerically

only after the partial derivatives of beam deflection with respect to y were determined. Integration is along the full length of the beam, so the integrals were split into two terms for the left side (evaluated from 0 to y) and the right side (evaluated from y to 1) of the beam.

C.7 Programming equations in MATLAB

To enter this system into a computer code, start with the matrix form

$$\dot{X} = aX + b. \tag{C.120}$$

X is a vector containing the state variables, which for us is

$$X = \begin{bmatrix} \eta_1 \\ \eta_2 \\ y \\ \dot{\eta}_1 \\ \dot{\eta}_2 \\ \dot{y} \end{bmatrix}, \quad \dot{X} = \begin{bmatrix} \dot{\eta}_1 \\ \dot{\eta}_2 \\ \dot{y} \\ \ddot{\eta}_1 \\ \ddot{\eta}_2 \\ \ddot{y} \end{bmatrix} \tag{C.121}$$

The matrix a is composed of the terms A, B, C, D, E, F, G, H, HH, and J, which are given above. The matrix b is composed of terms K and Q given above. The equations from the previous section are rearranged to give

$$\begin{bmatrix} A_0 & B_0 \\ A_1 & B_1 \end{bmatrix} \begin{bmatrix} \ddot{\eta}_0 \\ \ddot{\eta}_1 \end{bmatrix} = - \begin{bmatrix} C_0 & D_0 \\ C_1 & D_1 \end{bmatrix} \begin{bmatrix} \dot{\eta}_0 \\ \dot{\eta}_1 \end{bmatrix} - \begin{bmatrix} E_0 & F_0 \\ E_1 & F_1 \end{bmatrix} \begin{bmatrix} \eta_0 \\ \eta_1 \end{bmatrix} + \begin{bmatrix} Q_0 \\ Q_1 \end{bmatrix} \tag{C.122}$$

$$G\ddot{y} = -H\dot{y} - (HH)\dot{y}^2 + K - J. \tag{C.123}$$

Further rearranging is necessary because terms E and F contain not only η, y, and $\dot{y}$ terms, but also $\ddot{y}$ terms. Similarly, J contains $\ddot{\eta}$ terms. Breaking up E, F, and J into two parts - one that is a function of only state variables on the right hand side of equation (C.120) and another that is a function of variables on the left hand side of (C.120). To reconcile this issue, equation (C.120) can be expressed as

$$\begin{bmatrix} 1 & 0 & 0 & 0 & 0 & 0 \\ 0 & 1 & 0 & 0 & 0 & 0 \\ 0 & 0 & 1 & 0 & 0 & 0 \\ 0 & 0 & 0 & A_1 & B_1 & (E_{1b}\eta_1 + F_{1b}\eta_2) \\ 0 & 0 & 0 & A_2 & B_2 & (E_{2b}\eta_1 + F_{2b}\eta_2) \\ 0 & 0 & 0 & J_a & J_b & G \end{bmatrix} \begin{bmatrix} \dot{\eta}_1 \\ \dot{\eta}_2 \\ \dot{y} \\ \ddot{\eta}_1 \\ \ddot{\eta}_2 \\ \ddot{y} \end{bmatrix} = \begin{bmatrix} \dot{\eta}_1 \\ \dot{\eta}_2 \\ \dot{y} \\ -E_{1a}\eta_1 - F_{1a}\eta_2 - C_1\dot{\eta}_1 - D_1\dot{\eta}_2 + Q_1 \\ -E_{2a}\eta_1 - F_{2a}\eta_2 - C_2\dot{\eta}_1 - D_2\dot{\eta}_2 + Q_2 \\ -H\dot{y} - HH\dot{y}^2 + K \end{bmatrix} \tag{C.124}$$

Because of the nonlinearity of the equations we are working with, it is not possible to represent the right hand side of the equation strictly in matrix form.

Appendix D

Microfabrication Processing Details

D.1 PZT film deposition

The steps for deposition of the lead zirconate titanate (PZT) sol-gel film are shown in figure D.1. First, a single layer of lead titanate (PT) is spin coated onto the wafer at 500 rotations per minute (RPM) for 10 seconds, then 3000 RPM for 15 seconds. The wafer is then baked at 400° C for 1 minute and annealed at 600° C for 1 minute in an oxygen environment.

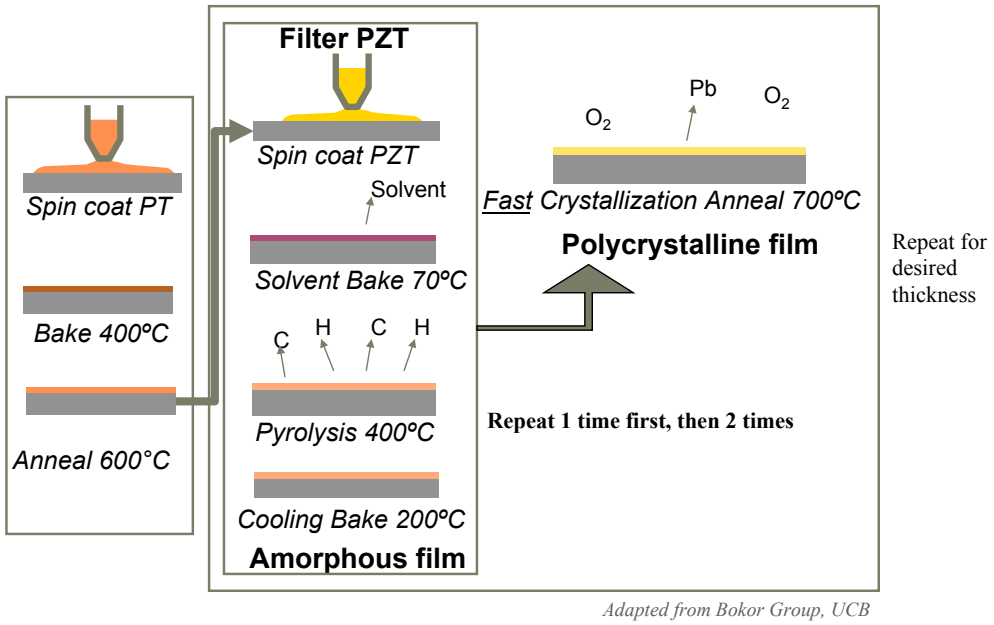

Figure D.1: Diagram of processing steps required to deposit a sol-gel PZT film.

Next, the first layer of PZT is filtered to remove any particles and deposited using a pipet onto the spinning wafer at 500 RPM for 10 seconds and then 3000 RPM for 30 seconds. The

wafer is then baked at 70° C for 1 minute to drive off the solvent and pyrolyzed at 400° C for 5 minutes to drive off organics. To ensure slow cooling, the wafer is moved to a hotplate at 200° C for approximately 30 seconds. At this point the PZT film is amorphous. A 700° C rapid annealing step is then performed in an oxygen environment. These steps are repeated as many times as necessary to achieve the desired film thickness. Each spin-bake-anneal step results in a PZT thickness of about 100 nm. Figure D.2 presents a scanning electron micrograph showing the PZT film obtained in this research.

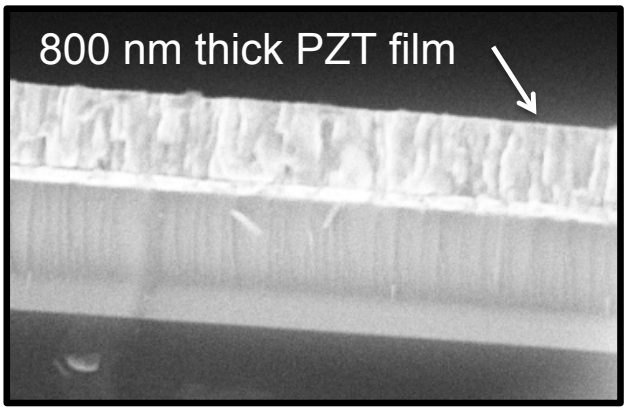

Figure D.2: Scanning electron micrograph of a sol-gel deposited PZT film.

It is important to ramp up to 700° C very quickly (essentially as quickly as the rapid thermal annealing tool can manage). The temperature is held for 1 minute before cooling as quickly as possible. One reason that the rapid heating and cooling are necessary is to avoid formation of the pyrochlore phase of PZT, which is not piezoelectric, as the film heats to 700° C. Its presence in a PZT film will degrade the piezoelectric coefficient significantly.

In the course of depositing these sol-gel films, it was found that catastrophic piezoelectric film delamination is a serious problem unless very specific film layers are used beneath the PZT. The dielectric layer that is deposited on top of the silicon wafer must be thermally grown oxide and the electrode beneath the PT/PZT layer must be a sputtered platinum film. The use of low temperature oxide, low stress nitride, or stoichiometric nitride resulted in complete piezoelectric film delamination, as did evaporated platinum bottom electrodes or bottom electrodes of a different metal. The information reported here corresponds with the Mitsubishi 1% PT (125/100) F2 and Mitsubishi PZT 15% [Pb125(Zr52Ti48)O3] E1 solutions, and it is possible that different sol-gel solutions have different processing requirements. Because of the challenges involved in obtaining a high quality sol-gel PZT film, aluminum nitride is recommended as a MEMS piezoelectric material instead.

D.2 Residual stress causing curling of cantilevers

Residual stress is often a problem in free-standing MEMS fabricated devices. Common sources of this residual stress are lattice mismatch of the thin films and thermally induced stress. For example, the thermal oxide used in the cantilevers presented in this work is grown at temperatures near 1000° C, so it experiences thermal contraction as it cools down. Evaporated and sputtered films also commonly contain residual stress.

Sometimes it is possible to make changes to the fabrication process in order to eliminate the residual stress, but other times this is not an option. One option in the latter case is to use argon ion bombardment [3], which works both by generating a thin layer of compressively stressed material on the outer surface and etching away layers of strained material. If the cause of the residual stress lies in the lower, covered layers rather than the top exposed layer, however, argon ion bombardment will not work.

In this research, the residual stress problem was solved by balancing rather than eliminating the highly stressed layer. To achieve this, the location of the neutral axis of the cantilever was calculated and the stress levels of each film layer were measured or estimated. It was determined that the thermal oxide layer had a residual stress about an order of magnitude higher than the other layers, and the location of the neutral axis was such that the entire oxide film was below the neutral axis, causing the cantilevers to curl up upon release. To eliminate the curling problem, a layer of silicon was left on the underside of the cantilever (rather than etching away all of the silicon). This moved the neutral axis location to be within the thickness of the oxide layer so that the bending moment due to residual stress cancelled out. The success of this method can be seen in the three righthand photographs of figure D.3. The top photograph had no compensating silicon layer, the middle photograph had a very thin layer, and the bottom photograph had several microns of silicon layer.

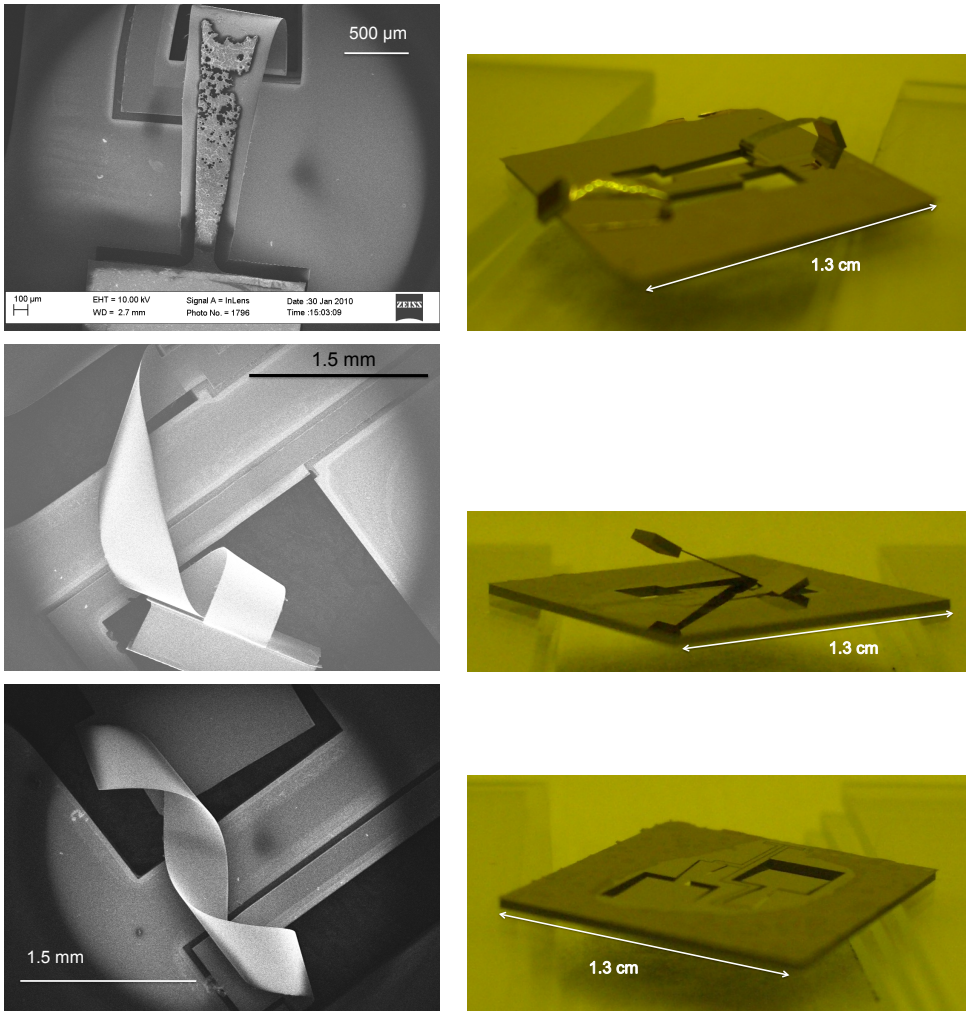

Figure D.3: On the left: three scanning electron micrographs showing the results of high levels of residual stress in a cantilever. On the right: three photographs showing how the effects residual stress can be successfully eliminated by incorporating stress-balancing layers. The top left and right images are of the same device.